A breathing anthropomorphic liver phantom for interventional radiology

Design and evaluation

D.R. Adrichem

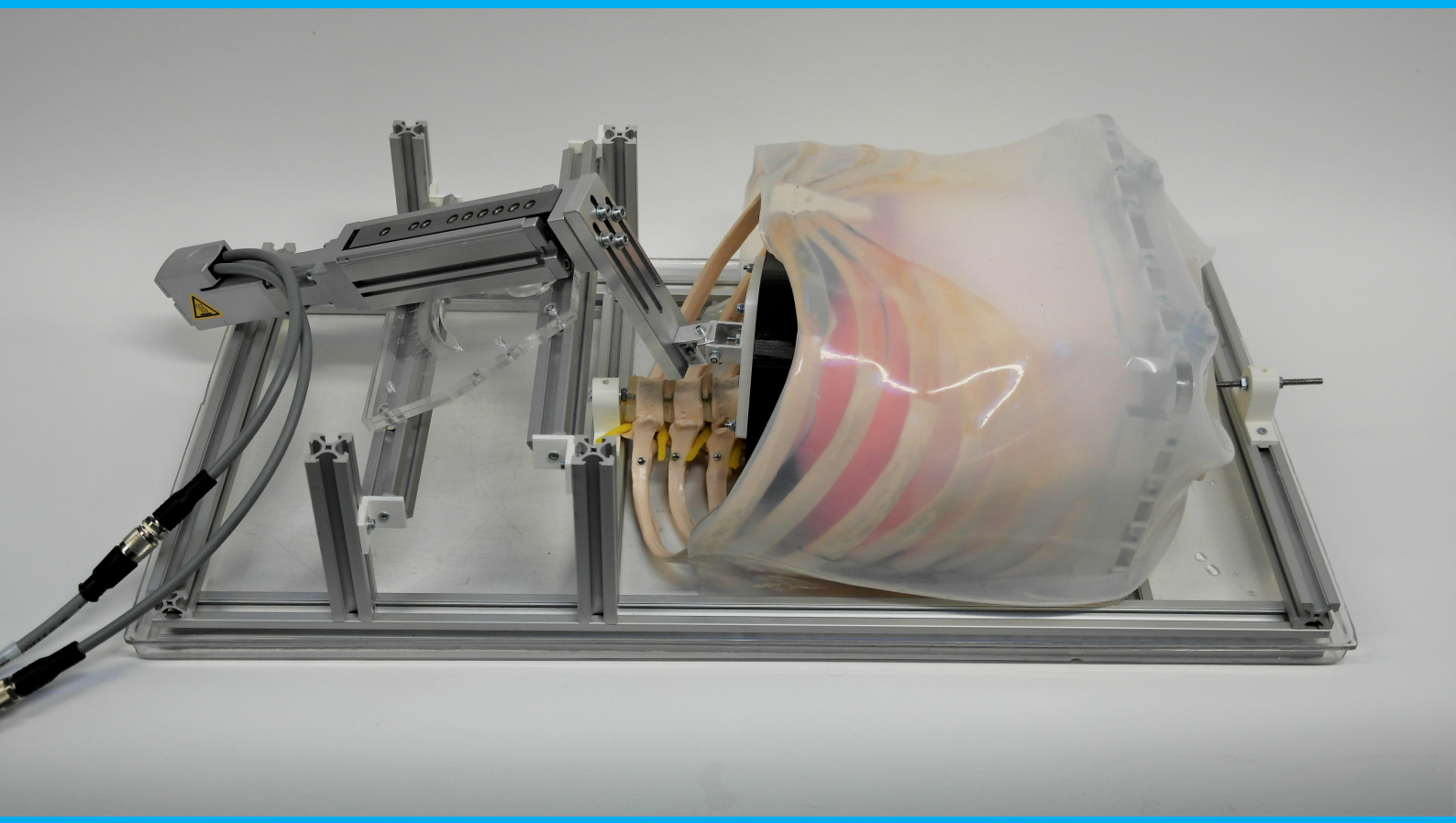

TU Delft

A breathing anthropomorphic liver phantom for interventional radiology

Design and evaluation

by

D.R. Adrichem

to obtain the degree of Master of Science
at the Delft University of Technology,
to be defended publicly on Tuesday Februari 7, 2018 at 13:00.

Student number:	4081439	
Project duration:	March, 2017 – Februari, 2018	
Thesis committee:	Dr. J. J. van den Dobbelsteen,	TU Delft, chairman
	Ir. T. L. de Jong,	TU Delft, supervisor
	Dr. Y. Song,	TU Delft, external member

An electronic version of this thesis is available at `http://repository.tudelft.nl/`.

TU Delft

Preface

Ever since I was young, I have been intrigued by how things work. Nowadays, the combination of a technical perspective and biological systems have been the drive to combine different fields and discover the overlap between them. This resulted in a master thesis project which takes technical understanding and applies it on biological systems to improve where possible. In the future, I would like to continue my work in creating contributing solutions. I have been given the tools and opportunity, so I will use them.

During my time as a student, I have made a ton of new, smart, funny and good friends, had my share of experience abroad and got to function in multidisciplinary teams. For this great time, I want to thank a lot of people. Those who I met on the way and those whom I have always known. First of all, an indescribable thanks to the never-ending support from my parents, the ones who made it possible for me to be where I am today. Further, I would like to thank my supervisors Tonke de Jong and John van den Dobbelsteen for the loads of questions during my project meetings, which provoked me to be critical about every decision. Another thanks to Arjan van Dijke, which helped me a lot during the physical construction of my final design and the overall support. A big thanks to the physicians dr. W. Polak and dr. A. Moelker from the Erasmus MC whom provided essential feedback for further development. Furthermore, I thank my girlfriend and close friends who gave me mental strength to continue whenever I was hesitant. Thank you all so very much.

'*Unless you expect the unexpected you will never find the truth, for it is hard to discover and hard to attain.*'
Heraclitus

D.R. Adrichem
Delft, Februari 2018

Abstract

Liver cancer causes 700.000 deaths annually. To assess new devices and pre-clinical procedures for treatment, a safe test environment can be provided by a phantom. Phantoms act as a surrogate for certain physical properties of tissue. The purpose of this study is to design, construct and evaluate an anthropomorphic liver phantom, which simulates respiratory motion and inhibits similar needle-tissue interaction for ultrasound-guided needle interventions. The liver model and surroundings are made from water-based solution with polyvinylalcohol (PVA). The liver model and surroundings are made of 6%m, 4%m PVA with 2 and 3 freeze thaw cycles, respectively. The rigid structures, i.e. vertebrae and ribs, are made of a flexible polymer. Three-dimensional printing technique is employed to create molds for the anthropomorphic structures in terms of organ shape. Detailed steps for phantom construction and choice of phantom ingredients and construction recipe are reported. The actuation is provided by a linear actuator, which is adjustable in stroke length, frequency and direction. Preliminary results of the reproduced motion in the liver model are 20.7, 10.8 and 6.7 mm in CC, AP and LR direction, respectively. Further, the phantom allows both subcostal and intercostal ultrasound needle guidance. The liver model is designed to simulate diseased tissue. From Fibroscan measurements, the liver model is characterized with an elastic modulus of 24.0($\pm$8.0) kPa. Further, the liver model shows median higher axial needle friction forces (0.0374 N mm^{-1}) compared to healthy liver tissue (0.01108 N mm^{-1}). Furthermore, tactile feedback on the liver model is obtained from a liver surgeon, dr. W. Polak, whom graded the liver model with fibrosis scale 2. Based on the Fibroscan results, increased needle friction forces and tactile feedback, the liver model can be classified as cirrhotic. Additionally, the prototype is assessed by head of the section interventional radiology at the Erasmus MC, dr. A. Moelker. The doctor was able to perform ultrasound-guided needle insertion. Concluding, that a working prototype, which simulates respiratory motion and inhibits similar tissue-needle interaction as human tissue for ultrasound-guided needle interventions, is created.

List of Figures

List of Tables

Contents

Abbreviations

In this report several abbreviations are frequently used. The abbreviations are presented and summurized as follows:

- US = Ultrasound
- IQR = Interquartile range
- CT = Computed Tomography
- FT = Freeze-thaw
- CC = Crano-caudal
- AP = Anteroposterior
- LR = Left-Right
- PVA = Poly-vinyl Alcohol
- rpm = Repetitions per minute
- IC MC = Intercostal midclavicular
- IC MA = Intercostal midaxillary
- SC MP = Subcostal midplane

1 Introduction

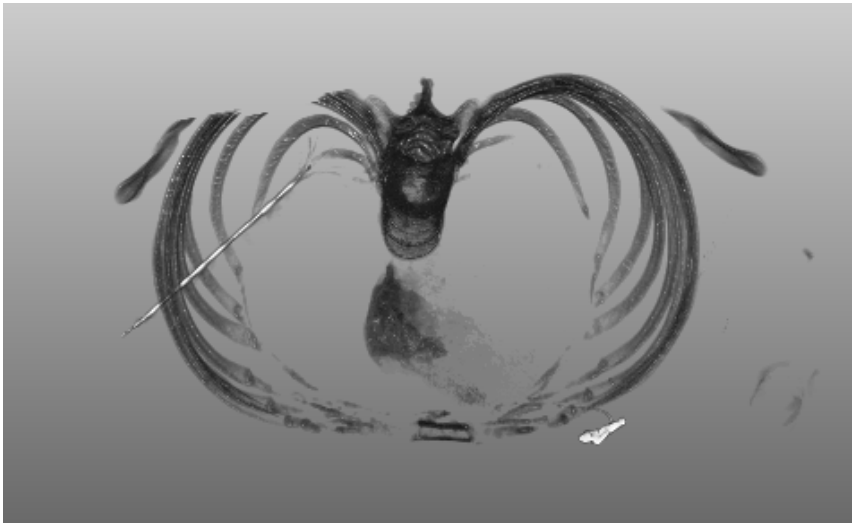

Figure 1.1: Example of needle insertion for a radio frequency ablation procedure captured in computed tomography imaging.

The second leading cause of cancer mortality in the world is due to liver cancer, which annually leads to more than 700,000 deaths [1]. The arrival of new devices and procedures can help to reduce morbidity due to liver diseases. In order to assess treatment devices and methods, a phantom can be used. An example of a treatment, is a radiofrequency ablation treatment as shown in figure 1.1. Phantoms provide a safe environment to test pre-clinical and novel devices and procedures. Phantom models are used as substitution for real tissue in studies where *in-vivo* and *ex-vivo* models are inappropriate or hard to obtain.

In this chapter a short background is given. Further, the problem statement is presented. Furthermore the research goal and project approach are described.

1.1. Background

In this part, a short background is given. In chapter 2 a more elaborate theoretical background is provided.

The liver is a dynamic organ in the human body. The liver is red-brown and situated in the upper-right part of the abdomen. It consumes 25% of the total cadiac output and due to its position directly underneath the diaphragm, it is subjected to respiratory motion. Due to the fact that the liver is an active organ and has the largest cardiac output passing through, many problems can occur which might tip the functionality off balance. For example, after chronic scarring due to fibrosis, the liver undergoes a physical change. The tissue characteristics of the liver change in different states of fibrosis [2]. The tissue charateristics is one of the parameters that influences needle-tissue interaction. Needle-tissue interaction is the way a needle interacts with the tissue in which it is inserted. This interaction can be described in reaction forces, needle trajectory and tissue deformation [3] and is influenced by tissue characteristics, needle properties and insertion parameters.

Liver phantoms are currently used for several clinical applications, such as tumor motion replication [4], needle-tissue interaction simulation [5] and perfusion reproduction [6]. A phantom can be modeled on anatomical structures, like vessels and vascular branches, or on mechanical structures that behave appropriately. A benefit of using a phantom model over an anatomical specimen is the ability to precisely model a selected structure or function, which is known and can be reproduced. Additionally, a phantom has benefits in long-term structural stability. Measurements over a prolonged period of time can be obtained without concern for loss in performance or subject discomfort and/or motion [7]. Sequentially, a phantom allows for easy registration of multiple phantom images and comparison between subsequent studies.

Tissue-mimicking materials (TMMs) have been reported to be an important tool for research facilitation in performance testing and procedure development and optimization of needle-tissue interaction simulation. Commonly used TMMs are agar, polyvinylalcohol (PVA), polyvinylchloride (PVC), gelatine, polyacrylamide (PAA) and silicone [8]. From recent studies, PVA has shown to be interesting for phantom design [5, 9]. The properties of the hydrogel is attractive for biomedical application due to the fact that they are hydrophilic cross-linked polymers. In fact, due to the crosslinks, the hydrogels can be made heterogeneous in a conditioned matter. For needle-tissue interaction, the friction slope, amount of peak forces and height of peak forces can be modulated and can closely represent human tissue by altering concentration and freeze-thaw cycles [5]. Additionally, the gels can be shaped in solid structures, the acoustic impedance and speed of sound [10] can be tuned to be closely to biological tissue.

1.2. Problem statement

In general, patients greatly benefit from improved technology in the health care. The more is known about a disease, the better it can be treated. Clearly, to treat difficult diseases, constant innovation is needed to find the most suitable treatment for each patient. New treatment methods and equipment need to be tested prior to being used in the field. A phantom allows testing in a safe and harmless environment and is therefore desirable. Another aspect is education. A starting health practitioner needs profound training to acquire the expertise for conducting a treatment. Both educating the desired skills as well as testing, are preferably not done on real patients, but on cadavers or phantoms. A phantom recreates a safe environment where mistakes are still acceptable and safe.

Literature shows that a simple phantom already has the potential to accelerate interventional training by providing a platform where core skills can be acquired [11]. Further, commercial phantoms tend to be prohibitively costly, do not have an infinite shelf life and often do not fulfill the desired specifications. Thereby, giving rise to the creation of in-house models using every day materials, as described in the work of Nicholson and Crofton [12]. Many studies have already been conducted using a phantom model, for example to verify the design and evaluation of an MRI-compatible linear motion stage to recreate respiratory motion [13], simulate perfusion for the evaluation of ultrasound contrast agents [6] or to test a new training device [14].

However, the following problem statement is presented:

"No model has been found that contains complex geometries and structures which enables the phantom to have respiratory motion and still have similar physical properties as human tissue."

In current literature, no liver-shaped phantoms are found. Further, respiratory phantoms are often limited to translation in 1 degree of freedom and little knowledge is available on needle-tissue interaction of TMMs simulating diseased tissue. The absence of an advanced liver phantom creates a limitation for researchers and clinicians to test and assess novel devices or pre-clinical procedures.

1.3. Translation of problem into technical principle

First of all, the liver moves as a consequence of the contraction of the diaphragm and intercostal muscles, which in turn allows respiration to happen. Therefore, a dynamic system is considered. The motion is dominant in cranio-caudal (CC) direction, given as the solid black arrow in figure 1.2. Secondly, organs in the abdomen translate as consequence of the respiratory motion. Organs in the abdominal cavity are compressed against the pelvic bone and ribs. Lower organs, i.e. intestines, move dorsoventral to make space. The first technical principle is the simulation of liver motion, which is caused by respiratory motion.

Additionally, a needle is inserted into tissue. Therefore, the second technical principle is needle-tissue interaction. Needle-tissue interaction describes how a needle responds in the inserted tissue. The interaction can be quantified in needle forces, needle deflection and/or tissue deformation.

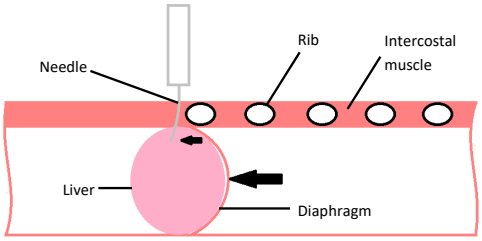

Figure 1.2: Saggital perspective on the technical principle of needle deflection as effect of respiratory motion. Pink simulating the liver, black circles the ribs and the black arrows relative motion directions.

1.4. Research goal

The research goal is formulated as follows:

"Develop a phantom which is able to replicate liver movement due to respiratory motion and shows similar needle-tissue interaction as human tissue in image-guided needle interventions."

In this work, an anthropomorphic breathing liver phantom is presented. Due to limited knowledge of the motion of the liver and relative motion of the ribs in the human body during respiration, a separate investigation is presented in chapter 2 to serve as design criteria in the design phase. Further, the needle-tissue interaction is determined through needle forces and needle deflection.

The final goal of this project is the achievement of a fully functional experimental model for simulation of respiratory motion and characterized needle-tissue interaction during ultrasound-guided needle interventions.

1.5. Project approach

This work involves several phases which contribute to the final result. In this section, relevant preliminary work is mentioned as basis of the presented work and the lay-out of the thesis is discussed.

1.5.1. Previous work

This study continues on the findings in previous work of Pluymen [9] whom investigated the material characteristics for TMMs in needle-tissue interaction for the human liver. Further, anthropomorphic liver design in a scaled model has previously been performed by Tom Paardenkoper. This work aims to combine the previous conducted works and add functionality by introducing respiratory motion of the liver during ultrasound-guided needle interventions.

1.5.2. Thesis structure

The thesis is structured as visualized in figure 1.3 and is described as follows:

In chapter 2, a theoretical background is presented to provide information about the anatomy, mechanical and imaging properties of the liver. Further, needle-tissue interaction is described and a review on current respiratory phantom designs is presented. An investigation into liver and rib motion is reported as basis for the design criteria in chapter 3.

In chapter 4, the design process is described. Phases in the design process are conceptual design, embodiment design, detailed design and design for manufacturability. The prototype is presented in chapter 5. In chapter 6, the evaluation methods and evaluation results are reported. The interpretation of results and the limitations of the study are described as discussion in chapter 7. Additionally, recommendations for future work are discussed. The work is concluded with a conclusion in chapter 8.

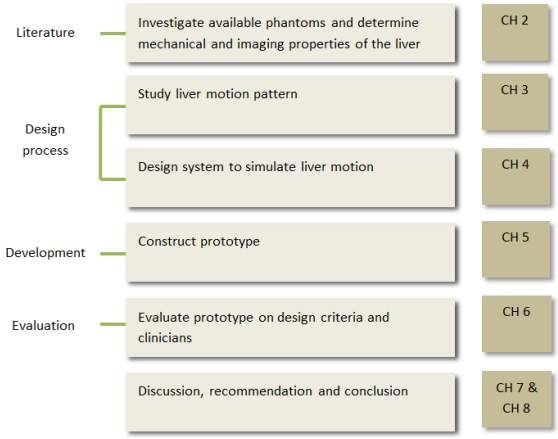

Figure 1.3: Structural overview of the thesis structure.

2
Theoretical background

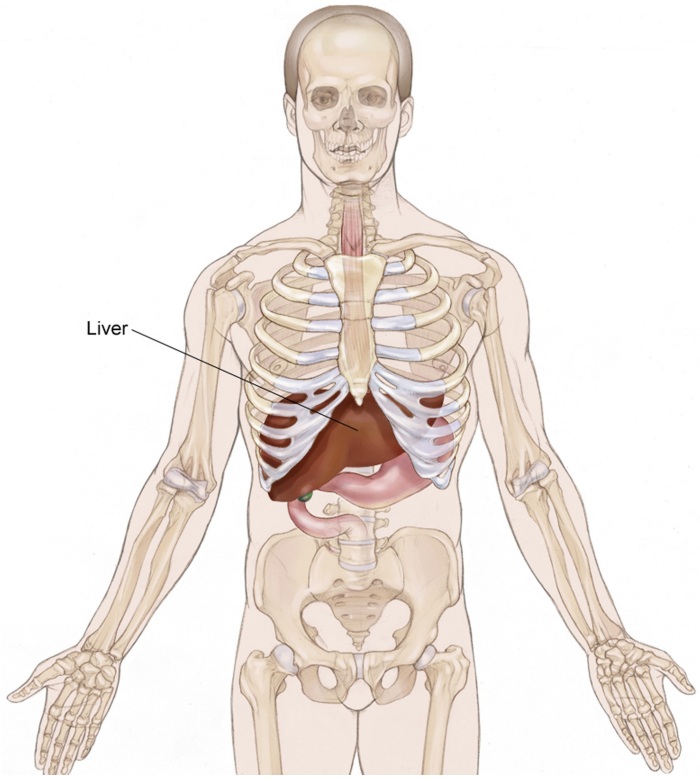

Figure 2.1: Position of the liver inside the human body. Adopted *from* Morreale, 2004. Accessed on: 12-01-2018

In this chapter, the theoretical background is presented. The three main topics that are enlightened, are as follows: first, the liver, where the anatomy and common pathologies are described. Second, interventional radiology, where common interventions are presented and third, available respiratory phantoms and the design of those phantoms are described.

2.1. Liver

This study is concentrated around the simulation of the liver. To gain insight in the working principles, the environment in which the liver is situated and the used procedures, are reviewed. In this section, elaboration on the general anatomy, hepatic vasculature, pathology and physical properties of the liver is done.

2.1.1. General anatomy

The liver is a vital organ and acts as a filter of the blood. As it is the largest organ, it accounts for 2% to 3% of the average body weight, ranging from 1200-1500 grams. The liver contains two lobes and is described by its functional anatomy in figure 2.2 [15]. Situated right beneath the hemidiaphragm in the right upper quadrant of the abdominal cavity, as shown in figure 2.1 [16]. It remains in position through ligamentous attachment and finds protection behind the ribcage. The attachments are not true ligaments, but are avascular and line up with the Glisson capsule, which is the visceral peritoneum of the liver [15].

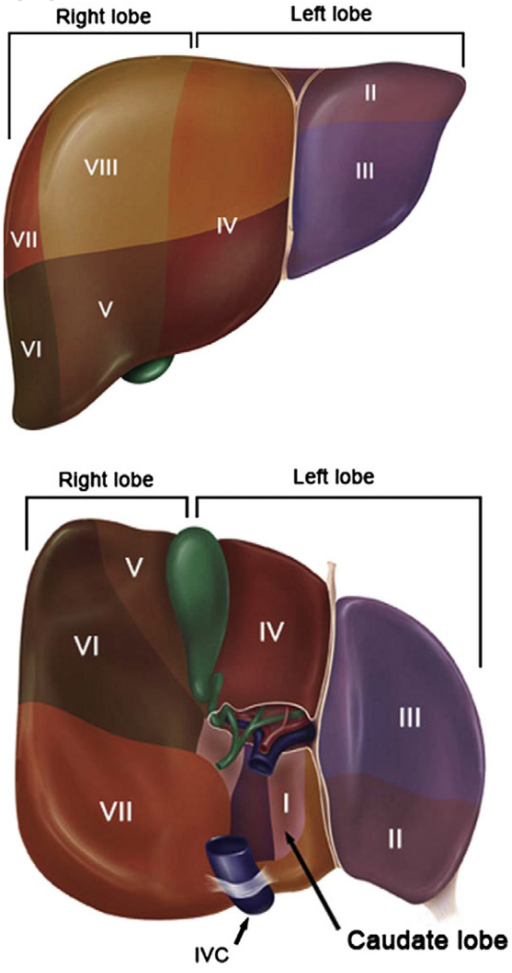

Figure 2.2: Anterior and posterior surfaces of liver where also the left and right hepatic lobes with Couinaud's segmental classification are illustrated. Figure as *from* Brunicardi et al. adopted *from* Abdel-Mish and Bloomston, 2010.

In this work, the anatomical planes are often used as reference for direction and position. As assitance, the anatomical planes are visualized in figure 2.3 [17].

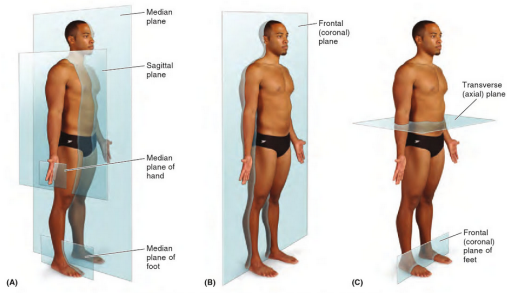

Figure 2.3: Anatomical planes. A) sagittal plane and mid/median plane. B) Frontal or Coronal plane. C) Transverse plane. Adopted *from* Moore et al., 2013.

2.1.2. Hepatic vasculature

The liver consumes at rest up to 25% of the total cardiac output, which is more than any other organ. The blood enters the organ via a dual supply, which consists of the hepatic artery, contributing 25% to 30% of the total supply and the portal vein, covering the other 70% to 75%. The supply from both entries finally mixes within the hepatic sinusoids, whereafter the mix is drained into the hepatic venous system [15]. In figure 2.4 the shape of the main hepatic vasculature and biliary anatomy are shown. The liver serves as a buffer for blood which can rapidly can be mobilized during a hemorrhage, yet hepatic blood flow tends to be maintained constant [18].

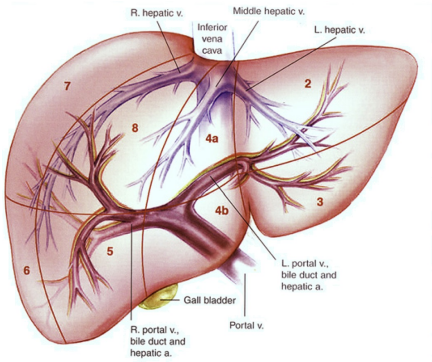

Figure 2.4: Anterior view of the hepatic vasclature and biliary anatomy. Figure as *from* Cameron and Sandone retrieved *from* Abdel-Mish and Bloomston, 2010.

2.1.3. Pathology

Due to the fact that the liver is an active organ and has the largest cardiac output passing through, many problems can occur which might tip the functionality off balance. In this section commonly observed diseases are discussed.

NAFLD and NASH Nonalcoholic fatty liver disease (NAFLD) and nonalcoholic steatohepatitis (NASH) are the first stages of a faulty liver function. Due to the emerging obesity epidemic in North America and other parts of the world these disorders gain more recognition as essential components of abnormal liver function. The hepatic manifestations of the insulin resistance syndrome can be subscribed to NAFLD and NASH and cover the associated spectra of fatty liver disease. NAFLD and NASH can progress to liver cirrhosis and might eventually be the cause of hepatocellular carcinoma (HCC) [19]. NAFLD and NASH are characterized by fatty deposition on the liver surface and increased liver size. In figure 2.5, this is seen as the first step after the healthy liver [20]).

Alcoholic fatty liver disease and alcoholic hepatitis Like NAFLD and NASH, alcoholic fatty liver disease and alcoholic hepatitis is characterized by the deposition of fat in the liver cells. The cause is due to high alcohol intake over a prolonged period of time and results in fat depostion on the liver. First symptoms that might occur are fatigue and discomfort in the upper right abdomen, followed by nausea and vomiting. Damage in this phase is still reversible with abstinence of alcohol. Severe hepatitis might lead to liver failure or death [21]. Study shows that even if a nutritious diet is followed, it will not prevent the development of this disease if excessive intake of alcohol is chronically consumed [22].

Cirrhosis Liver cirrhosis occurs in response to chronic liver disease and is defined as the histological development of regenerative nodules surrounded by fibrosis bands. Alcoholic cirrhosis occurs in response to heavy alcohol abuse and is marked by severe scarring on the liver [21]. Cirrhosis might eventually lead to portal hypertension and end-stage liver disease. The disease is an advanced stage of fibrosis, which is the result of abnormal wound-healing. Fibrosis is described by the process of encapsulating or replacement of injured tissue. The disorder is accompanied by a distortion in the hepatic vasculature [23]. In figure 2.5, the last phase is noted as a cirrhotic liver, where the surface is observed as nodular.

Hepatocellular carcinoma Hepatocellular carcinoma (HCC) is a collective term for liver cancer and comes in a large variety. The occurrence of HCC is closely associated with liver cirrhosis and the development varies in different parts of the world. For example, in Japan most males are affected in the sixth and seventh decade of life compared to Mozambique, where the males are more susceptible in their third and fourth decades [24].

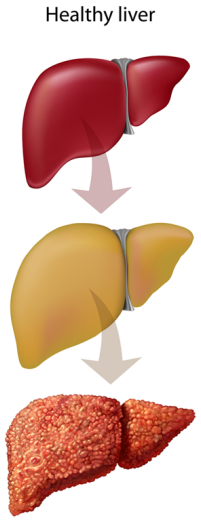

Figure 2.5: Transition of a healthy liver to a fatty liver, to a cirrhotic liver. Adopted *from* Eubanks, 2013 (adjusted).

2.1.4. Needle-tissue interaction

The interaction between tissue and needles has been of interest in many studies. The relevance can find its origin in the improvement of minimal invasive procedures [25]. Needle-tissue interaction is determined by needle properties, tissue properties and insertion parameters and influences on needle forces, needle deflection and tissue deformation. The interaction is shown in figure 2.6.

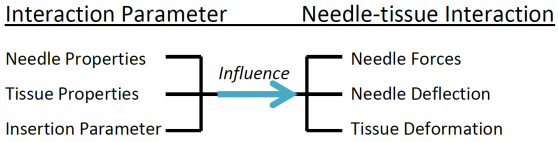

Figure 2.6: Overview of influencing interaction parameters on the needle and tissue response. Adopted *from* de Jong et al., 2017 (adjusted)

Interaction parameters

In this part, three aspects that influence the response of both needle and tissue are described. The aspects are: needle properties, tissue properties and insertion parameters.

Needle properties A needle can be of all sizes and shapes. The shape of the tip and diameter of the needle significantly determine the interaction between tissue and needle. The tip of the needle can be symmetrical or asymmetrical. Some common needle tip shapes are shown in figure 2.7. Each shape has its own characteristics in terms of needle reaction forces and needle deflection. A sharper needle will result in lower axial force, since resulting cutting force will be lower upon insertion [26]. Needle deflection is affected by the symmetry of the tip. An asymmetrical

bevel tip has more deflection than a symmetrical diamond shaped tip. Yet, all needles show deflection due to in-homogeneous material properties of the interacting tissue [27].

Figure 2.7: Common needle tip shapes, left to right: blunt, beveled, conical, sprotte, diamond, Tuohy. Adopted *from* van Gerwen et al., 2012.

As for the needle diameter: a bigger needle diameter will result in more tissue displacement and compression, thus in turn more normal forces act on the shaft. The increased normal forces result in higher friction along the shaft [27]. Furthermore, needle deflection is influenced by needle diameter. A thicker needle will show less deflection due to an increased rotational inertia. Additionally, stiffer needles will also show less deflection [28].

Tissue properties - mechanical properties The mechanical properties of tissue depict the way the material deforms and how the tissue will react to needle interaction. The liver itself possesses non-linear elastic behavior. The liver is classified as a visco-elastic tissue. Furthermore, the liver is both temporal as spacial dependent, meaning that the tissue will react differently under altering test configurations. More features of visco-elastic material are material relaxation (decrease of stress during constant strain), creep (increase of strain under constant stress) and hysteresis (loss of energy during loading and unloading). Further, the liver is an-isotropic (directional dependent characteristics) and non-homogeneous (location dependent characteristics) [29]. All these variables make it hard to quantify the elastic modulus of the liver. Besides the visco-elastic behaviour, as aforementioned, the pathology influences the stiffness of liver tissue. Researchers observed significantly increased stiffness in case of fibrosis [2].

Tissue properties - motion The needle-tissue interaction of the liver is not only difficult to determine due to its visco-elastic behavior, but the organ residences under constant motion. As mentioned before, the liver is situated underneath the diaphragm. The postition of the liver makes that it moves with respiratory motion, which is between 12-18 pulses per minute for quiet breathing. The influence of the respiratory motion on needle-tissue interaction is investigated in this research. In the next chapter, a separate study is presented to elaborate more respiratory motion.

Insertion parameters Besides the needle properties and tissue properties, also the way a needle is inserted affects needle-tissue interaction. In literature, the needle insertion force and velocity are often kept constant to allow comparison of the effects [30]. An increased velocity shows an increase of interacting needle forces [31], whereas the needle deflection tends to decrease with higher insertion velocities [28].

Interaction response
In this part, the response that is influenced by the interaction parameters is described. The needle-tissue interaction can be quantified by needle force, needle deflection and tissue deformation. Only needle force is described below, since this parameter will be used for prototype characterisation.

Needle force During needle insertion and retraction, three phases can be distinguished, being a deformation, insertion and retraction phase [27]. The phases occur chronologically. In the deformation phase, tissue deformation occurs due to contact of the needle with the tissue surface. Forces continues to increase while the surface starts to deform. Once, the surface is punctured, the second phase starts. The second phase is referred as the insertion phase. During the insertion phase, forces act on both the tip and shaft, cutting and friction forces, respectively. Once the desired depth is reached, the third phase starts. In the third phase is called the retraction phase. The needle is retracted from the tissue. The only forces in play during the retraction phase, are friction forces on the shaft. An example of axial needle forces in a needle run is shown in figure 2.8 as a force-position diagram [27].

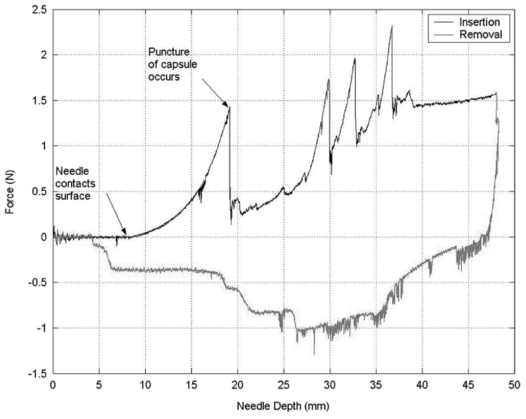

Figure 2.8: Axial needle force measured during needle insertion and retraction. Adopted *from* Okamura et al., 2004.

In equation 2.1, the axial reaction force of the needle can be described as a combination of force resulting from initial tissue stiffness at contact ($F_{\text{stiffness}}$), needle friction along the shaft (F_{friction}), and needle cutting force at the tip (F_{cutting}). In the equation, x depicts the location of the needle in a certain point in time. The stiffness forces are a result of tissue deformation at insertion and act only up to tissue puncturing. Cutting forces only act during insertion. Friction forces act both during insertion as retraction. The friction forces and cutting forces are determined by the internal tissue stiffness [27].

$$F_{\text{needle}}(x) = F_{\text{stiffness}}(x) + F_{\text{friction}}(x) + F_{\text{cutting}}(x) \quad (2.1)$$

2.1.5. Ultrasound imaging properties

Ultrasound imaging is presented because it is a fast and easy manner of image generation. It can be used to recreate an image constructed from the reflection of high frequency sound waves. The variables which affect the image reconstruction are firstly, the material acoustic impedance, which is the resistance of the material for ultrasound wave propagation and secondly, the acoustic attenuation [dB cm^{-1} MHz^{-1}], which is the loss of wave amplitude due to absorption, reflection and scattering. Boundaries of tissue layers can be noted by the amount of reflection. Difference in acoustic impedance of the touching tissue layer determines the amount of reflection [32]. Strong reflection can be seen from tissue like bone (high impedance) or air (low impedance), because the impedance differs strongly from surrounding tissues. An-echogenic structures are reconstructed as a black object, since no ultrasound waves are reflected. The acoustic attenuation is dependent on the frequency of the ultrasound waves. A higher frequency leads to a higher loss in wave energy.

The acoustic impedance can be described as the product of speed of sound [m s^{-1}] through the material and the density of the material [kg m^{-3}]. Liver tissue has been reported with a speed of sound of 1040 m s^{-1} and a density of 1060 kg m^{-3} [33]. The acoustic attenuation of soft tissues scale approximately linear with frequency. The acoustic attenuation of healthy liver tissue is reported in between 0.4-0.7 dB cm^{-1} MHz^{-1} [34].

In short, for the reconstruction of ultrasound images, important variables are the acoustic impedance and acoustic attenuation.

Visual reconstruction of a healthy Liver A healthy liver appears as a homogeneous texture with an echogenic fine smottled pattern. Other structures, visible with a low greyscale on the ultrasound image, are arteries, ducts and vessels. A diseased liver is marked with a nodular surface, where as a healthy liver shows a smooth surface. In figure 2.9 a healthy liver is shown [35], with characterizing smooth surface, heterogeneous appearing and low echogenic hepatic vasculature structures.

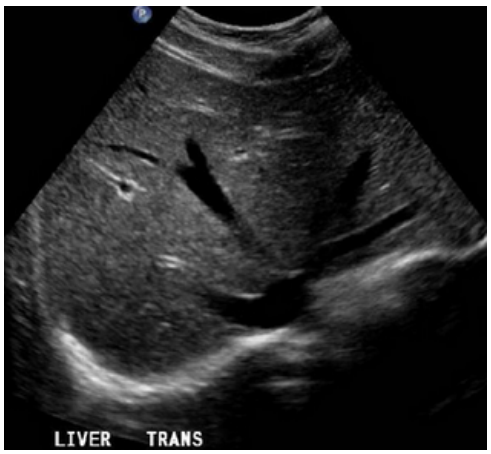

Figure 2.9: Ultrasound image of a healthy liver. Adopted *from* Ultrasoundpaedia, 2017. Accessed on: 17-11-2017.

Visual reconstruction of a diseased Liver As mentioned before, the appearance of a cancer infected liver is different than a healthy liver. Hepatocellular carcinoma is revealed by a hypo(darker) or hyper(lighter)-echogenic area where a homogeneous texture is expected. The size and brightness of the diseased area can differ per person. In figure 2.10, both hypo and hyper-echogenic metastases are shown [36]. Other typical characteristics are nodular regeneration (change in surface smoothness) and ascites (fluid accumulation in the abdominal cavity).

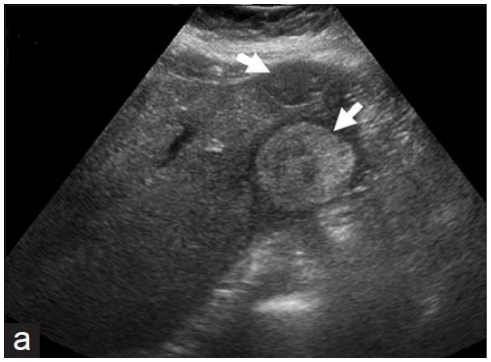

Figure 2.10: Ultrasound image of a diseased liver with hypo and hyper-echogenic metastases (white arrows). Adopted *from* Study blue Inc., 2017. Accessed on: 17-11-2017.

2.2. Interventional radiology

Interventional radiology is a collective term which covers procedures to treat a disease and also includes imaging techniques and other methods to make a di-

agnosis. An interventional radiologist provides minimal invasive image-guided diagnosis and is able to treat a patient with the least invasive technique to minimize risk and improve recovery time. In this section, the most general treatment methods are discussed. The interventions are divided into general treatment by biopsy, ablation and embolization.

2.2.1. Biopsy

Biopsy is one of the oldest interventions to obtain knowledge about the state of a tissue. By performing a biopsy, the practitioner introduces an instrument into the body to obtain a piece of the desired tissue. This procedure is fairly straightforward and helps in making the right diagnosis by directly assessing the state of the tissue via microscope inspection.

A liver biopsy can be performed in several ways. Firstly, a percutaneous liver biopsy which is done with the use of a needle which penetrates the skin and directly reaches through in the abdomen to the area of interest, as shown in figure 2.11 [37]. This type of biopsy is executed most commonly and can be done blindly, visually guided at laparascopy or guided via ultrasonography or computed tomography [38]. Secondly, a transvenous liver biopsy is done via the neck, where a sheath is guided down into the jugular vein, along the side of the heart, into one of the veins in the liver. This is procedure is carried out on patients who are therapeutically anticoagulated, or in a situation where excessive bleeding may occur during a percutaneous biopsy [39].

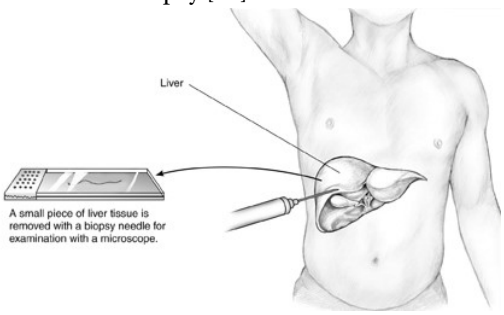

Figure 2.11: Procedure for a percutaneous liver biopsy. Adopted *from* NIDDK, 2014.

2.2.2. Ablation

Ablation therapy has as purpose to kill cancerous cells instead of removing them from the body. Next, is discussed that ablation can be done via chemical or thermal means and what the working principle is behind the treatment.

Chemical ablation During this treatment, a chemical compound is administered to the tissue which blocks the normal functioning of the affected cells and consequentially killing the cells. Agents which are commonly used for this therapy are ethanol and acetic acid. The agent is percutaneously injected into the tumor and exerts the cytotoxic effect through a cytoplasmic dehydration, denaturation of cellular proteins, and small vessel thrombosis [40]. An ethanol agent however has difficulties penetrating tumor septa and also is less able to fully diffuse within the tumor. Hence, for the treatment of large tumors (> 3 cm in diameter) ethanol is less suitable. Study shows that acetic acid is able to diffuse through tumor septa and furthermore a same volume of necrosis can be achieved with the use of a smaller doses, compared to ethanol [41].

Thermal ablation Many techniques are available to locally change the temperature of the desired tissue, which induces necrosis. Increasing the temperature to 46 °C for 60 minutes results in irreversible cell damage. When the temperature is increased even more to 50-52 °C, it even shortens the time necessary for irreversible damage [42]. Techniques used for hyperthermia configuration are radiofrequency ablation (RFA), ultrasound ablation, laser ablation and microwave ablation. Cryoablation is the only intervention which uses a decrease in local temperature, subjecting the tissue to hypothermia [43]. Each technique, although similar in purpose, has specific and optimal indications [44]. As visalisation, in figure 2.12, a RFA procedure is shown [45].

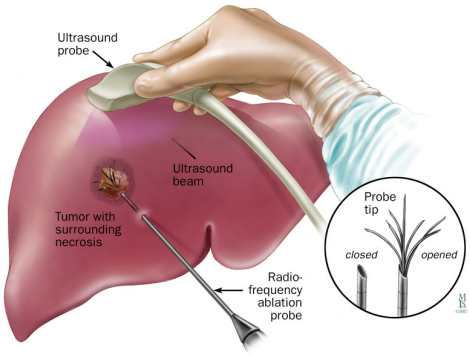

Figure 2.12: Radiofrequency ablation (RFA) in liver cancer under ultrasound guidance. Adopted *from* The John Hopkins University, 2017. Accessed on: 17-11-2017.

2.2.3. Embolization

Embolization can be used to reduce the amount of blood flow towards a malignant tumor, thereby reducing potential growth rate. Most cancer cells receive their blood flow from the hepatic artery whereas normal liver cells are fed by the portal vein. By cutting off the blood flow of the branches of the hepatic artery the cancer cells will grow slower while healthy liver cells remain unharmed.

Chemoembolization Chemoembolization is the combination of embolization with chemotherapy

and is also referred to as trans-arterial chemoembolization. Small beads are injected into the branches of the hepatic artery containing a chemotherapy drug. In the study of Choi et al. [46], the authors investigated the therapeutic effect of chemoembolization for encapsulated nodular HCC and found that the best effects are observed for a complete retention of the chemical agent and surrounding liver, which showed 100% necrosis. Further study reveals that trans-arterial chemoembolization improves survival and no difference is noted between chemotherapeutic agents [47].

Radioembolization Radioembolization combines the embolization procedure with radiotherapy, which can be done by administering microbeads that contain a radioactive isotope and put them into the hepatic artery. The beads nestle themselves in the vessels near the tumor, letting their radiation go in small amounts to the tumor in a certain timeframe. The radiation only travels a short distance and therefore affects mainly the malignant cells [48].

2.3. Phantoms

Phantom studies are often used as an alternative to *in-vivo* experimental configurations. These studies provide an easy-to-reproduce and controlled environment to simulate the right conditions. Ideally, a phantom model should fulfill all the functional requirements equally if compared to a like-wise *in-vivo* tissue experiment. In this section, the factors of influence on the requirements on the phantom model are discussed. Additionally, the field of application and possible materials will be addressed.

In order to come with a new design, existing designs are analyzed on working principle. The designs are assessed per functionality. The functionalities presented are: Respiratory movement and physical properties of TMMs. Physical properties of TMMs is further divided into the following subcatergories: Ultrasound Imaging Properties, Mechanical Properties and Multilayer. Other functionalities of a phantom can be integrated perfusion and tissue deformation, but are not presented because they are found not relevant in this work.

2.3.1. Respiratory movement

The first functionality of a phantom which is discussed, is the tissue motion and deformation in consequence of respiration. Due to the fact that the human body is a dynamic structure, it is necessary to regulate the movement of the desired volumes. The respiratory movement does not only induce motion but also deformation of tissue. Several studies are reviewed with examinations of the motion platform and the ways deformation is integrated.

Translation and deformation The liver itself shows displacements of 10-25 mm during quiescent physiologic breathing and up to 55 mm during maximum respiration and is mainly in a cranio-caudal direction [49, 50]. Deformation is approximately 10 mm over the entire liver and showed a maximum deformation of 34 mm in one place. The amount of deformation is extracted from MR images [51]. In a different study, deformation varied between 10 mm for shallow breathing and 15 mm for deep breathing [52]. Translations in other directions are observed to be between 1 and 12 mm in anterior-posterior direction and between 1 and 3 mm in left-right direction. Rotations do not exceed 1.5 degrees [53]. Just like the liver, most organs in the upper abdominal cavity will experience motion and deformation due to respiration. The heart shows a typical deformation of 3-4 mm measured from full exhalation to full inhalation [54]. A typical waveform is show in figure 2.13and noted is that this is not perfect a symmetrical signal [55]. The amplitude differs for each breath, just like the time period and sporadically pause breaks within the breathing cycle.

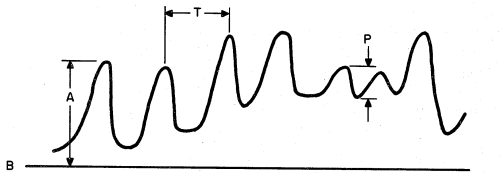

Figure 2.13: A typical respiratory signal over time, where A is the amplitude; T is the period and P indicates a pause. Adopted *from* Barker ,1982.

Designs Current study already reveals the use of respiratory motion phantoms which are MRI compatible. Tavallaei et al. [13] use a custom fabricated linear motion stage constructed from nonmagnetic materials. Actuation is achieved by an ultrasound motor and transmitted by a nut-screw connection. The range of travel was designed to be capable of replicating the respiratory motion, where a maximum peak-to-peak excursion of 21.8 mm is reproduced. The schematic setup of the phantom is shown in figure 2.14. The setup has been tested and results indicate that the system is MRI-compatible and able to facilitate reliable and reproducible motion. Limitations are the operational temperature of the ultrasound motor, which is $45°C$ and change in operation characteristics as the the temperature rises. Furthermore, the phantom solely contains an actuation part and is not integrated into an embedded design.

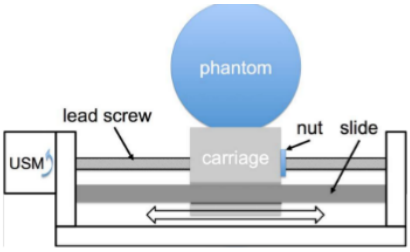

Figure 2.14: Schematic view of a MRI compatible motion phantom driven by an ultrasound motor. Adopted *from* Tavallaei et al., 2016.

A computer controlled pump system has been developed by Lin et al. [56] to recreate a variety of natural breathing patterns and has integrated the construction into an anthropomorphic respiratory phantom. Due to the control of the pulmonary cavities, the system is able to facilitate chest movement. Imaging of the movement is done via CT visualization of the cavities. Difficulties were observed in fully simulating the breathing, for the model cannot simulate the mechanical interaction between the diaphragm contraction and the plurea, where the authors observe that a larger tidal volume is needed to create similar chest wall displacement. Yet, they state that 'the larger tidal volume required does not affect the effectiveness of this platform as a validation tool, as long as we can accurately compensate for the difference in volumes to achieve human-like motion'. So, the model is still suitable to replicate human breathing motion.

In a different study the effects of fractionated radiotherapy delivery on a breathing, anthropomorphic, tissue-equivalent phantom have been investigated. The phantom is constructed from perspex which resembles the thoracic cavity and two 'lungs' are mounted inside and consist of accordion-type flexible hose with collapsible sides. Breathing motion is induced by a 3D positioner gantry with motion controller. The space around the lungs are filled with water and the 'lungs' itself are filled with damped sponges to simulate similar lung density for the CT scan [57]. The authors conclude that a higher amplitude of motion results in a higher degree of blurring, thus creating an underdosage on the planning target volume.

2.3.2. Tissue mimicking material

In this section some of the most common tissue mimicking materials (TMMs) are described. The presented TMMs are described in ultrasound imaging properties, mechanical properties and multi-layer designs.

As mentioned before most common base materials used for phantom models are: agarose, gelatin, polyvinyl alcohol (PVA-C), polyvinyl chloride (PVC), silicone [8]. Used TMMs in the design phase are PVA and PVC. Only these TMMs are presented, since other TMMs are regarded as less suitable. The suitability is based on the findings in the work of Pluymen [9].

Ultrasound imaging properties As mentioned for the liver, important ultrasound imaging properties are ultrasound impedance and ultrasound attenuation. The two variables depict the visual reconstruction of the material. In this work, the two variables for the used TMMs are not characterized. Only, the visual reconstruction will be investigated. This is done, because only the visual reconstruction is needed for US-guided needle insertion. Visual reconstruction of PVA and PVC is shown in figure 2.15 and 2.16. As noted from the images, the scattering in PVA sample looks more like the us reconstruction of liver tissue than the PVC sample.

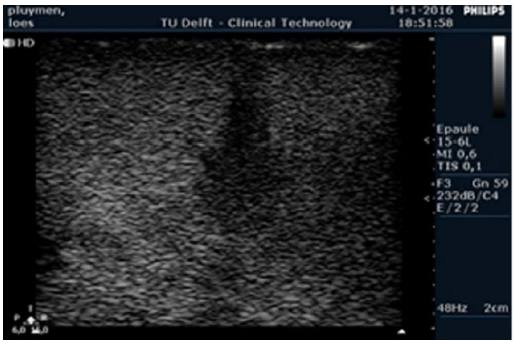

Figure 2.15: Ultrasound visual reconstruction of 7%m PVA sample. Retrieved *from* Pluymen, 2016.

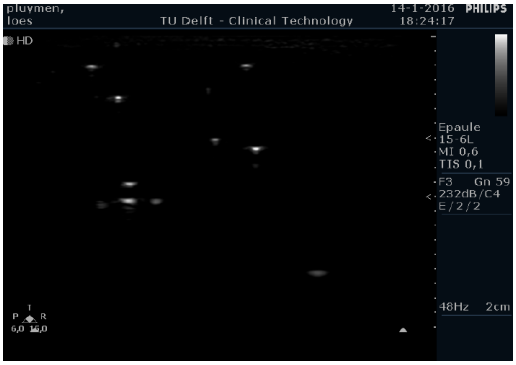

Figure 2.16: Ultrasound visual reconstruction of 100% plasticizer PVC sample. Retrieved *from* Pluymen, 2016.

Mechanical properties The mechanical properties of a TMM determines the needle-tissue interaction. The elastic modulus describes the stiffness of a material. The stiffness is a material property and has, as before shown in figure 2.6, an influence on needle forces, needle deflection and tissue deformation [27]. The TMM elastic modulus is characterized

in different studies with different experimental setups. Therefore, together with the visco-elastic material properties, results vary. The elastic modulus characterization of PVA, PVC with test principle is noted in appendix A. The elastic modulus provides only a guidance in the final choice of materials and production method.

Multi-layer designs Most of the physical models only consist of a single, homogeneous substance, where in reality the tissue is heterogeneous, anisotropic and can be defined by multiple layers of different tissue. Existing designs of multilayered phantoms are described below.

In a study of Saager et al. [58] a multi-layer phantom is constructed from silicone. The design in this work is made for the validation for optical instrumentation. The silicone phantom is able to mimic the optical properties physiologic tissues such as skin. Further, a patented multi-layer design consists of a container with a water-based phantom, such as gelatin and scattering agent for better ultrasound imaging. The container is sealed with a film, which acts as window for ultrasound imaging [59].

In a different study the mechanics of rupture events during transition between tissue layers is investigated [60]. From the research, the insertion velocity proves to have an effect on needle force, tissue deformation and needle work. Concluding, the researched confirmed that most benefit, in terms of least fluctuation of forces and work, can be achieved using a speed that is inversely proportional to the relaxation time of the tissue.

From literature review can be said that there are not many phantoms which include multilayered design with US-guided needle insertion. Yet, to give the liver its motion freedom, it is desired that the liver model will be a separate object.

2.4. Summary

Summarizing, many phantom studies have been conducted over the years, yet a phantom which combines respiratory motion with similar needle-tissue force interaction is not found in literature. The integration of the respiratory motion into a liver phantom and the needle-tissue interaction in this structure can improve the phantom model in terms of resemblance of reality. Knowledge about the respiratory motion vectors is limited and are key in the success for the development of a respiratory phantom. Therefore, in chapter 3 a separate study is done into the liver motion. Further, other preferred functions include appropriate tissue properties for imaging techniques. TMMs PVA and PVC are taken into the design phase for development of a liver model.

Integration of respiratory motion, appropriate needle-tissue interaction and US-guided needle insertion into one model, can provide a phantom which is able to simulate a dynamic range of test configurations.

3

Respiratory motion of the Liver

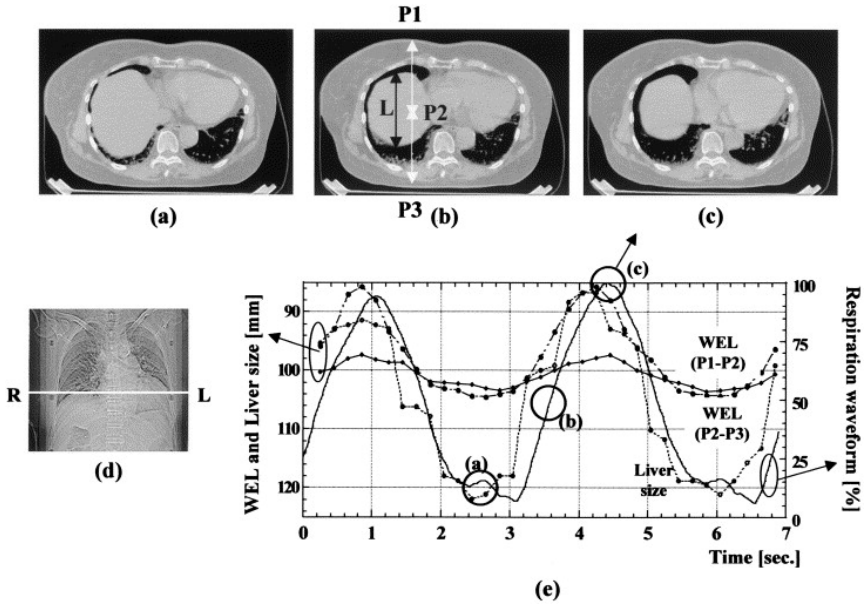

Figure 3.1: Respiratory Signal and liver motion over time. Adopted *from* Minohara et al., 2017.

In order to simulate respiratory motion patterns in a liver phantom, the trajectory of the liver is investigated. In this chapter, research into the motion pattern of the liver and ribs is presented.

3.1. Introduction

The liver is in direct contact with the diaphragm, situated in the upper right part of the abdominal cavity. As mentioned earlier, the liver moves as a consequence of the contraction of the diaphragm and intercostal muscles. To describe the liver motion over time, the respiratory signal as shown in figure 3.1 can be used as a reference [61]. The muscle contraction of the diaphragm as shown in figure 3.2, dictates the motion of the liver, because of the direct contact [62].

The breathing sequence can be described as follows:

1. Commencing at the maximum expirational state, the diaphragm and intercostal rib muscles are relaxed and untensioned leaving the liver situated high in the abdominal cavity.
2. Sequentially, the respiratory signal drives the diaphragm and intercostal rib muscles to contract, thereby shortening the diaphragm muscle and widening of the thorax circumference. The muscles in turn force the liver in dominantly cranial direction and possibly also anterior and left or right direction.
3. Once reaching the maximum inspirational state, the muscles release tension followed by the ribs and organs searching for the way of least resistance. The lungs are in overpressure and the ribs are tensioned in maximum inspirational state. Due to the volume difference the ribs will move as well, in order to allow the increase of volume.
4. When the muscle tension is released, the air in the lungs will naturally flow outward due to pressure difference with the athmosphere and the ribs compress to their resting state due to their spring characteristics. The diaphragm lengthens and the liver regains its place in the upper right part of the abdomen [61].

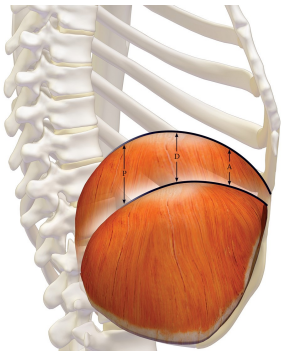

Figure 3.2: Physical representation of the diaphragm contraction during respiration. Adopted *from* Long, 2015. Accessed on 2017-11-17.

3.1.1. Problem statement

In previous studies, motion patterns between inhalation and exhalation of multiple volunteers have been described [53]. Translations were found dominantly in crano-caudal direction but motions in anterior-posterior and left-right direction direction were quantified as well [63]. However, literature only provides limited knowledge about the liver and rib motion in combined directions and has no information about the subject-specific motion vectors. Therefore, there is chosen to extract the motion paths from real cases.

3.1.2. Research goal

In this section the research goal is presented. Since, there is only limited knowledge about how the liver and ribs quantitatively move and the different motions between subject, the following research goal has been set:

"Determine the motion pattern in terms of translations of the human liver and ribs between inspiration and expiration."

3.2. Methods

The respiratory motion pattern of the liver and 7^{th} rib is extracted from in-house abdominal CT scans of real patients (resolution range in CC direction: 0.40-0.74 mm) during inspiration and expiration. The including criteria for CT scans are based on visibility, firstly the scans of each patient should at least contain one scan of the liver and 7^{th} rib at cartilage transition to the sternum in inspiration state and one in expiration state. Secondly, the liver and 7^{th} rib and should be fully captured on both scans. The tracking point are shown in figure 3.3.

The influence of the motion of the heart on the liver or ribs is not included in this study, because the rithmic interference by the heart has relatively little influence on the spacial outcome (1-4 mm, close to the heart) than the respiration [64] and this study will focus on translation and not rotations since they are relatively small (1.5°) [53].

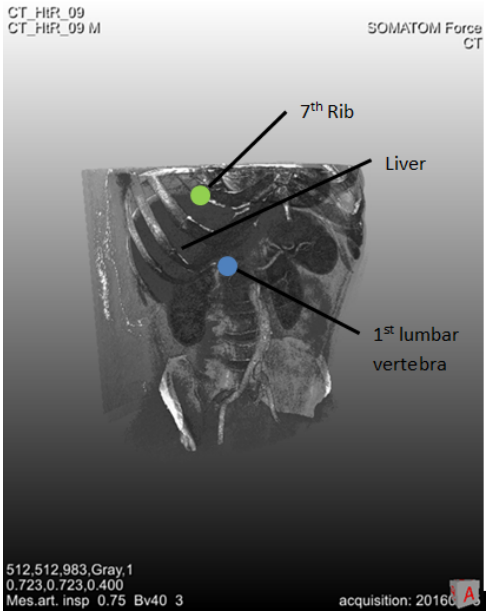

Figure 3.3: Locations of the relevant tracking points on the organic structures.

Motion patterns are determined by comparison of the shift in center of mass (CoM). The CoM is determined by averaging over all the sampling points and is described by the following equation:

$$CoM_{x,y,z} = \sum_{i=1}^{n} \frac{S_{x_i,y_i,z_i}}{n} \tag{3.1}$$

where, $CoM_{x,y,z}$ is the average CoM coordinate; S_{x_i,y_i,z_i} is the local coordinate and n is the number of samples.

Samples are extracted from the CT scan with MeVisLab 2.7.1 (MeVis Medical Solutions AG, Bremen, Germany). The liver is segmented, which means that samples are taken from series of semi-repetitive segments. Point allocation on the segments is done manually, since automated segmentation is prone to errors due to the low contrast with surrounding tissues [65] and has low accuracy [66]. The liver is sampled in 3 planes, sagittal, coronal and transverse, beginning top to bottom, starting at first top slice with notable liver tissue. The same procedure is done in anteroposterior direction, commencing at the first notable anterior slice and in left-right direction, starting at the first notable left slice. In each perspective, the liver is segmented in at least 5 slices.

Further, the 7th rib at the anatomical right side is tracked for insight into the relative motion of the ribs due to respiration. The center of the 7th rib at the cartilage transition to the sternum in coronal perspective is used as tracking point. Tracking is done manually. The 7th rib is chosen for tracking, because it is approximately at the similar CC position as the diaphragm. The tracking at the cartilage transition is done, since it is relatively well visible on the CT scan.

As a verification procedure, the 1st lumbar vertebra is analyzed to deduce relative motion and to check if the patient laid still during the measurements. The hypotheses is that the 1st lumbar vertebra shows only limited motion due to respiration. The vertebra motion is obtained from the same CT scans where the liver motion is distilled from. A single tracking point of the vertebra is chosen in the center of the anterior edge.

Samples are processed in Matlab 2017a (MathWorks, Inc., Natick, USA). The average coordinates of the CoM in both inspiration and expiration state are calculated and compared to obtain the translations of the liver and 7th rib during respiration. Secondly, the gross deformation modes of the liver are obtained from Matlab to qualitatively investigate global deformation.

3.3. Results

The available CT scans of 40 patients are subjected to the selection criteria. Only the CT scans of five patients pass the criteria. The segmented point clouds are fed in Matlab for visualisation and analyses, as shown in figure 3.4. The values of the points are directly obtained from MevisLab and are expressed in mm. The measurements enable the calculation of relative motions.

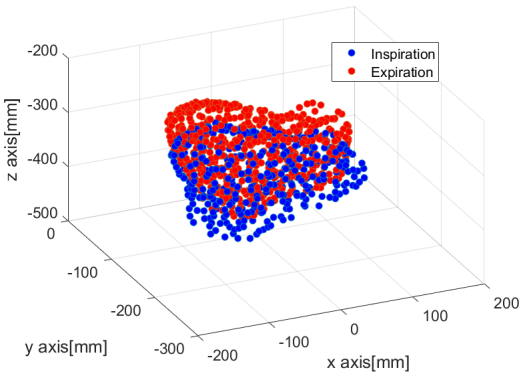

Figure 3.4: Point cloud segmented liver from CT scan in inspiration (blue) and expiration (red) state.

Liver translations Amplitude and angles of the motion paths between inspiration and expiration are visualized in figure 3.5. The translations range from 9.3-31.0 mm in CC direction, 2.7-20.7 mm in AP direction and -0.75-15.4 mm in left-right direction. Note that the positive direction is inverted for readability. Positive values are indicated as the direction of the black arrows in figure 3.5. Motion vectors are reported in table 3.1.

Table 3.1: Overview of the extracted liver motion vectors.

Patient #	CC [mm]	AP [mm]	LR [mm]
1	21.46	15.11	14.09
2	30.98	2.66	15.42
3	24.75	20.74	8.47
4	22.32	16.95	5.3
5	9.28	12.6	-0.75

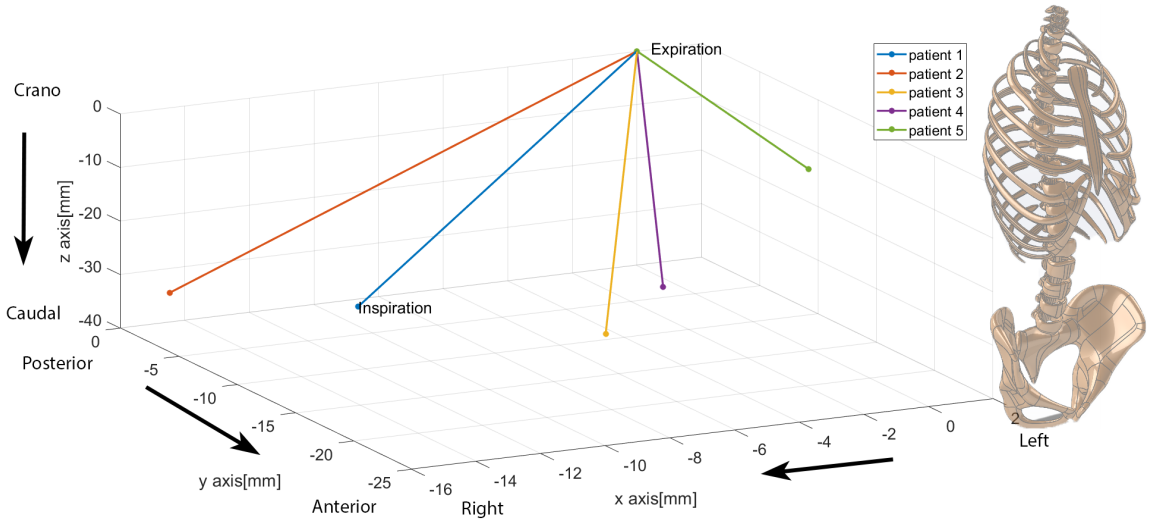

Figure 3.5: 3D CoM motion pattern between inspiration and expiration [0,0,0] state of all investigated patients. Perspective is visualized by the upper body insert, where positive motion is reported as from crano to caudal; posterior to anterior and left to right.

Liver deformations In order to visualize deformation, the segmented point clouds are approximated by triplots from Matlab. The visualization results in a qualitative measure for global deformation. For visualization, patient 3 is selected, since it shows the median motion pattern of the five obtained motion patterns. All patients are reported in appendix B. Figure 3.6 and 3.7 show the motion of the connected points from state of inhalation (blue) to exhalation (red). The shape of the liver remains roughly the same and mainly shifts and slightly rotates.

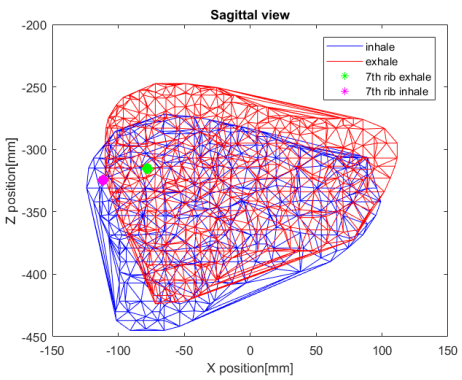

Figure 3.6: Saggital view of the deformation mode of the liver and relative motion of the 7th rib between inspiration and expiration.

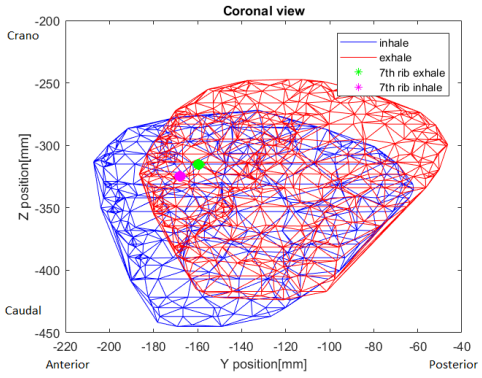

Figure 3.7: Coronal view of the deformation mode of the liver and relative motion of the 7th rib between inspiration and expiration.

Rib translations The ribs move as a consequence of respiration. The motion is dominant to the right (median: 18.95 mm) and in caudal direction (median: 18.85 mm), whereas relatively small movement in posterior direction is observed (median: 1.0 mm). The rib motion is reported in figure 3.8. The relative motion of the rib is also visualized together with the liver deformations in figure 3.6 and 3.7. All relative motion patterns are shown in appendix B.

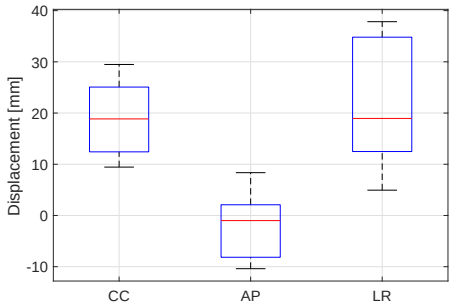

Figure 3.8: Relative motion of the 7th rib at catilage transition of 5 patients between inspiration and expiration. Motion in crano-caudal (CC), anteropostrior (AP) and left-right (LR) direction, respectively.

Verification procedure The CT scans are obtained in a dynamic environment where the patient is able to move, even if it is instructed to minimize movement. To verify validity of the liver motion due to solely respiration obtained from the CT data, the motion of the 1st lumbar vertebra is analyzed. In figure 3.9, the vertebra's motion is shown. Maximum motion (3 mm) is observed in anteroposterior direction (Y translation), with a median of 2 mm. Mean total (3D) translation of the vertebra is 1.86 mm.

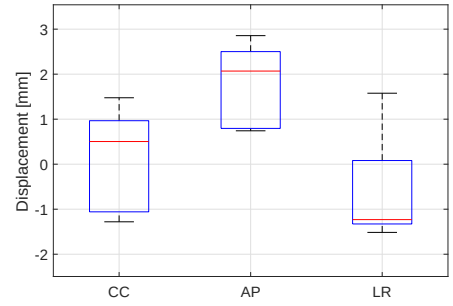

Figure 3.9: Relative motion of the 1st lumbar vertebra of 5 patients between inspiration and expiration. Motion in crano-caudal (CC), anteropostrior (AP) and left-right (LR) direction, respectively.

3.4. Discussion

The goal of the study was to determine the motion pattern of the liver between inspiration and expiration. The motion patterns of the liver can approximated by a motion in right, anterior and caudal direction from state of expiration to inspiration. The motions are in line with previous conducted experiments found in literature [67]. The motion pattern in this study are assumed to be linear from state of inspiration to expiration. In reality the motion can be non-linear.

The rib motion at the cartilage translation of the 7th rib is in the same order of magnitude as the liver motion, the direction however differs. The intercostal muscles and diaphragm pull the ribs outward and downward and not so much to the front.

The first lumbar vertebra is used for a verification procedure. The motion of the first lumbar vertebra is marginal compared to the motion of the liver in all directions. Therefore, the found liver motions originate from within the body and the patients did not move during the measurements.

The point allocation for the calculation of the center of mass has been done manually, and due to a limited time span, sampling rate has been reduced in respect to the given CT resolution. The downgrading of the spacial resolution can influence the accuracy of the determination of the CoM coordinates. Sequentially, the motion pattern might be different. However, due to the averaging over all points for CoM determination, the addition of more slices has percentage wise less and less effect on the mean CoM coordinates.

The manual selection procedure is prone for human error. Yet, automatic selection tools have problems with boundary detection and therefore, are less able to reconstruct the liver from CT scans [65, 66].

The scans are obtained in a setting which are not controlled by this work. The explanation for the spread in CoM translations is therefore not conclusive. The difference could be due to inter-subject differences.

The visualization of the triplots give a qualitative measure of the connection between points, but lack of information for a quantitative validation of deformations. Yet, the 3D plots are reconstructed from 2D CT images and will therefore always need interpolation.

3.5. Conclusion

Concluding, in this work, the goal was to determine the liver translations and rib motion. The liver translations have been determined. The liver moves in caudal, right and anterior direction, ranging from 9.3-31.0 mm in CC direction, 2.7-20.7 mm in AP direction and -0.75-15.4 mm in left-right direction have been found. Motions are cross checked by analyses of motion of the first lumbar vertebra. The vertebra's motion is found to be marginal, thus liver motion can be assumed to originate from respiratory motion. At last, the right 7th rib showed dominant motion in right and caudal direction, median 18.95 mm and 18.85 mm, respectively and relative little motion in anteroposterior direction, 1.0 mm.

4
Design process

The objective as mentioned in chapter 1, is to create an anthropomorphic liver phantom with respiration functionality and the simulation of similar needle-tissue interaction. In order to develop a prototype, a design process is used, which is presented in this chapter. Firstly, the design requirements are set. Continuing in a phase of conceptual design. Followed by an embodiment design and manufacturing.

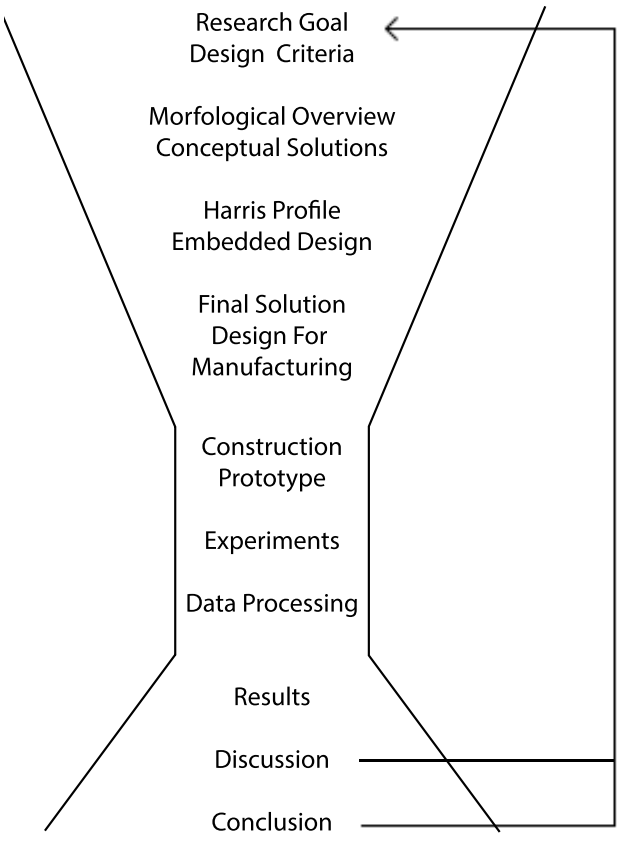

Figure 4.1: Structural overview of the design process.

Structure The design process of the project is shown in figure 4.1. Prior to the design process, the problem definition and the research goal are set in the problem analysis as introduced in chapter 1. In this work I will walk through a design process, commencing with the definition of design criteria, followed by conceptual design. During the conceptual design phase, I will make use of a morphological overview to help with the exploration of conceptual solutions. Continuing, with concept selection with the help of a Harris Profile [68] and further elaboration of 3 selected concepts. With elaborated knowledge of the three concepts, the final concept is chosen based upon the design criteria and additional wishes. The final concept is then further developed for manufacturability, followed by a production phase to a prototype. The prototype is presented in chapter 5. Experiments, data-processing and results are presented in chapter 6 as an evaluation of the design criteria. Finally, the work is concluded in a discussion and conclusion in chapter 7 and 8, respectively.

4.1. Design requirements

The design requirements control the design of the project through the design process and are determined after assessment of literature. In table 4.1, the design requirements are summarized.

Table 4.1: Overview of the design requirements

Design criteria	**Requirement**	**Literature**
Anthropomorphic liver kinematics	CC direction: 0-31 mm	Own study
	AP direction: 0-21 mm	Own study
	LR direction: 0-15 mm	Own study
Adjustability	Able to adjust motion pattern	Own study
Anthropomorphic mechanical properties	Friction slope: 0.015 - 0.05 N mm^{-1}	de Jong et al. [5]
	Amplitude peak forces: 0.1 - 0.8 N	de Jong et al. [5]
	Amount of peak forces: >8 #/dm	de Jong et al. [5]
Anthropomorphic liver dimensions	CC direction: 147.4-181.1 mm	Own study
	AP direction: 126.7-198.5 mm	Own study
	LR direction: 183.3-221.4 mm	Own study
Anthropomorphic liver volume	0.940-2.344 dm^3	Henderson et al. [69]
Compatible with ultrasound imaging	Ultrasound needle guidance possible	Hodge et al. [70]

Anthropomorphic liver kinematics One of the requirements of this work is to simulate anthropomorphic liver motion by respiration. In chapter 3, the motion is investigated and requirements are therefore set to 0-31 mm, 0-21 mm and 0-15 mm in CC, AP and LR direction, respectively.

Anthropomorphic mechanical properties Another requirement is that the needle-tissue interaction is able to simulate response like liver tissue. Since, interventions are performed mostly on diseased tissue, the requirement are estimated for cirrhotic liver tissue instead of healthy tissue. In the study of de Jong et al. [5], healthy human liver tissue is characterized in terms of axial needle forces during insertion and retraction. The three used metrics are: friction slope, amplitude of peak forces and amount of peak forces ,valued 0.011 [N mm^{-1}], 0.179 [N], 7.27 [#/dm], respectively. Cirrhotic liver tissue increases in stiffness [2], therefore an increase in needle friction slope is desired. The friction force on the needle shaft is the result of the internal stiffness of the inserted material [27]. Due to a higher heterogeneity in cirrhotic tissue, the amplitude and amount of peak forces are chosen such that they are higher than healthy liver tissue. The design requirement for the mechanical properties are: 0.015 - 0.05 N mm^{-1}, 0.1 - 0.8 N, >8 #/dm for friction slope, amplitude of peak forces and amount of peak forces, respectively.

Anthropomorphic liver dimensions The liver itself comes in many shapes and sizes, and alters in different pathological states. In literature, the specific dimensions in CC, AP and LR direction are quantified for healthy livers. The average liver dimensions are 15-17.5 cm, 10-12.5 cm, 21-22.5 cm in CC, AP, LR direction, respectively [33]. From the available CT scans used in chapter 3, the dimensions are extracted from the five selected patients. The segmented liver is boxed in CC, AP and LR directions. The distance between the two parallel planes is used as the CC, AP and LR dimension, respectively. These distances are set for the anthropomorphic liver dimensions. Obtained dimensions from the five patients are as follows:

Table 4.2: Overview of the extracted liver dimensions

Patient #	CC [mm]	AP [mm]	LR [mm]
1	147.4	198.5	193.1
2	168.0	165.2	192.2
3	176.4	140.0	221.4
4	181.1	136.0	215.3
5	158.6	126.7	183.3

The volume of the liver model acts as an additional metric for the liver dimensions. Since, the liver is a-symmetric and organically shaped, liver dimensions expressed in CC, AP and LR direction can have variable outcomes in terms of volume. The range for the liver volume is set to the mean plus and minus 1 standard deviation found in Henderson et al. [69].

Compatible with ultrasound imaging The last requirement is that the phantom is compatible with ultrasound(US) imaging for needle guidance. US imaging is the most commonly used imaging method in interventional radiology, since it is cheap, simple and easy to use [70]. Therefore, the phantom should allow ultrasound-guided needle insertion.

Wishes Additionally to the design requirements, design wishes are added. The wishes are kept in mind

during the design process for a more desirable end result. The design wishes are as follows:

- The design should be simplistic, meaning the use of the minimal amount of parts.
- The design should be maintainable, meaning that parts are easily replaced.
- The design should be cost effective, meaning that only essential expenses are made.
- The design should simulate rib motion due to respiration.

4.2. Conceptual design

In this section the creation and assessment of the conceptual solutions is elaborated. The main purpose of the design is to move and to perform the same needle-tissue characteristics as a real human liver. As a first step in concept design, the system is separated into four elementary parts:

1. Structural Support
2. Functional Structure
3. Actuation
4. Surroundings Simulation

The four elementary parts divide the problem at hand in more comprehensible pieces. For each subsystem, a separate solution can be found after which each subsolution can be combined to fit the whole problem. Below is a description of each subsystem:

- Structural support: subsystem which will provide the connection to the solid world and maintains the other subsystems in a controlled position.
- Functional structure: subsystem which reenacts as the liver.
- Actuation: subsystem which will provide respiratory motion upon the functional structure.
- Surroundings simulation: subsystem which will function as surrogate for the abdomen.

In a later stadium, the integration of sensors and measurement equipment will be examined and discussed. Even though that these parts are separated for design generation, it is necessary to keep in mind, that all parts could influence the motion modes of the phantom.

4.2.1. Morphological overview

The subsystems can be visualized in the form of a morphological overview as shown in figure 4.2. The morphological overview gives insight in the possible solutions for each subsystem. Note that there could be many more solutions to all the subsystems, only the visualized subconcepts are investigated further based on literature. Other subconcepts for the functional liver structure are excluded by inability to fulfill either the needed mechanical properties or ultrasound imaging properties.

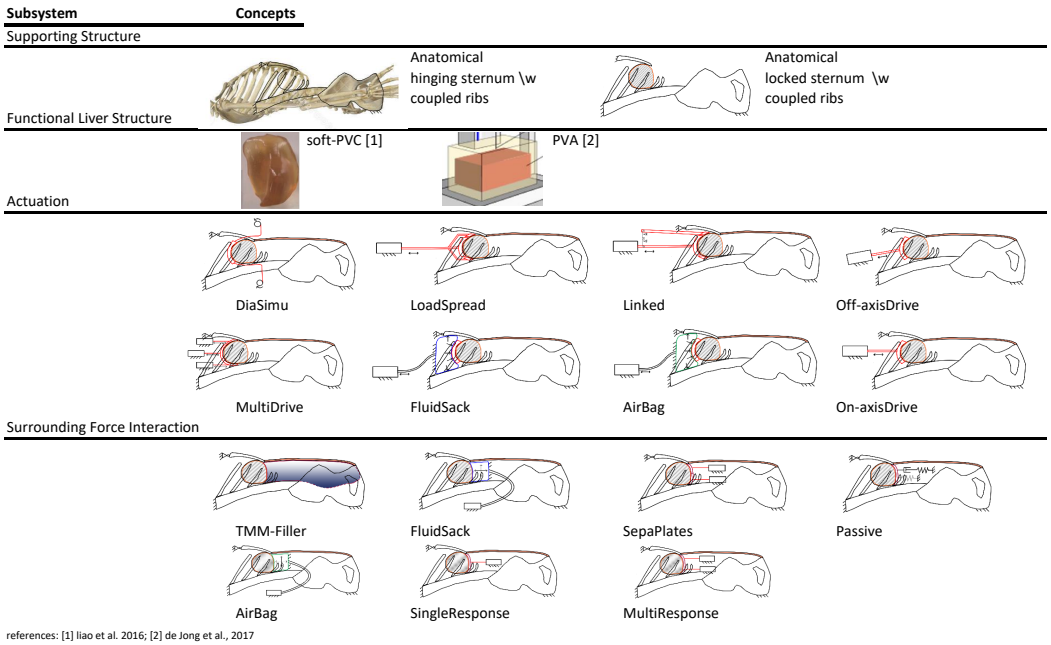

Figure 4.2: Morphological overview.

4.2.2. Conceptual solutions

By combining solutions to each subsystem, conceptual solutions can be generated, as shown in figure 4.3. The conceptual solutions provide a spectrum of differently constructed designs and thereby covering several perspectives on the problem.

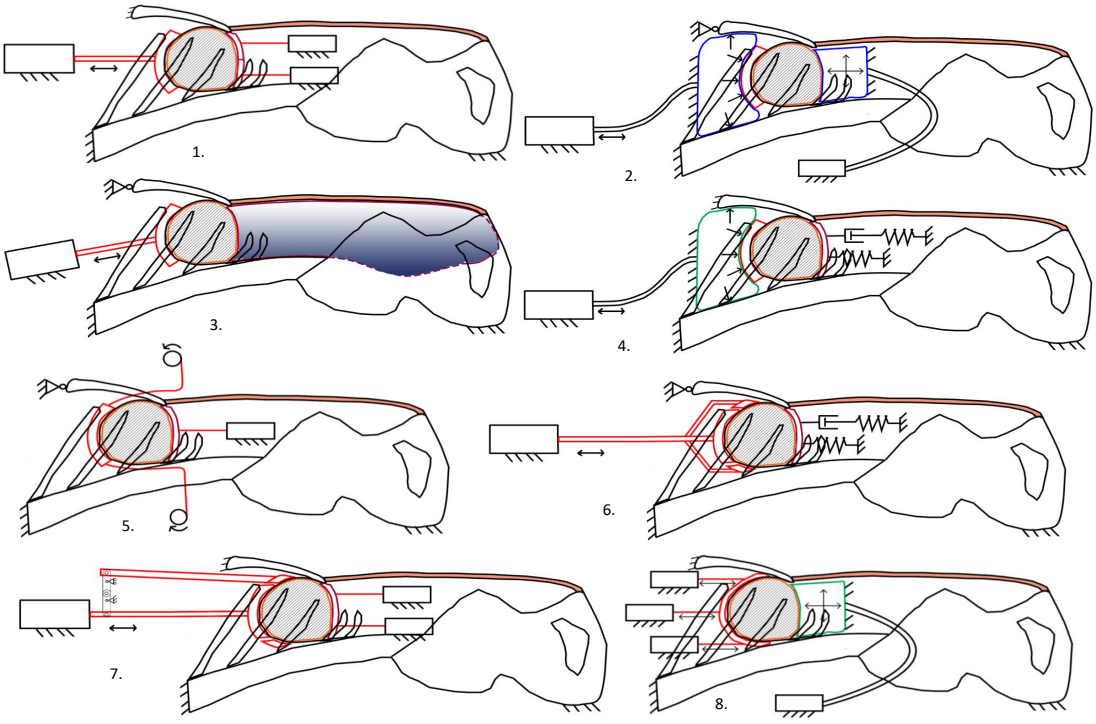

Figure 4.3: Conceptual solutions.

A short description explaining the key components of each conceptual solution is given below:

1. Single drive stage for actuation with multiple separated response pistons. The structural support with a clamped sternum and a PVC based functional structure.
2. Both actuation and response is generated with regulation of fluid volumes. The structural support with a rotational sternum and a PVC based functional structure.
3. Off-axis single drive with a tissue mimicking material for surroundings simulation. The structural support with a rotational sternum and a PVA based functional structure.
4. Lung-like actuation and a passive shape memory material as response unit. The structural support with a clamped sternum and a PVA based functional structure.
5. Diaphragm motion generates actuation while a single stage functions as surroundings simulation. The structural support with a rotational sternum with a PVC functional structure.
6. Single drive actuation with compliant load distribution to the functional structure and a passive shape memory material as response unit. The structural support with a rotational sternum and a PVA based functional structure.
7. Single drive with a separation of loads and displacements to the functional structure and multiple response motors. The structural support with a clamped sternum and a PVC based functional structure.
8. Multiple drive stage and an air chamber for surroundings simulation. The structural support with a clamped sternum and a PVA based functional structure.

4.2.3. Concept selection: assessment of strengths and weaknesses

To converge to a design solution which best fit the design criteria, the strengths and weaknesses of each conceptual solution are assessed. The assessment is presented in table 4.3.

4.2.4. Harris profile

A Harris Profile is created as another way for the assessment of the conceptual solutions. Here, the solutions will be assessed on the degree on which they comply with the design criteria. The scale ranges from -2, -1, 1, 2, where the rate is assigned by how well a concept is likely to score on each criteria.

In figure 4.4, the Harris Profile is shown. All conceptual solutions have been given a color coating which will be used as further reference. An extra weight of 2x is given on the criteria: Kinematics and Insertion Force, since these criteria are considered to contribute more to the value of a final design. In figure 4.4 the 'Kinematics' and 'Insertion Force' criteria are shown in saturated colors.

Table 4.3: Overview of the design specifications versus design requirements

Concept number	**Strengths (+)**	**Weaknesses (-)**
Concept 1	Simple actuation	Fixed action and reaction points
	PVC liver is able to handle depicted motions	
	Separation of response plates leads to more realistic mobility	
Concept 2	Pressure distribution is equal	Prone for leakage
	Reactive properties can be controlled	Expensive system
Concept 3	Simple actuation	Large volume of TMM needed
	Similar reaction forces from TMM	Limited lifespan of Surroundings
Concept 4	Actuation pressure distribution is equal	Prone for leakage
	Memory Shape Foam distributed pressure from surroundings	
Concept 5	Real diaphragmatic motion patterns	Motion delay of Surroundings
		Difficult motion control
Concept 6	Load distribution with compliant mechanism	Load distribution hard to predict
	Memory Shape Foam distributed pressure from surroundings	
Concept 7	Different displacement modes on actuation	Bad end-point control
		Expensive actuation
Concept 8	Multiple drives can locally control the motion	Prone for leakage
	Air sack can distribute response pressure	Expensive actuation

Criteria	Concept 1	Concept 2	Concept 3	Concept 4	Concept 5	Concept 6	Concept 7	Concept 8
	+2 +1 -1 -2	+2 +1 -1 -2	+2 +1 -1 -2	+2 +1 -1 -2	+2 +1 -1 -2	+2 +1 -1 -2	+2 +1 -1 -2	+2 +1 -1 -2
Kinematics								
Insertion Force								
Dimensions								
Adjustability								
Compatibilty								
Wishes								
Total (weighted/unweighted)	-2/0	2/2	6/3	6/3	-2/0	8/5	-4/-2	3/0

Figure 4.4: Harris Profile. The design criteria, Kinematics and Insertion Force are weight-rated 2x and shown with saturated colors, because they are considered to contribute more to the value of a final design.

From the Harris Profile, concept 3, 4 and 6 show the highest suitability with the criteria. These three concepts score high on 'kinematics and insertion force', since they all contain a PVA functional structure based on findings in Pluymen [9], whom concludes that PVA is best suitable to simulate liver tissue in terms of needle forces and heterogeneity, non-toxicity and other practical aspects.

4.2.5. Design criteria matrix

A different way to visualize the strengths and weaknesses is with the design criteria matrix as shown in figure 4.5. The concepts are rated on each of the six axis how well they will cover each criterion. As mentioned before, the criteria of 'Kinematics and Insertion Force' have a larger weight. If these two criteria are well met, the final design will be effective in solving the gap in designs for a respiratory liver phantom for needle-based interventions.

From the design criteria matrix again concept 6 (orange) shows the best suitability in 'Kinematics and Insertion Force' criteria and relatively average in 'Wishes, Imaging Compatibility and Dimensions'.

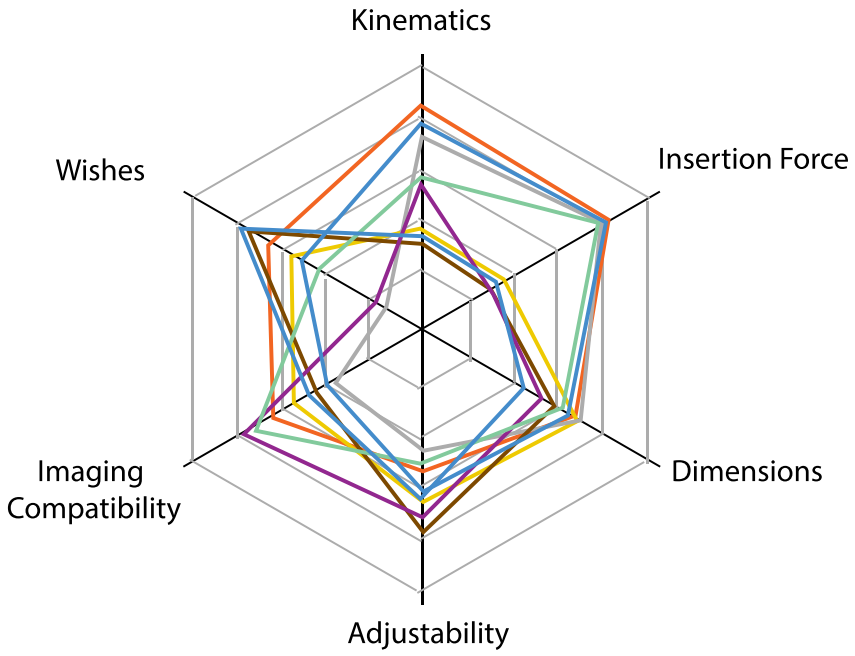

Figure 4.5: Design criteria matrix.

4.3. Embedded design

The embedded design phase includes a more defined design, particularly in cases where the level of conceptualization achieved during ideation is not sufficient for full evaluation. So where the preliminary design phase focuses on creating the general framework to build the project on, the embedded design phase defines the whole system configuration.

In the conceptual design phase three core solutions are chosen, which to a large extent cover the design criteria. In this phase the three conceptual solutions are further developed to an embedded design.

Concept 3 - filler In perspective of the wishes concept 3 will be respectively time consuming in producing the TMM filling as well as the liver in follow up experiments, because the TMM's lifespan is limited compared to a spring-damper design as in concept 4 or shape memory shape solution in concept 6. However, the material properties of the filler can be chosen to mimic the surroundings quite closely in both mechanical behavior as in image modality. Motor load can be calculated from the motion and deformation of the functional and surrounding structure. Indentation of the filler should be in the same order as the motion of the liver, which is distilled from the CT scans. The translation of the liver's CoM is on average 1.95 cm. Decomposed in [x-y-z] motion, [8.06 ± 6.31 ; 7.79 ± 11.26 ; 15.99 ± 10.01] mm, respectively. Assuming simple compression where the abdomen filler is approximated with an ellipsoid contact area, the following calculations can be made:

$$F = E * A * \delta l / L_0 \tag{4.1}$$

Where, F [N] is the force needed for the compression; E [MPa] is the elastic modulus of the filler; A [m^2], the contact area; δl [m] is the compression length and L_0 [m] is the initial length. Since the design needs to hold for the worst case loading, values from literature or own findings are chosen such that the resulting load is maximum.

$$\delta l = 1.95 * 10^{-2}\text{m}$$
$$L_0 = 25 * 10^{-2}\text{m} *$$
$$E_{avg} = 2000\text{N m}^{-2} * *$$
$$A = 197.135 * 10^{-4}\text{m}^2 * **$$

substituting in equation 4.1

$$F = 30.7\text{N}$$

*Estimated for a 24 yr male. ** Estimated average elastic modulus for the whole abdomen. *** Extracted from ct scan, calculated as ellipsoid area of the thorax at single coronal ct slice at height of the diaphragm minus cylinder shape spinal cord.

Substituting the parameter into equation 4.1, returns a load of 30.7 N. The calculation is an approximation which holds up to a compression of a tenth of the starting length for normal quiet breathing. This criterion is met, since $0.1L_0 > dL$. Even though this criterion is met, it is wise to note that the filler will react as a viscoelastic material. Viscoelastic material does not show a linear elastic behavior, therefore this calculation is only an estimation for the force loads. From the liver's CoM motion pattern can be seen that the liver moves both in crano-caudal, anterior-posterior and transverse direction . A motion stage which facilitates these degrees of freedom is desired. This makes an adjustable motion angle interesting to include in further concepts.

Concept 4 - lung Concept 4 key features are the lung-like actuation and the surroundings simulation by a spring-damper system. The lung-like actuation is relatively impractical to implement, because the air volume might be pierced during the intervention and all connections will have to be air tight in order to provide proper control of the pressure and motion. The surroundings are simulated by a passive spring-damper mechanism. Advantage of the passive spring-damper system is that it is simple and reliable, but might not be good enough in representing the mechanical properties of the surrounding tissues. Spring characteristics: The spring will have to simulate the same stiffness as the abdominal stiffness, earlier assumed with a simple compression in crano-caudal direction. As simplification it is assumed that there is equal compression between the contact area of the liver and the abdominal organs. To have stable compression at least four parallel springs need to be placed.

$$k = \frac{F}{\delta l} \tag{4.2}$$

,where k [N m^{-1}] is the spring stiffness; F [N] is the reacting force in compression for this use and δl [mm] is the displacement or compression length. From the calculations in section Concept 3, the reacting force from the abdomen is approximated as $F = 30.7$ N. The accompanied displacement extracted from ct scans is $\delta l = 1.95 \cdot 10^{-2}$ m. Thus, the total stiffness and stiffness per spring should be, respectively:

$$k_{total} = 1575\text{N m}^{-1}$$
$$k_{1,2,3,4} = 393.75\text{N m}^{-1}$$

Lung material/stroke: As an iteration, the spring damper system can be made active, provided by a

motor with proper control parameters. Thereby, giving opportunity in tuning the response of the surroundings at the final design. Pressure in the lung is the sum of the trans diaphragmatic pressure and the atmospheric pressure. Normal trans-diaphragmatic pressure hovers around 121 mm H2O or 0.01186 bar [71] and atmospheric pressure is 1.01325 bar. Complications in this concept can arise in the control of motion. The way that the lung will expand is unknown. The motion enforced upon the liver is depicted by the shape and the boundary conditions of the lung. Additional sensory feedback is needed to obtain the desired motion, whereas the end-point position of a direct drive motion stage as in concept 3 and 6, can be read out more easily (if the motor has an integrated position sensor).

Concept 6 – compliant Concept 6 uses a compliant mechanism which allows to distribute loads as desired instead of a single push. The surrounding tissues are simulated with shape memory foam, which can be shaped to the desired form and locks the liver in place. Shape memory foam has very specific mechanical properties. An aspect which needs investigation is the recovery speed. The foam needs to follow the motion of the liver, if not, there will be pressure loss and the liver is free to move which will most likely lead to undesired motion. Shape memory foam consists mainly from polyurethane (PU) and new generation foams react to heat and weight. All foams have viscoelastic properties to a certain extent [72]. To get an idea of the mechanical properties, literature is reviewed. PU foams have been tested by Maji et al. [73] and showed compressive yielding at 0.75 ± 0.03 MPa in rise direction for the 80 kg m3 density foam. The foams were tested in a hydrostatic compression test. The load on the material is approximated by the normal trans diaphragmatic pressure [71], at 121 mm H2O or 0.01187 MPa. So according to literature, the material should easily be able to withstand the load without yielding. An additional advantage is that the foam can be produced in 3D milling machine, allowing complex cut-outs. From the stress-relaxation curves presented in Tobushi et al. [74], a relaxation is observed of several minutes, which is too much for the application in this setting. The surroundings surrogate material needs to follow the motion of the liver, else contact is lost and the liver will move uncontrolled and image guidance is not possible.

Functional structure – liver

Based upon the design constraints the appropriate phantom material is chosen. Material selection is done based upon the physical properties of the material and behavior. The material is subjected to deformation, therefore the material should be able to withstand the deformations without breaking or shear failure, e.g. there should be no plastic deformation. Further, image properties of the material should be compatible with ultrasound imaging modality. In the work of Hungr et al. [8] near equal design requirements are determined. The material should be able to withstand deformation motion, be compatible with imaging modalities and be cost efficient. The authors concluded that agarose and gelatin were too fragile for the types of motion; Silicone has inappropriate acoustic characteristics and the CIRS phantoms did not show evident deformation and were expensive. Resulting in the choice between PVA-C, with a lengthy and complex production preparation procedure and PVC with softener dioctyl terephthalate, where preparation needs high temperatures and produces possible toxic fumes. The PVA mixture gives the best compromise between mechanical and imaging characteristics, without compromising safety concerns of the maker. Further, it is inexpensive, easy to manufacture, has a sufficiently large range of elastic modulus and has heterogeneous elastic properties whilst still resistant to rough handling. Thus, based on these findings, the liver phantom is constructed from PVA.

It is yet unknown if PVA is able to withstand the loads associated with respiration. This is investigated in a static and a dynamic compression test and will be presented in the detailed design phase.

The dimensions of the liver are determined from the readily analyzed point clouds. After analyses of the allocated point cloud, patient 3 is chosen to serve as model for liver simulation. The CT data is segmented a second time on a resolution of 1.6mm between slices in crano-caudal direction instead of the point allocation used in chapter 3. The newly obtained point cloud is fed in Solidworks and turned to a solid. Dimensions in each anatomical direction are as follows:

- CC direction: 174.57 mm
- AP direction: 119.76 mm
- LR direction: 226.53mm

Summary From concept 3, 4 and 6, the advantages are combined into an embedded design. The first embodiment design is shown in figure 4.6, where the anatomical support structure or skeleton is clearly visible. Inside the skeleton, the liver is fixated and actuated with a linear motion stage where the motion vector is adjustable at will. Response forces are generated by another linear motion stage, simulating abdominal tissue characteristics. To allow different

needle insertion angles, a transition TMM material is placed between the liver and the response motor stage.

- Single actuation motion stage with adjustable drive angle.
- PVA based functional structure.
- Anatomical similar support structure.
- Single drive response stage or preloaded spring with a TMM as the connecting part to the functional structure.

For the follow-up process the motor stages will have to be chosen, together with the drive angle and control for tissue simulation. Since, the abdominal tissue is relatively free to move, the degrees of freedom need to be preserved.

4.3.1. Detailed design

The detailed design phase further elaborates each aspect of the product by description through solid modeling, drawings as well as specifications.

As iteration on the previous phase, it is chosen to make the surroundings simulation passive, instead of active. This step is done because of practical consideration of cost effectiveness, less needed control and minimizing the amount of design parts. The surroundings simulation is provided by partially a spring mechanism and a counter-mold with holds the functional structure in place. The counter mold is also created from PVA. The CAD model of this iteration is shown in figure 4.7.

Compression test on PVA Compression tests on two PVA mixtures are done to observe potential loss of structural strength It is unknown if PVA is able to withstand compression loads resulting from respiration. Two sets of 4%w and 7%w PVA concentration, containing each three cylinder shaped samples, are made. The samples are conical, where the smallest diameter is 7.5 cm and biggest 8 cm and a 8 cm height. The pressure exerted on the liver is assumed to be equal to the transdiaphragmatic pressure (Pdi). Transdiaphragmatic pressure is measured in Rochester et al. [71] and is 0.121 N cm^{-2} for a normal person. As a certainty factor, the load is raised to 2.5 times the transdiaphragmatic pressure.

Method The three samples are placed in symmetric triangular formation in order to obtain a stable uniform loaded platform. The reason not to test on single samples is, load tests on single samples showed unstable behavior due to the inability to apply centered loads. For each set, the downward stroke is manually set to reach a load of at least 5.5 kg over the three samples covering 19.635 cm^2 (e.g. 2.5 x Pdi). Compression is performed 10 times on each set, with a 30 seconds relaxing period in between each downward stroke. The signal is filter with a butterworth filter with a 1000 Hz sample frequency and 50 Hz cutoff frequency for noise reduction. Sample production parameters are described in appendix C

Results The samples are compressed and showed no observable loss in structural strength. Force-time diagrams are shown in appendix D.

Discussion Both sample configuration, 7%m as 4%m PVA 2 FT, are able to withstand compression up to 2.5 times transdiaphragmatic pressure without yielding. A more elaborate interpretation is reported in appendix D. A limitation is that the sample size is relatively small and mechanical properties can differ per batch. From the results, it is reasonable to assume that PVA 4%m-7%m 2FT is able to withstand the transdiaphragmatic load.

Conclusion Concluding, both 7%m as 4%m PVA 2 FT is able to withstand the 2.5 times transdiaphragmatic pressure without yielding. Therefore, PVA 4%m-7%m 2FT can be used for the functional structure as well as the surroundings simulation.

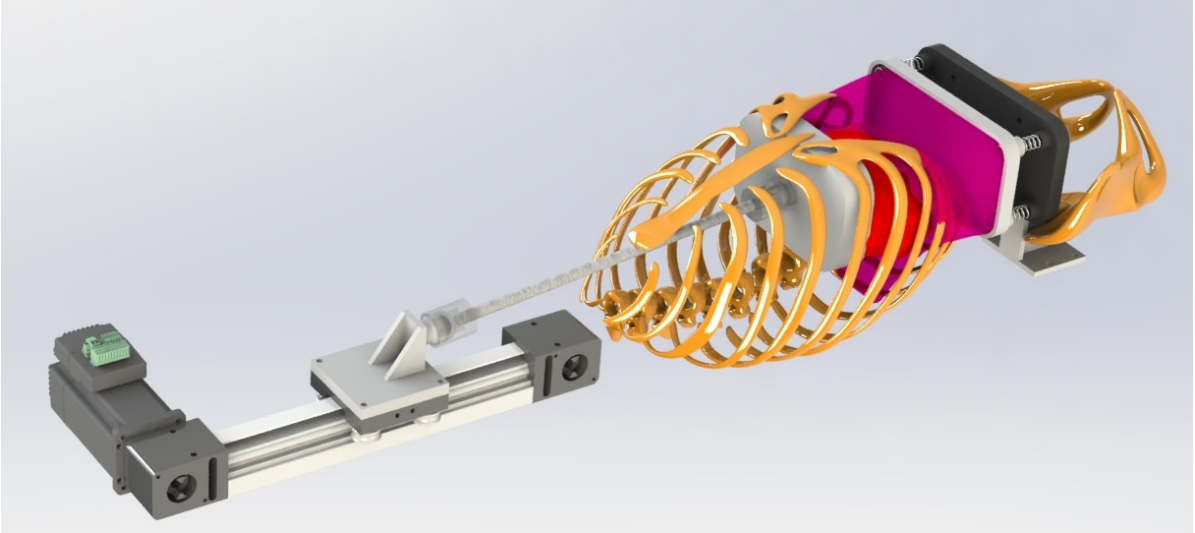

Figure 4.6: First 3D modeling concept.

Intercostal spacing In order to allow extracorporeal contact between the liver phantom and, the ultrasound machine and needle, an intermediate layer of tissue mimicking material is implemented. For the ultrasound machine, the ultrasonic characteristics are important. The characteristics can be expressed in speed of sound and ultrasonic attenuation. It is assumed that similar TMM ultrasonic properties compared to human tissue ultrasonic properties will provide similar image feedback by the machine. For the needle, the interaction parameters are important, to simulate similar response. It is assumed that similar TMM interaction properties compared to human tissue properties will provide similar response by the needle and environment. In Muller et al. [75], the elastic muscle intercostal muscle is observed to be 10 times higher than healthy liver tissue, 100 kPa versus 10kPa, respectively.

4.4. Prototyping

In this section the prototyping process is described. Furthermore, iteration steps are enlightened.

4.4.1. Design for manufacturability

Design for manufacturability is designing products in such a way that they are easy to manufacture. In general preference goes out to readily existing parts, so that the amount of custom made parts is kept at a minimum.

Actuation The actuator is chosen based upon stroke and power specifications and two wishes. From the study into the respiratory motion in chapter 3, maximum found respiratory motion is 33 mm (combined 3D translation). The stroke should therefore be at least 33 mm and preferably be more to increase functionality. More respiratory patterns can be simulated if the amplitude can be larger, yet dimensions of the actuation subsystem should be kept at a minimal (e.g. the larger the stroke, the larger the actuation subsystem). Minimal dimensions are a wish. The motor should at least be able to generate a load equal to the transdiaphragmatic pressure, which is more than 0.121 N cm^{-2}. Another wish is that the actuation generates as little sound as possible. Therefore, based on stroke, load, minimal dimensions and sound characteristics, the actuation subsystem is chosen. The actuation will be provided by a Festo EMMS-ST-28-L-SE, with integrated incremental encoder for position tracking and translated to linear motion by a ball screw slide, Festo EGSL-BS-35-50-8P. Connecting parts to the functional structure can be found in appendix F.

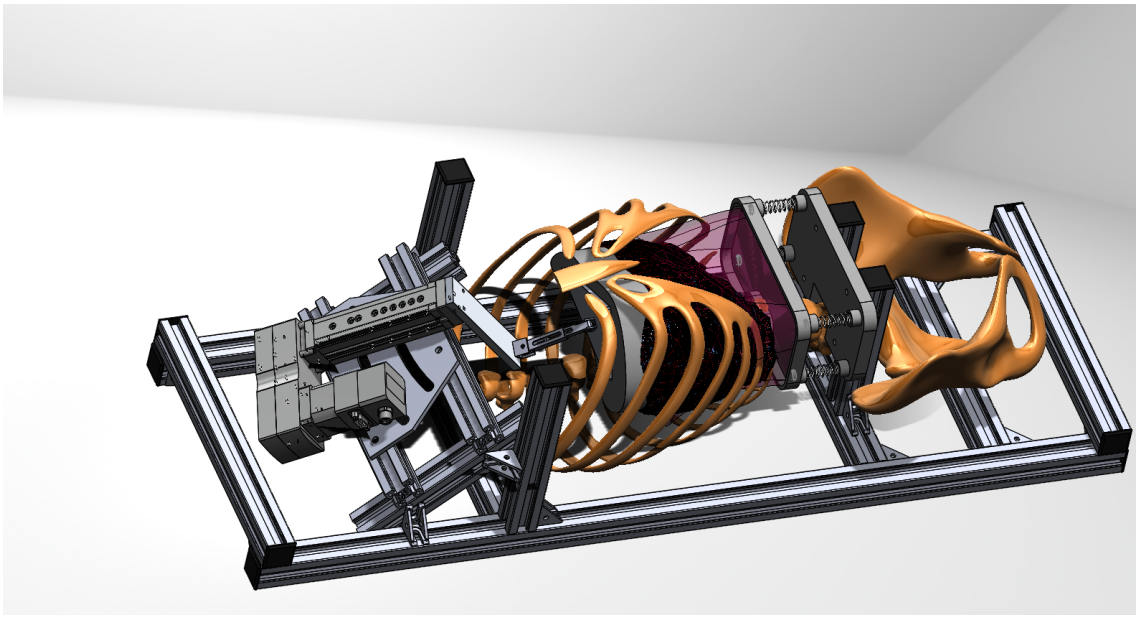

Figure 4.7: Detailed CAD in Solidworks. The subparts; actuation, functional structure, support structure and surroundings simulation, are visible for insight in the working principle.

Functional structure The functional structure is the part which will simulate the desired needle-tissue interaction and US image characteristics. The functional structure is required to be anthropomorphically shaped. The anthropomorphic shape is obtain by pour-molded the PVA solution in a 3D printed mold, as shown in figure 4.8. The mold is obtained from CT data. The CT data is segmented in MeVisLab which converts voxels to 3D point coordinates. The point coordinates can be imported and shaped in Solidworks to create a 3D liver model. The mold is created from a negative imprint of the 3D liver model. The 3D mold is created by 3D printing.com (Amsterdam, The Netherlands).

Figure 4.8: Pour-molding of the liver in 3D printed mold.

Mass percentage functional structure The functional liver structure is based upon the findings of de Jong et al. [5]. Desired property of the liver model is that it resembles cirrhotic tissue.

The needle force characteristics of PVA which resembles healthy liver tissue, is described in de Jong et al. [5]. Pathological liver tissue is stiffer and more heterogeneous [2] than healthy liver tissue, therefore the concentration is increased from 4% to 6% m PVA 2 FT and further the FT cycle is increased to 40 and 20 hours, respectively. With the increased concentration and freeze time, more cross-links can be made. The amount of cross-links depict the stiffness of the PVA model. FT time is increased because, during the liver model construction, the model did not solidify within the prior set 16 freeze and 8 thaw hours FT cycle. The production process is further described in appendices C and E.

Surroundings simulation For the surrounding tissues in the abdominal cavity also PVA is used.

Abdomen filler is constructed with 4 %m PVA and 3 freeze-thaw cycles. The abdomen filler is assumed to be stiff enough to generate sufficient support. Therefore, it is chosen to increase freeze thaw cycles, thereby increasing cross-linking and thus, the stiffness. Intercostal spaces are filled with 6%m, 3FT PVA slices to simulate muscle tissue. Mass percentages are calculated in appendix C and are based upon the friction slopes of the findings in de Jong et al. [5] and the fact that muscle tissue is stiffer than abdominal tissue.

In order to facilitate ultrasound propagation between the different layers, the samples are kept in water. Upon assembly, the water provides a promoting connection for US wave propagation. Further,

to facilitate intercostal imaging, an ultrasound patch is constructed. The patch is made from Acros PVA 6%m 2 FT. The patch is placed between the ribcage and liver model to secure a connection for ultrasound propagation.

Initial concept of the surroundings simulation was with a spring mechanism as shown in figure 4.9. However, the spring mechanism showed problems in terms of hysteresis and buckling, therefore it is replaced for a solid PVA insert. In figure 4.10, the final CAD design is shown, also the one part PVA surroundings is shown.

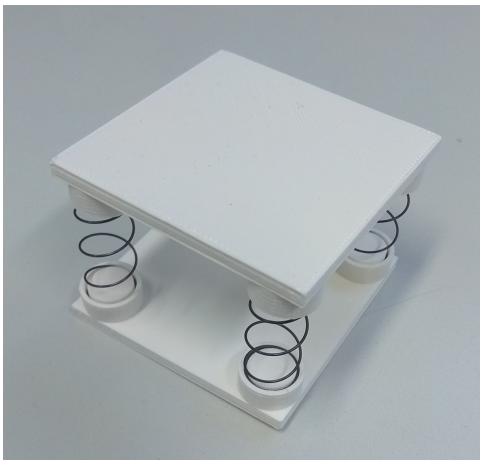

Figure 4.9: Spring mechanism for surroundings simulation.

Structural support The structural support is the subsystem which gives support to the the other subsystems. In the detailed design this can be seen as the skeleton which encapsulates the liver and surroundings structure together with the aluminum profiles to form the base frame of the design. The skeleton (Praxisdienst, Germany) is modified to minimize size which still fits the functional requirements; support and containment of the liver and surroundings model. The aluminum base frame is designed to a minimum amount of parts, while still allow to tune distances between components. The aluminum profiles along with connection components are obtained from Spanpartner BV (Ridderkerk, The Netherlands).

4.5. Final Design

During the design process, several concepts have been generated. Sequentially, the solutions which fitted the design criteria best, have been selected and further developed into an embedded design after which several iterations are made to come to a final design, as shown in figure 4.10. The assembly of the prototype is presented in the chapter 5, along with the key components.

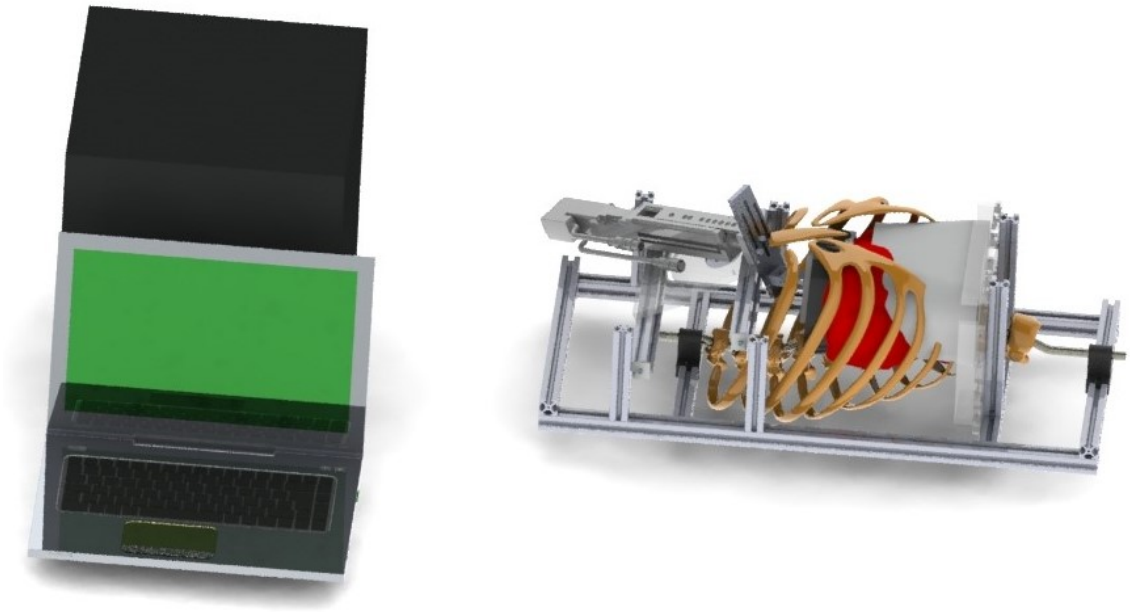

Figure 4.10: Render of the final design with laptop to show relative size and blackbox containing the control hardware.

5 Prototype

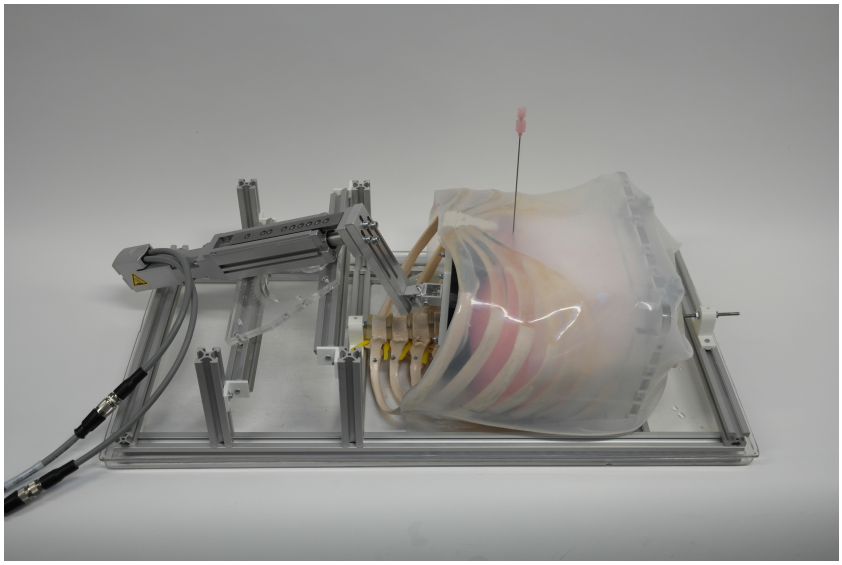

Figure 5.1: The prototype.

In this chapter, the prototype is presented. In the design process multiple iterations are made for manufacturability and compromises had to be made. The overall design is based upon the anatomical structure of the human body. Figure 5.1 shows the fully assembled prototype. The design is explained through the four subsystems presented in the previous chapter.

5.1. Design characteristics

The prototype is created based on subsolutions of four subsystems, being: functional structure, structural support, actuation and surroundings simulation. In this section each subsolution is presented and the interaction between each subsystem is elaborated on. In figure 5.2, the four subsystems are shown and encircled. The design specifications are summarized after the design evaluation in chapter 6.

Functional structure The functional structure or liver model is made of PVA hydrogel (Selvol PVOH 165, Sekisui Chemical Group NJ, USA) and manufactured by pour molding in a 3D additive manufactured mold. The mold is created from a negative imprint of a segmented liver. The imprint is aqcuired from CT data analysed in MevisLab (MeVis Medical Solutions AG, Germany) and designed to a solid structure in SolidWorks (Dassault Systèmes SOLIDWORKS Corp., Waltham, Massachusetts, USA). The segmentation is done with a 1 mm resolution in crano-caudal spacial orientation. The functional structure is designed to fit mechanical characteristics of a cirrhotic liver. The functional structure is in direct contact with the actuation and the surrounding simulation. Motion is enforced by a rigid connection between the functional structure and the actuation subsystem.

Structural support The structural support is created from a cut-out of the human thorax and spinal cord. This part is attained from adjusting the human skeleton offered by Praxisdienst (Longuich, Germany). The sternum is cut away between the connection of the cartilage of the 5th and 6th rib. Ribs 1-5 and adjoining vertebrae are removed from the model. Furthermore, the pelvis is removed and replaced by a vertical structure to hold the surroundings simulation structure. Additionally, the steelbar which reinforces the spinal cord is cut to size and rethreaded for fixation. All parts are fixated on standardized 20x20 aluminum profiles (M-BLOCAN, RK Rose+Krieger, Spanpartner BV, Ridderkerk, The Netherlands).

Actuation The actuation is provided by a stepper motor, Festo EMMS-ST-28-L-SE, with integrated incremental encoder for position tracking and translated to linear motion by a ball screw slide, Festo EGSL-BS-35-50-8P. The linear stage is mounted on an adjustable fixation plate which allows tuning of the motion vector in 2 rotation (x and y-axis) and 1 translation (x-axis) degrees of freedom. The fixation plate is made from transparant plexiglass (2mm) and cut to shape by laser cutting. In the connection to the functional structure an additional three adjustable degrees of freedom to compensate for rotations and translations induced on the effective endpoint, where the functional structure is in contact with the actuation. The adjustable rotations and translations can be fixated in a desired position, leaving only a primary translation which is controlled by the linear stage. The linear stage enforces a linear motion vector on the functional structure with preset direction.

Surroundings simulation The surroundings simulation subsystem is also created from PVA hydrogel. The surroundings simulation or abdominal structure is approached by the thought that is should sufficiently contain the liver whilst allowing enough deformation for the functional structure to move. The abdominal structure is created by pour-molding. The mold is created in a 150x250x150 mm plastic box with an additive manufactured insert. The insert is a part of the CAD segmented liver which is used for the functional structure. The insert is manufactured in an Ultimaker 2+ extended (Ultimaker B.V., Geldermalsen, The Netherlands). The liver model is position locked by shape fixation. The liver model is enclosed by the negative cut out in the abdominal structure and on the other side, the surface contact in the actuation subsystem. Additionally, the top layer of the prototype is made to recreate skin like mechanical properties, while still allow ultrasound wave propagation. The skin is made from a 2.5 mm thick layer silicone (Ecoflex 00-30, Smooth-on Inc., Macungie,Texas, USA), where width and length are 620 mm and 310 mm, respectively. The skin remains in place by friction and is easily removable.

5.2. Compromises and limitations

During the design process, it is chosen to recreate the functional structure based on the liver of only one person. This choice is made because there is no general format of a liver as in terms of shape. Each person has a differently shaped liver and therefore also a different motion vector. The motion of the chosen patient showed most median motion compared to other patients. The choice for the replication of one liver could have consequences in how the liver will eventually move in the design.

The phantom is limited for needle insertion only with a frontal or side approach in supine position with the back touching solid ground, and not for insertions from the back or a supine positioned interventions with the flange touching solid ground. Rotation of the whole model could facilitate needle insertions approaching from the the back and model positioning with the flange touching solid ground, however it is not investigated if the motion of the liver is comparable to reality nor if all parts will stay in place.

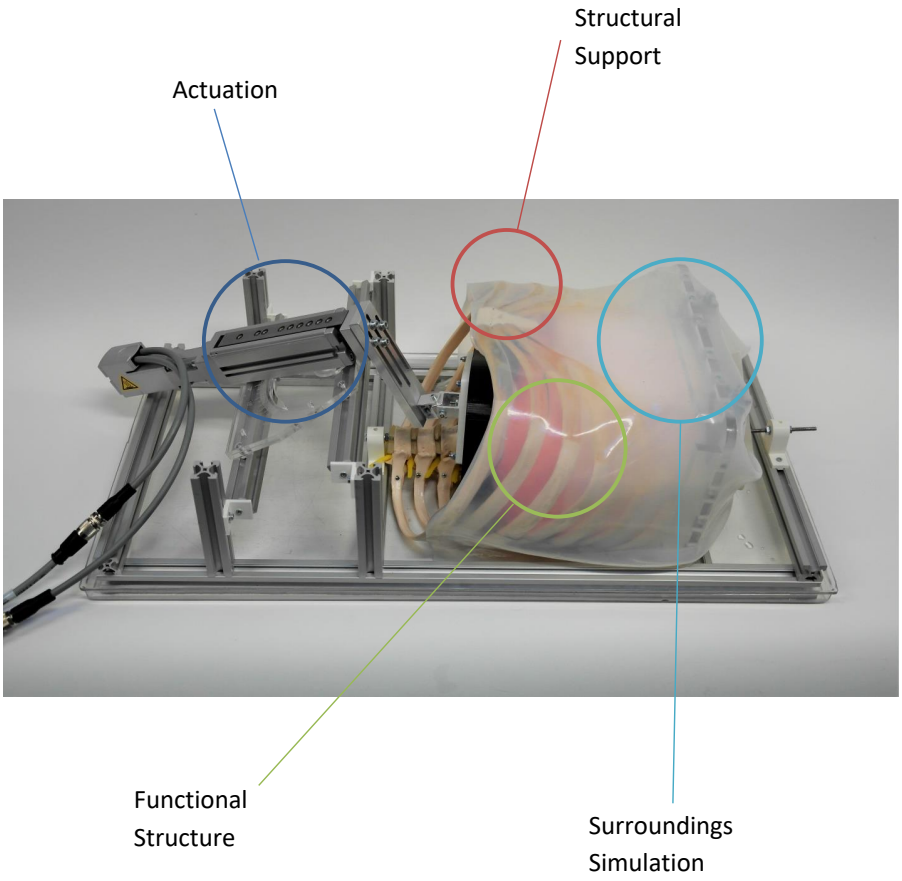

Figure 5.2: The prototype, encircled are the four primary subsolutions: functional structure, structural support, actuation and surroundings simulation.

6
Results - design evaluation

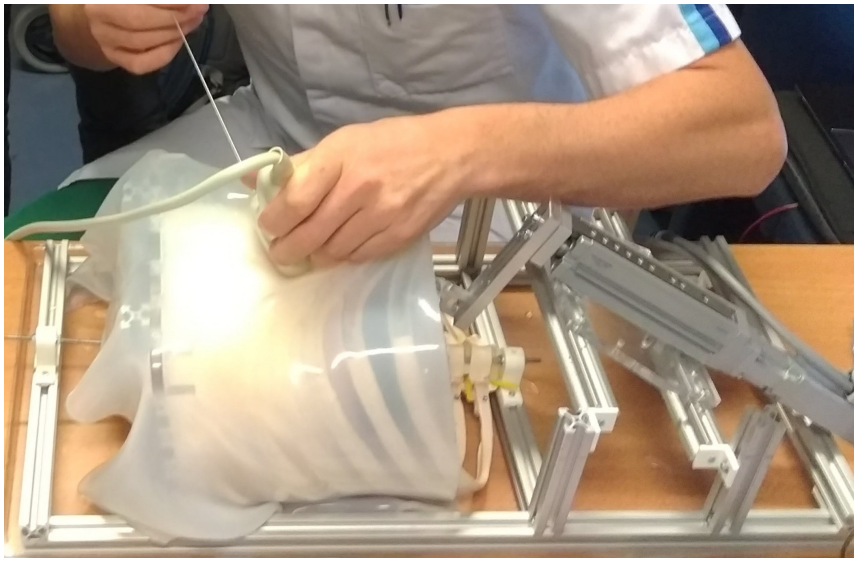

Figure 6.1: Evaluation of the phantom during needle insertion under ultrasound guidance.

In this chapter, the validation methods and results of the prototype are presented. The liver model motion pattern is characterized and the axial needle forces during insertion and retraction are measured. Needle deflection during respiratory motion is mapped and the dimensions of the liver model are obtained. Additionally, the phantom is subjected to ultrasound imaging and finally, expert feedback on the phantom is reported.

6.1. Evaluation methods

In order to validate the design against the set criteria, experiments are performed. The validation methods used in the experiments are described in the following section. Presented validation criteria are: anthropomorphic kinematics; anthropomorphic liver dimensions; anthropomorphic mechanical properties; needle deflection and expert feedback. Preliminary study showed that the liver model had too little freedom to move in the lower regions; therefore an additional PVA insert was developed. The insert could improve the kinematics. The insert has been tested as well. In table 6.1 an overview is given of the measurements, together with the goal of the measurement, configurations and amount of runs. In the table dynamic test conditions are expressed in repetitions per minute (rpm).

Table 6.1: Overview of measurements, goal of the measurement, configurations and amount of runs.

Measurement	**Goal**	**Configuration**	**Runs [#]**
Kinematics [mm]	chart respiratory motion	With insert 12 rpm	5
		Without insert 12 rpm	5
		Without insert 18 rpm	5
Dimensions [dm^3]	determine liver shape	Liver model	10
Axial needle force [N]	characterize needle-tissue interaction	Selvol 165	21
		Acros 146-186	30
Needle deflection [mm]	characterize needle-tissue interaction	IC MC 12 rpm	5
		IC MC static	5
		IC MA 12 rpm	5
		IC MA static	5
		SC MP 12 rpm	5
		SC MP static	5
US compatibility	prove US needle guidance	Subcostal	-
		Intercostal	-

6.1.1. Anthropomorphic kinematics

The liver model kinematics are charted with an electromagnetic tracking system named Aurora (Northern Digital Inc., Waterloo, Ontario, Canada). The Aurora allows to track given points from connected sensors. Reasons to do the tracking electromagnetically is because first, the PVA samples are not transparent, excluding direct video tracking methods. Second, ultrasound imaging requires difficult automated tracking. Third, other imaging methods, e.g. MRI, CT, are time consuming and not readily available, thus are excluded on availability and time span.

Six sensors (Aurora 5DOF 0.8 mm x 11 mm) are placed on different locations in the phantom. Prior to positioning the sensors, they are made waterproof by adhesive coating (Kombi Power Bison, Bolton Adhesives, Rotterdam, The Netherlands). The sensors are placed on the phantom as shown in figure 6.2. In frontal view, two sensors in the global maxima in transverse direction (sensor 1 & 3), one at the caudal maximum (sensor 4) and in sagittal perspective one at the anterior maximum(sensor 2), are placed. Another sensor is positioned on the bone to cartilage transition of the 7^{th} rib (sensor 5). The last sensor is put on the 'liver press' (sensor 6), which is the direct contact of the liver with the motion stage and works as reference signal for the motion vector tracking.

The phantom is actuated with a configuration of 12 rpm and 18 rpm. The used motion pattern is that of patient 4 as presented in chapter 3. The motion vector is [22.3 17.0 5.3] mm in [CC AP LR] direction. Each configuration is repeated for 5 runs. Each run is recorded for 60 seconds, starting at the maximum expiration state. Records are sampled with 40 Hz. The run sequence is randomized. Randomization is done to reduce the effect of possible changes in the environment. The translation of the sensor is compared to the translation acquired from the CT segmented data from patient 4 at the projected location of the sensors.

For comparison between the different configurations, a sensor selection is made. The selection is as follows:

- For studying the difference between measured data and CT data, sensor 2 and 4 are chosen.
- For studying the effect of a different breathing cycle period, sensor 2 is chosen.
- For studying the effect of an additional insert sensor 4 in chosen. At the location of sensor 4, most difference should be notable. Only 12 rpm is presented.
- For increasing validity of the motion vector, sensor 6 is observed.

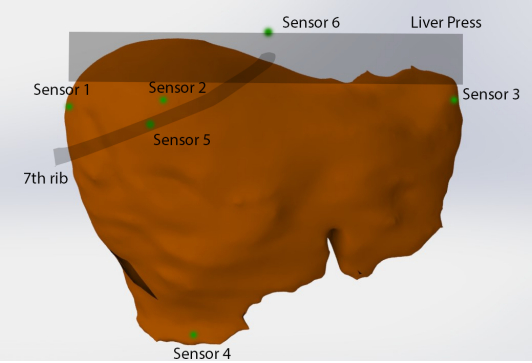

Figure 6.2: Frontal view on the liver model depicting the locations of the applied sensors.

The field generator is placed in parasagittal plane of the phantom. For the Aurora, the minimal distance between a sensor and the field generator should be 5 cm. Furthermore, the sensor accuracy decreases the further it is moved away from the field generator. Therefore, the phantom model and field generator are fixated with a 5 cm gap in between at the narrowest point. Also, the Aurora receiver and motor control unit are placed as far away as possible, so interference by noise is kept minimal. The experimental setup is shown in figure 6.4.

Data acquisition is done by 'NDI Track' software (Northern Digital Inc., Waterloo, Ontario, Canada) running on a laptop. Data-analysis is done in Matlab 2017a (MathWorks, Inc., Natick, USA). An example of a 3D tracked path is shown in figure 6.3. Amplitude is determined as difference between maxima in CC, AP and LR direction. To reduce noise a low-pass butterworth filter is used. Cut-off frequency is 50 Hz at 1000 Hz sample rate.

6.1.2. Anthropomorphic liver dimensions

The dimensions of the liver are determined by direct measurement with measuring tape. This allows for a global estimation of the size in three dimensions. The liver model is placed with the anterior side facing up on a flat surface. The maxima in CC, AP and LR direction are manually measured.

Another measured metric is the gross weight of the liver model. The liver model is placed on a scale (Kern PCB 6000-1, Balingen,Germany) and the weight is reported.

The last metric is volume. The liver model volume is obtained by the water displacement method, which rests on the concept that a submerged object displaces a volume of liquid equal to the volume of the object. The liver is placed in a full bath of water and the overflow of liquid is caught in an overflow container. The experimental setup is shown in figure 6.5. Sequentially, the overflow is measured on a scale (Kern PCB 6000-1, Balingen,Germany) and converted to volume by the known density properties of water at a given temperature. The experiment is performed at room temperature, measured at 20.7 $^{\circ}C$ with a digital thermometer (Technoline ws 7012, Wildau, Germany). The volume measurement is repeated 10 times.

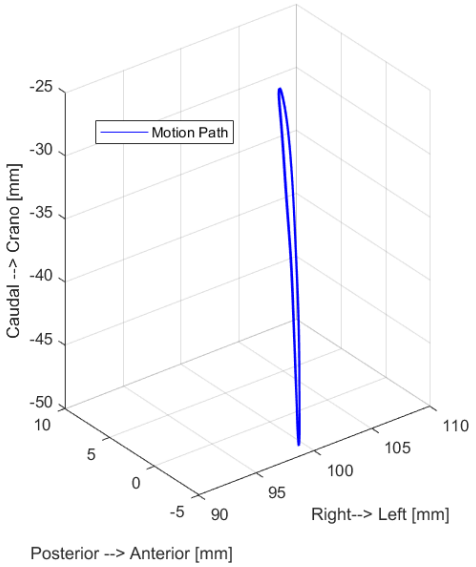

Figure 6.3: Example motion 3D path.

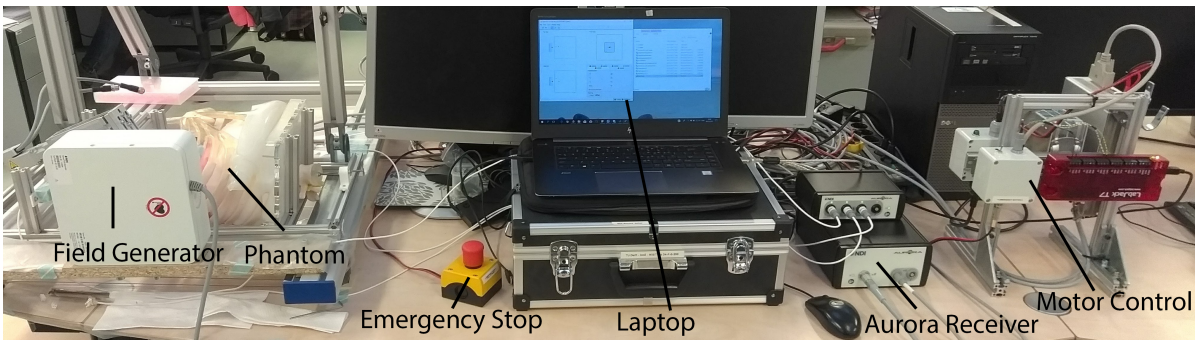

Figure 6.4: Experimental setup for the kinematics registration of the liver model.

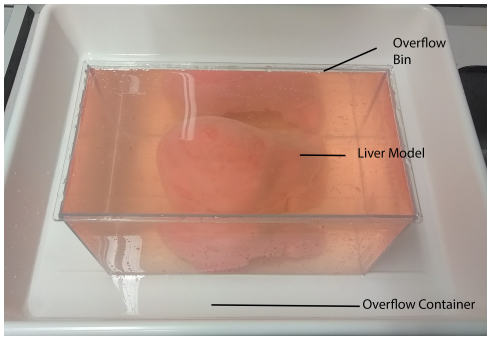

Figure 6.5: Experimental setup for the volume registration of the liver model.

6.1.3. Anthropomorphic mechanical properties

The mechanical properties of the liver model can be characterized by three metrics: the needle friction slope [N/mm], amplitude of peak forces [N] and amount of peak forces per decimeter [#/dm]. The acquirement and processing of the metrics are described in the following section.

The inner needle of an 18 Gauge Disposable Two-Part Trocar Needle (Cook Medical, Bloomington, USA), is mounted on a linear motion stage (EGSL-BS-45, Festo Group, Esslingen, Germany) and connected via a load sensor (LSB200 5lb, Futek, Irvine, California). The experimental setup is shown in figure 6.6. Only the inner needle is used in order to eliminate force effects of the outer cannula and to allow comparison to the human liver measurements done in the needle insertion experiments of de Jong et al. [5]. The measurements of the human liver are done on a healthy ex-vivo liver and the data is publicly available [76]. Sequentially, the needle insertion depth is at least 50 mm in the sample at a constant insertion and retraction speed of 5 mm/s. Data acquisition stores the axial forces acting on the needle hub, as well as corresponding time and positions at a sample frequency of 1KHz.

The measurements are done on two separate samples and not on the liver model itself; this is done to spare the model for the needle deflection experiment. The liver model is created from a 6%m 2FT PVA, Selvol PVOH 165 (Sekisui Chemical Group NJ, USA), solution. Therefore, two physically cross-linked samples are made of 6%m PVA, one sample Selvol PVOH 165 (Sekisui Chemical Group NJ, USA) and one Acros PVOH 146-186 (Acros Organics, Geel, Belgium), following the same preparation method. Both samples are subjected to 2 freeze-thaw (FT) cycles, with a freeze and thaw cycle of 40 and 20 hours, respectively. Preparation method is repeated as follows: the granular PVA is mixed at room temperature, then heated to 93 °C and maintained at that temperature for 30 minutes. The solution is then passively cooled to room temperature. Sequentially, the samples are placed in the freezer to commence the freeze-thaw cycle, freezing at -30 °C and thawing at room temperature. Amount of needle insertions is determined by the surface area. Each needle insertion is performed with at least 10 mm distance from any other needle track. The amount of needle insertions in Selvol 165 and Acros 146-186 are 21 and 30, respectively.

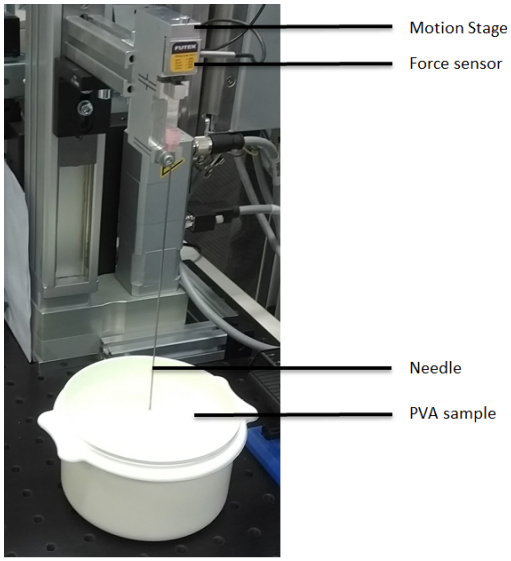

Figure 6.6: Experimental setup for the mechanical properties registration of Selvol and Acros PVA samples.

Needle friction slope Data-analysis is done in Matlab 2017a (MathWorks, Inc., Natick, USA). For the determination of the friction slope, a region of interest (ROI) in the retraction phase is selected. The ROI is chosen such that retraction start-up dynamics are diminished and no effects of deceleration are notable. The slope of a linear best estimate on the ROI is regarded as the needle friction slope. In figure 6.7, an example of the determination of the friction slope with a selected ROI is shown.

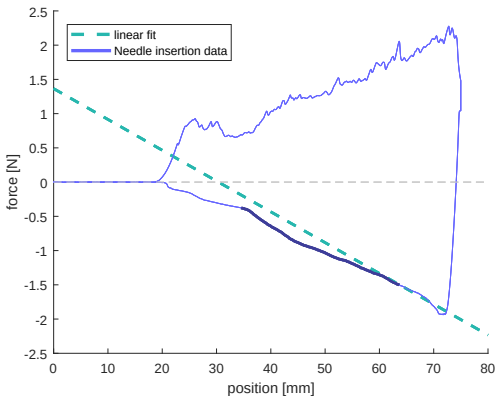

Figure 6.7: Example determination friction slope, with emphasized ROI. Adopted *from* Pluymen, 2016.

Needle peak forces - amplitude and amount To characterize needle peak force amplitude and amount, the acquired data is filtered by the Douglas-Peucker algorithm (DPA) for a top-down data reduction and separation of relevant from irrelevant peaks. The DPA is adopted from van Gerwen et al. [30]. For the data set, a divergence criterion of 0.05N is used. The divergence threshold removes relatively small peaks, yet preserves the characteristics of the needle forces. In figure 6.8, an example of the peak reduction is shown. Further, peak height is defined as the change in needle force between the maximum and the previous minimum after subtraction of the needle friction slope. The subtraction is done to correct the signal, thus to prevent overestimation of the peak height. In figure 6.9, an example is shown of the extraction of the peak force height and peak force amount.

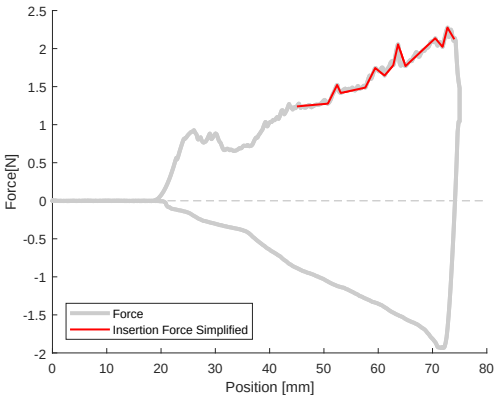

Figure 6.8: Example of peak reduction by the DPA given as Insertion Force Simplified. Adopted *from* Pluymen, 2016.

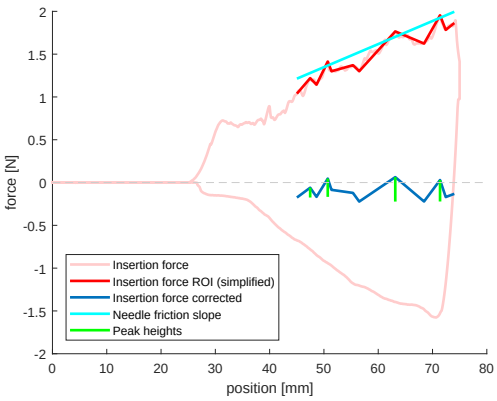

Figure 6.9: Example determination peak force height and amount. Adopted *from* Pluymen, 2016.

6.1.4. Needle deflection

The needle deflection is charted with the same electromagnetic tracking system as used for the mapping of the liver model kinematics, Aurora. Electromagnetic tracking is chosen, since PVA limits direct video tracking due to nontransparent material property.

A redesign of the liver model and surroundings has been considered by incorporating gelatin models instead of PVA. However gelatin is not suitable, since it cannot withstand shear needle forces. Consequentially, the needle tears through the gelatin model during respiratory motion instead of deflecting in a liable way, which in turn leads to unreliable measurements.

The needle deflection is characterized for six configurations. The needle is manually inserted in three different locations for two different conditions. In each location, the needle is inserted with the phantom in static condition and another time in dynamic condition, moving at 12 rpm. Each configuration consists of 5 runs. Each run is recorded in 60 seconds. Records are sampled with 40 Hz. Combining the static and dynamic condition per location, there are 10 runs. The run sequence is randomized per insertion location. The insertion locations and angles are as follows:
1) Subcostal midplane, perpendicular to coronal plane. 2) Intercostal midaxillary, perpendicular to sagittal plane. 3) Intercostal midclavicular, 45° from coronal plane and 45° from transverse plane (insertion towards posterior, crano and left quadrant).

The insertion parameters are set as follows: Insertion depth is 70 mm from the skin, insertion speed is manually controlled at around 10-20 mm s^{-1} and during a dynamic run, the needle is inserted at the exhalation maximum. The needle is released, once it has reached the insertion depth.

The needle deflection is determined from the measurement of three sensors. Two sensors (Aurora, 5DOF 0.8 mm x 11 mm) are placed on a hub to which the needle is fixated. The third sensor is integrated in the needle (Aurora Needle, 2-Part, 18G/150 mm, Chiba). The three sensors are aligned. The sensor placement and part of the experimental setup is shown in figure 6.10. Other components of the experimental setup are the same as shown in figure 6.4.

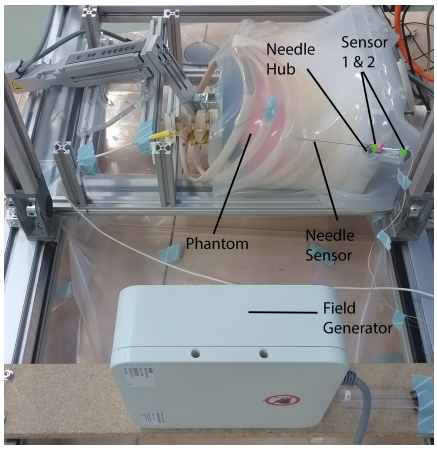

Figure 6.10: Experimental setup for the needle deflection registration in the phantom.

Data-analysis is performed in Matlab 2017a. Continuing, the two sensors on the hub are assumed to be at a fixated position relative to each other. The hub is considered a rigid object, showing no deformation during the experiment. With this assumption, the two hub sensors are used as reference to estimate the needle deflection. The two hub sensors are virtually connected to form a line. This line is translated, so it intersects with the needle sensor before insertion. The initial translation of this line is the offset, which is corrected for prior to insertion. The deviation from the corrected line is regarded as the absolute needle deflection during insertion. In figure 6.11, the initial sensor positions, the correction and the needle deflection is shown as step 1,2 and 3, respectively.

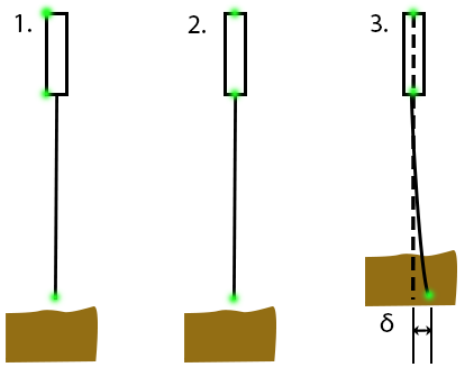

Figure 6.11: Data analyses for determination of the needle deflection. Step 1, initial sensor positions (green); step 2, correction by placing hubsensors intersecting the needle sensor; step 3, deflection determination.

To allow comparison between the dynamic and static runs, the average needle deflection is estimated. The mean between the maximum and minimum deflection between 15 to 30 seconds in a run is used for the estimation. Between 15 to 30 seconds, needle deflection is assumed to be in steady-state.

6.1.5. Ultrasound imaging properties

In order to verify the possibility for ultrasound needle guidance, the phantom is subjected to visual ultrasound image reconstruction. The ultrasound machine (Philips HD7 XE, Eindhoven, The Netherlands) is used to verify the US image modality. Images from both a subcostal as well as an intercostal window are obtained.

6.1.6. Expert feedback

A liver surgeon and interventional radiologist are asked to provide feedback on the prototype. Topics for the feedback are presented in this section.

Liver Surgeon Overall feedback of the 6%m 2 FT (40/20) liver model is obtained from a site visit to the Erasmus Medical Center. From an interview with dr. W. Polak, specialized in liver transplantation, feedback on tactile feeling and aesthetics is obtained. As a reference the 4%m 2FT PVA 70% scaled liver model of Tom Paardekoper is used. Furthermore, an in-house Fibroscan (Echosens 2017, Paris, France) is used for Vibration-Controlled Transient Elastography (VCTE) determining the elastic modulus of the liver model. The Fibroscan working principle is elastography. It propagates sound waves 80 mm into the tissue and estimates the elastic modulus based on response of tissue positioned at 20 to 60 mm depth.

Interventional radiologist Overall feedback on the performance of the prototype is obtained from an assessment by dr. A. Moelker. The assessment is done on the respiratory motion, ultrasound imaging reconstruction, needle response, dimensions and overall performance. The doctor is asked to fill in a form as shown in appendix K. The prototype is configured with 12 rpm, 28,5 mm stroke in motion vector [CC AP LR] = [22.3 17.0 5.3], or plane rotations: x-y 17.3° ; y-z 37.3°.

6.2. Evaluation results

In this section, the performance of the design is presented in means of results of the validation methods. Most of the results are expressed in a boxplot, with a median and interquartile range (IQR).

6.2.1. Anthropomorphic kinematics

The motion of the tracking points from different configurations are shown in figure 6.12 to 6.15. In figure 6.12, the translation of sensor 2 subjected to 12 breathing cycles per minute is shown. Sensor 2 is closest to the contact between the liver model and the actuation part. The median motion in this sensor, is 20.73 (IQR 20.56-20.94), 10.81 (IQR 10.74-10.90), 6.68 (IQR 6.63-6.73) mm in CC, AP and LR direction, respectively as oppossed to the motion of the real liver which is 25.14, 13.25, 10.06 mm in CC, AP and LR direction, respectively. The translation of the sensor is in the same direction as in the CT scan, yet smaller in all directions.

Sensor 4 is furthest away from the actuation part. Displacement by motion is shown in figure 6.13. The median motion in this sensor, is 4.76 (IQR 4.61-4.89), 1.46 (IQR 1.41-1.53), 0.81 (IQR 0.80-0.81) mm in CC, AP and LR direction, respectively as oppossed to the motion distilled from the CT scan at the projected location of sensor 2, 21.00, 21.6, 22.00 mm in CC, AP and LR direction, respectively. The translation of the sensor is in the same direction as in the CT scan, yet smaller in all directions.

The effect of a different breathing cycle period is measured. In figure 6.14, the displacement for breathing cycle period between 12 rpm and 18 rpm is shown. The median motion for 12 rpm, is 20.73 (IQR 20.56-20.94), 10.81 (IQR 10.74-10.90), 6.68 (IQR 6.63-6.73) mm in CC, AP and LR direction, respectively. The median motion for 18 rpm, is 19.53 (IQR 19.40-19.73), 10.12 (IQR 10.08-10.24), 6.38 (IQR 6.35-6.42) mm in CC, AP and LR direction, respectively.

The measured motion vector is presented in appendix J. The reference signal is shown for both 12 rpm and 18 rpm for the runs with and without insert. From the reference signal in a configuration without insert at 12 rpm, the median motion vector is 24.06, 9.83 and 7.13 mm in CC, AP and LR direction, respectively. For 18 rpm without insert, the motion vector is 22.94, 9.31, 6,75 mm in CC, AP and LR direction, respectively.

The effect of an additional insert in the surroundings simulation is measured. In figure 6.15, the displacement with and without insert at 12 rpm of sensor 4 is shown. The median motion with no insert, is 4.76 (IQR 4.61-4.89), 1.46 (IQR 1.41-1.53), 0.81 (IQR 0.80-0.81) mm in CC, AP and LR direction, respectively. The median motion with, is 6.85 (IQR 6.65-7.14), 1.32 (IQR 1.24-1.38), 0.73 (IQR 0.64-0.83) mm in CC, AP and LR direction, respectively.

The motion of the tracking points of all runs in each configuration can be found in appendix G.

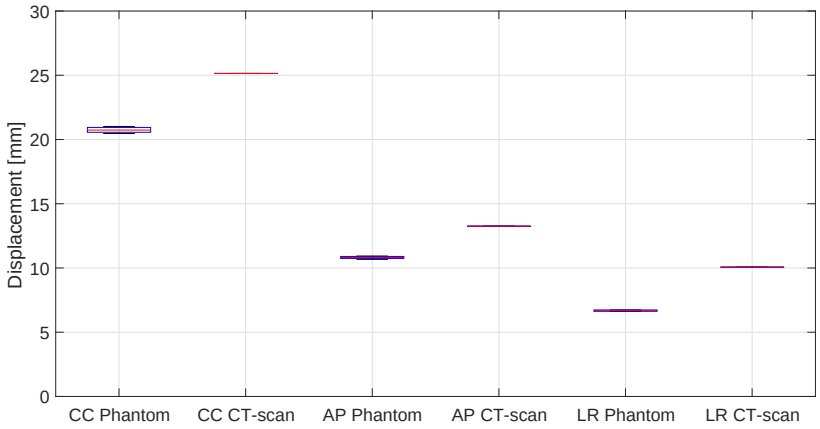

Figure 6.12: The liver model translation versus the CT derived translation in CC, AP and LR direction subjected to 12 breathing cycles per minute in sensor 2. CT derived data has no range since it is obtained from 1 sample point.

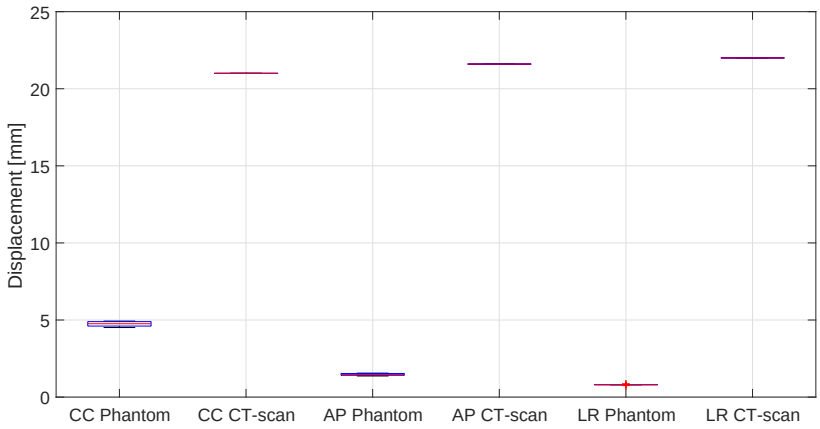

Figure 6.13: The liver model translation versus the CT derived translation in CC, AP and LR direction subjected to 12 breathing cycles per minute in sensor 4. CT derived data has no range since it is obtained from 1 sample point.

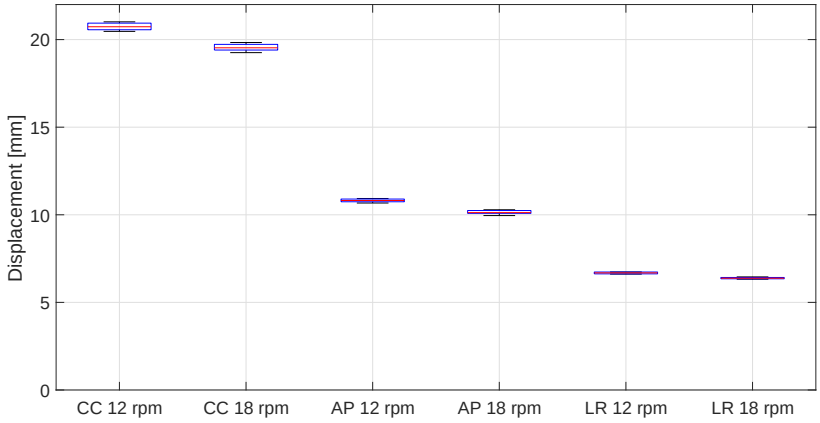

Figure 6.14: Influence of different breathing cycles on the motion pattern measured in sensor 2.

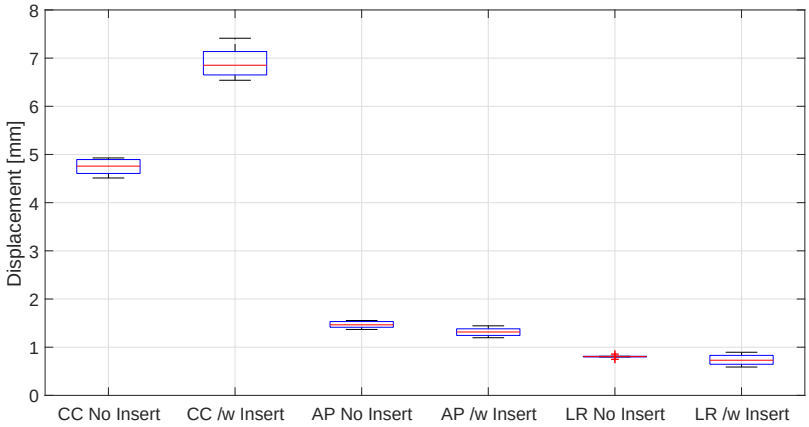

Figure 6.15: Influence of an additional insert on the motion pattern measured in sensor 4.

6.2.2. Anthropomorphic liver dimensions

The measured dimensions of the replicated liver model are 169, 104 and 224 mm in CC, AP and LR direction, respectively. For perspective, in figure 6.16, the relative size is shown. The volume of the liver is measured as 1.188($\pm$0.023) dm^3 and weighs 1308 grams, resulting in a density of 1108 kg/m^3.

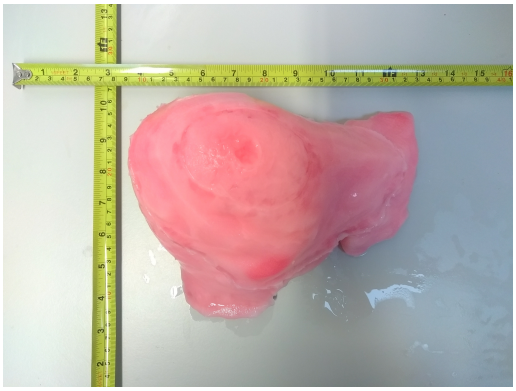

Figure 6.16: The relative size of the functional structure which simulates the liver constructed with 6%m PVA 2 FT cycles.

6.2.3. Anthropomorphic mechanical properties

The mechanical properties of 6%m PVA are characterized in needle friction, needle peak force-amplitude and -amount of peaks. The results of the three metrics are presented in this section. All runs are shown in appendix H.

Needle friction slope The PVA samples show different needle friction slopes then observed in healthy liver tissue. The median needle friction force is 0.0374 (IQR 0.0339-0.0406), 0.0076 (IQR 0.0068-0.0081) and 0.0111 (IQR 0.0098-0.0134) N/mm for 6%m 2 FT (40/20h) PVA Selvol, 6%m PVA 2 FT (40/20h) Acros and healthy liver tissue, respectively. These results are visualize in a boxplot as shown in figure 6.17.

Needle peak forces - amplitude and amount The amplitude and amount of needle peak forces are observed to be as follows. The median height of peak needle forces is 0.185 (IQR 0.116-0.249), 0.030 (IQR 0.018-0.043), 0.179 (IQR 0.095-0.335) N for 6%m 2 FT (40/20h) PVA Selvol, 6%m PVA 2 FT (40/20h) Acros and healthy liver tissue, respectively. These results are summarized in a boxplot as shown in figure 6.18.

The median amount of peaks per decimeter is 17.25 (IQR 13.80-17.25), 18.97 (IQR 17.25-24.15), 7.27 (IQR 5.45-9.08) #/dm for 6%m PVA 2 FT (40/20h) Selvol, 6%m 2 FT (40/20h) PVA Acros and healthy liver tissue, respectively. These results are summarized in a boxplot as shown in figure 6.19.

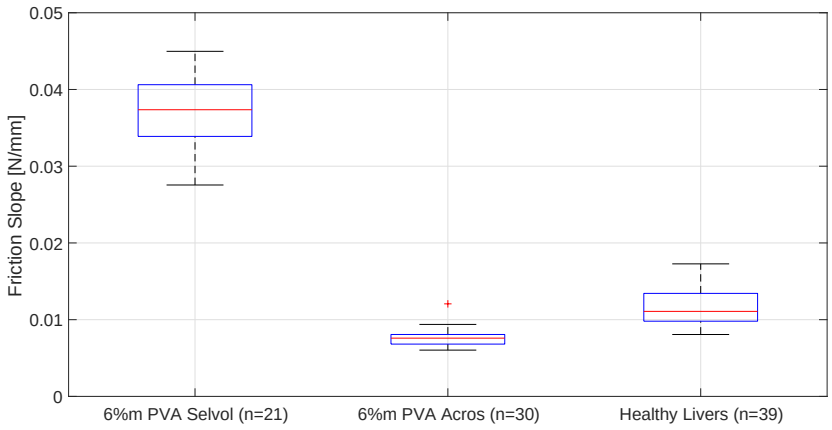

Figure 6.17: The friction slope [N/mm] of 6%m PVA 2 FT (40/20h) cycles from brands: Selvol and Acros, respectively versus healthy liver tissue.

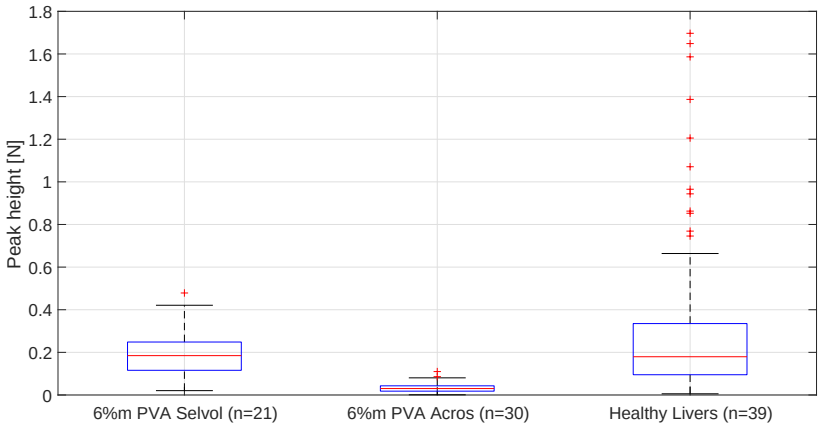

Figure 6.18: The height of peak needle forces [N] of 6%m PVA 2 FT (40/20h) cycles from brands: Selvol and Acros, respectively versus healthy liver tissue.

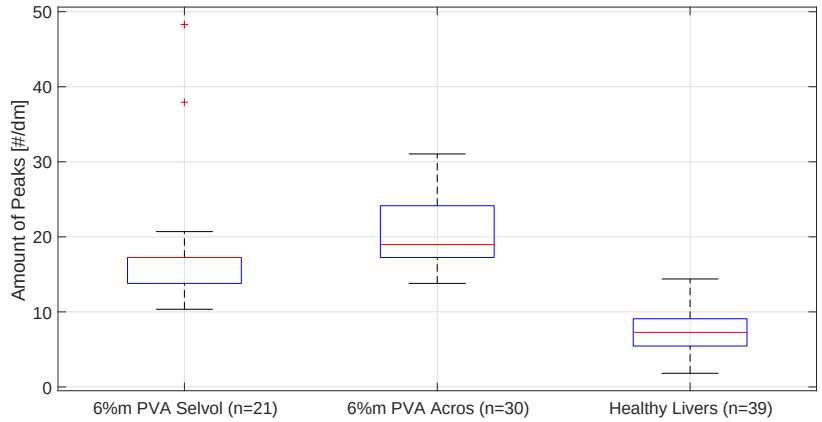

Figure 6.19: The amount of peak needle forces [#/dm] of 6%m PVA 2 FT (40/20h) cycles from brands: Selvol and Acros, respectively versus healthy liver tissue.

6.2.4. Needle deflection

Needle deflection is evaluated in static and dynamic insertion configurations. In figure 6.20, the amount of needle deflection is shown for three static and three dynamic configurations. All runs are presented in appendix I. Median needle deflection for intercostal mid-axial static insertion is 12.12 mm (IQR 12.01-12.90 mm), where the median needle deflection for intercostal mid-axial static insertion is 11.20 mm (IQR 10.49-11.57 mm). Median needle deflection for intercostal midclavicular static insertion is 11.08 mm (IQR 10.57-11.75 mm), where the median needle deflection for intercostal midclavicular static insertion is 8.27 mm (IQR 7.39-12.00 mm). Median needle deflection for subcostal midplane static insertion is 3.72 mm (IQR 3.49-4.13 mm), where the median needle deflection for subcostal midplane static insertion is 3.48mm (IQR 3.24-5.38 mm).

The median, IQR and spread in IQR are summarized in table 6.2. The spread in IQR is reported to show the relative variance between runs in each configuration.

6.2.5. Ultrasound imaging compatibility

In this part the results of the ultrasound imaging compatibility of the phantom is presented. Image reconstruction is possible. In figure 6.21, an ultrasound visual reconstruction from a subcostal positioned probe is shown. The sound waves propagate through three layers. The first skin layer of 3mm silicone, then a second abdominal surroundings layer of 4%m 3FT PVA, followed by the liver model 6%m 2FT PVA. The prototype also contains an intercostal US imaging window between the 6^{th} and 7^{th} rib. US reconstruction during intercostal probing is shown in figure 6.22.

Table 6.2: Overview of the median, IQR and spread in IQR of needle deflection

Configuration	Static IC MA	Dynamic IC MA	Static IC MC	Dynamic IC MC	Static SB MP	Dynamic SB MP
Median [mm]	12.12	11.20	11.08	8.27	3.72	3.48
IQR [mm]	12.01-12.90	10.49-11.57	10.52-11.75	7.39-12.00	3.49-4.13	3.24-5.38
Spread IQR [mm]	0.89	1.08	1.23	4.61	0.64	2..14

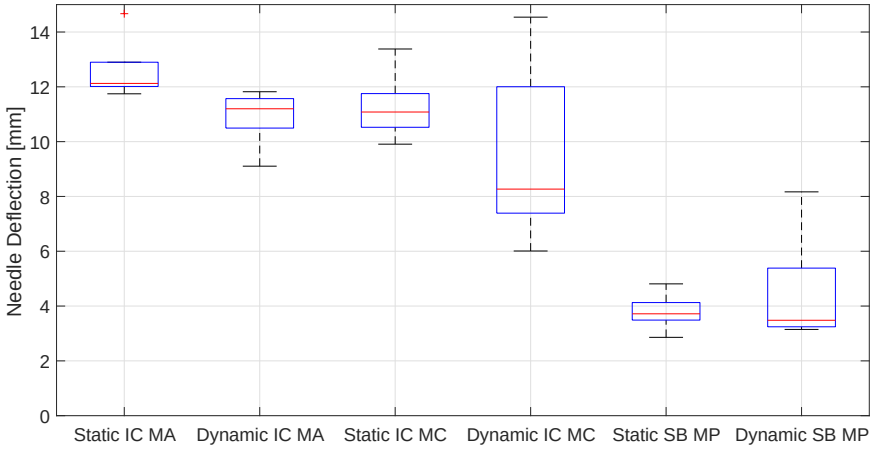

Figure 6.20: Amount of needle deflection for 6 different insertion configurations. IC MA = Intercostal Mid-Axial; IC MC = Intercostal Midclavicular; SB MP = Subcostal Midplane.

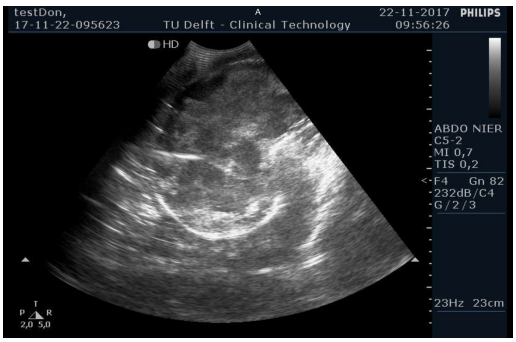

Figure 6.21: Ultrasound image reconstruction of the integrated liver model taken from subcostal probe position.

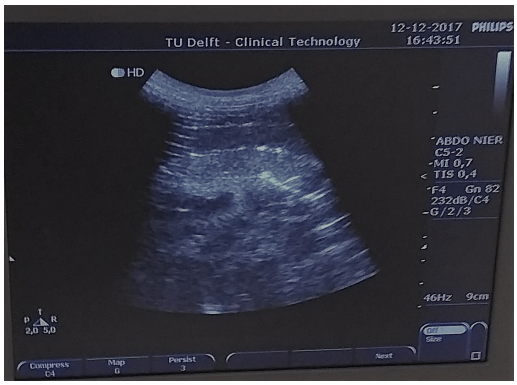

Figure 6.22: Ultrasound image reconstruction of the integrated liver model taken from intercostal probe position.

6.2.6. Expert feedback

In this section, expert feedback is presented from a liver surgeon on the liver model and from an interventional radiologist on the full prototype. The feedback consists of comments, reactions and assessment from the doctors.

Liver surgeon The first response of dr. Polak was that: 'this liver model is more realistic than the small model'. The scaled 4%m PVA liver model is described as 'too elastic' and 'not representative for a diseased liver'. Further, the pathology of the 6%m PVA model is estimated on a liver fibrosis grade 2 based on tactile experience.

As a note, the 6%m PVA liver model is labeled as 'springy', a characteristic which the doctor had not seen in real tissue. In terms of weight and size, dr. Polak. described the full-scale model as 'light' and still 'relatively small'. The shape was characterized as 'good' and 'realistic'. From an aesthetic point of view, the doctor asked if the model could be more brownish, instead of the current color pink. An overview of comments by dr. W. Polak is given in table 6.3.

Table 6.3: Overview of the comments about the liver model by dr. W. Polak.

Aspect	Description
Shape	Good, relatively small
Weight	Relatively light
Stiffness	Fibrosis grade 2, springy
Color	Not brown

Second, an examination on the Fibroscan is performed on the 6%m PVA liver model. The E-modulus has been measured at 24.0 (IQR ±8.2) kPa. All measurements are reported in table 6.4. The 6%m PVA liver model had to be partially submerged in a water container to make the Fibroscan to work. The 4%m PVA scaled liver model was too small for the Fibroscan to work; therefore no data was obtained from the scaled liver model.

Table 6.4: Overview of the elastography requirements on the fibroscan.

Measurement	Elastic Modulus [kPa]
1	16.4
2	27.7
3	14.0
4	22.5
5	32.4
6	27.2
7	24.5
8	23.4
9	18.0
10	27.7
Median (IQR)	24.0 (8.2)

Interventional radiologist dr. Moelker was enthusiastic about the phantom and also saw room for improvements. The overall performance of the phantom is graded 3.5 out of 5. Ultrasound-guided needle insertion was described as 'good' and was 'clearly visable' on the ultrasound machine. However, the ultrasound texture of the liver phantom was described as too 'inhomogeneous'. The liver tissue itself shows a lot of difference in ultrasound texture between patients, but not in the same liver. Further, the needle was traceable both subcostal as intercostal. The filled in phantom assessment form can be found in appendix K. In figure 6.23, an interventionist is shown conducting ultrasound-guided needle insertion on the prototype. During the assessment, the needle tracks of previous inserted needles remain visible on the ultrasound image.

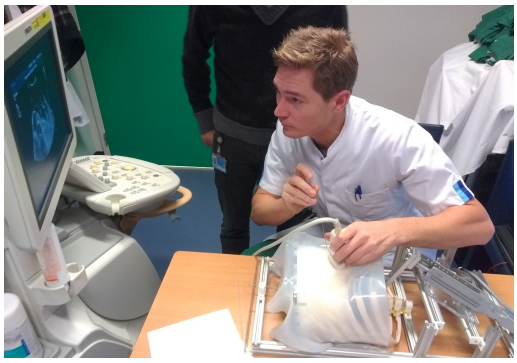

Figure 6.23: Clinical testing of the prototype in the Erasmus MC for ultrasound-guided needle insertion.

6.3. Summary Design Specifications

The prototype underwent several experiments to validate the design criteria. The design criteria are summarized in table 6.5. For the kinematics, the median of sensor 2 with the configuration under 12 rpm with no additional insert, is taken as representation for the design specification.

Needle deflection is not described in the design specifications, since it was not a design criterion. However, needle deflection will be discussed in the discussion.

Table 6.5: Overview of the design specifications versus design requirements

Design criteria	Specification	Requirement
Anthropomorphic liver kinematics	CC direction: 0-20.7 mm	0-31 mm
	AP direction: 0-10.8 mm	0-21 mm
	LR direction: 0-6.7 mm	0-15 mm
Adjustability	Adjustable motion pattern	Able to adjust motion pattern
Anthropomorphic mechanical properties	Friction slope: 0.0374 N/mm	0.015-0.05 N/mm
	Amplitude peak forces: 0.185 N	0.1-0.8 N
	Amount of peak forces: 17.24#/dm	>8 #/dm
Anthropomorphic liver dimensions	CC direction: 169 mm	147.4-181.1 mm
	AP direction: 104 mm	126.7-198.5 mm
	LR direction: 224 mm	183.3-221.4 mm
Anthropomorphic liver volume	1.118 (±0.023) dm^3	0.94-2.344 dm^3
Compatible with ultrasound imaging	Ultrasound needle guidance possible sub- and intercostal	Ultrasound needle guidance possible

7 Discussion

Figure 7.1: Workshop part construction.

In this chapter the interpretation of the results is presented and the limitations of the study are discussed. Also, recommendations for future work are given.

7.1. Interpretation of results

In this section the results are interpreted and discussed. Topics are anthropomorphic kinematics, anthropomorphic dimensions, anthropomorphic mechanical properties, needle deflection, ultrasound imaging compatibility and expert feedback.

7.1.1. Anthropomorphic kinematics

The liver kinematics differ for each sensor location. Sensor 4 shows that the upper part of the liver model follows the motion vector as noted on the patient specific CT scan. The simulated motions are smaller in CC, AP and LR direction, but are in the same direction as observed in the CT scan. The stroke can be adjusted to fit the motion as seen on the CT scan. A different solution could be to redesign the enclosement of the liver model, so the model is more free to move.

Further, based on the results it can be said that the caudal section of the liver model moves too little compared to motion on the CT scan. The motions measured by sensor 4, positioned low on the liver, are relatively small and deviate most from observed motion in the CT compared to sensor 2. As mentioned before, a redesign of the enclosement of the liver model can be done to allow more motion freedom.

Furthermore, considering differences in the dynamic conditions 12 and 18 rpm. The model moves less for 18 rpm than with 12 rpm. The decrease in motion can be subscribed to the control of the actuation. Since, the period of a stroke is shorter, the time for the control loop to follow the given sinosoid decreases as well. The outer values of the sinosoid are therefore chopped, which results in a relative smaller amplitude. The decrease is also noted in the reference signal as shown in appendix J. A solution can be the tuning of the control loop based on a given rpm, in this case the gain in the feedback loop can be increased. Additionally, the measured reference signal shows that the desired motion vector of 22.3, 17.0 and 5.3 mm in respectively CC, AP and LR direction, is not achieved. The measured reference signal of 24.06, 9.83 and 7.13 mm in respectively CC, AP and LR direction, deviates most in AP direction. The difference points out that the tuning of the motion vector in AP direction is difficult.

Continuing, an additional insert is introduced to improve motion simulation in the lower parts of the liver model. The insert increased the motion in dominantly CC direction, as noted in sensor 4, from median 4.8 mm to median 6.9 mm. However, although the insert increases the motion in the lower parts, the observed motion with insert is still not in the same order as observed on the CT scan.

The difference in motion between the top and bottom sensor show that there is compression, which leads to tissue deformation. The tissue deformation is not taken into account in the prototype, but can be valuable for further development. In reality, the liver deforms as well. For the functionality of the phantom itself, the compression has influence on the motion, however the liver model and other PVA construction parts do not show signs of plastic deformation of rupture.

7.1.2. Anthropomorphic dimensions

The shape and dimensions are obtained from a real patient; therefore the liver dimensions can be said to be anthropomorphic. The 3D model used for pour-molding is 173, 119 and 225 mm in AP, CC and LR direction, respectively. If the 3D model is compared to the measured outcome of liver model of 169, 104 and 224 mm in AP, CC and LR direction, respectively, a main decrease in AP direction can be found. During the measurements, the liver model tends to flatten under gravitational force. Sequentially, the dimensions in LR and CC directions increase, where as the size in AP direction decreases. Additionally, the liver has a natural curvature if reviewed in transverse plane. Hence, laying the liver phantom with anatomical coronal plane parallel to the surface, the curvature diminishes, which results in a increase in LR length. Further, the 3D model is obtained from a CT scan in which the liver is supported by the abdominal surroundings. In short, differences can be subscribed to the varying effect of gravity and support.

Volumetric measurements showed that the liver is within the range of 1 standard deviation from the volume of a healthy sized liver. Thereby, meeting the set design requirement.

7.1.3. Anthropomorphic mechanical properties

The friction slope, peak force amplitude and amount of peak forces are investigated and interpreted in this part.

Needle friction slope The PVA samples differ from each other in amount of friction exerted on the shaft measured during retraction. Selvol 6%m PVA 2FT shows a higher median friction slope than seen in Acros 6%m PVA 2FT. Selvol 6%m PVA 2FT also shows a higher median friction slope compared to healthy liver tissue. Acros 6%m PVA 2FT shows a lower median friction slope in comparison with healthy liver tissue.

The reason for the difference between Selvol PVA and Acros PVA can be subscribed to a different amount of hydrolysis between the two PVA types.

Selvol 165, is super-hydrolyzed to 99.3+%, whereas Acros 146-186 is hydrolyzed to 98.0-98.8%. Further, the amount of volatiles is batch dependent. Thus, a different batch might need different mass concentrations for the same result.

Selvol 6%m PVA 2FT is designed to be at least stiffer than healthy liver tissue. The increased stiffness is confirmed by the higher friction slope, since the friction slope is characterized by the internal stiffness of a material.

Needle peak forces - amplitude and amount The median amplitude of peak forces for Selvol 6%m PVA 2FT, 0.182 N, is in the same order as healthy liver tissue, 0.179 N. The IQR of Selvol 165 6%m PVA is within the IQR of healthy liver tissue. The median amount of peak forces for Selvol 6%m PVA 2FT is higher than for healthy liver tissue.

The median amplitude and IQR of peak forces for Acros 6%m PVA 2 FT are lower and outside the IQR of healthy liver tissue.

Further, Acros 6%m PVA 2FT has near equal peak height in cutting forces and shows a higher amount of peaks per dm than observed in healthy liver tissue. Acros 6%m PVA 2FT is deemed more heterogeinic compared to Selvol 6%m PVA 2FT, since the amount of peak forces is higher. However, Acros 6%m PVA 2FT is easier to cut through and shows too little friction; therefore Acros 6%m PVA 2FT is deemed less suitable than Selvol 6%m PVA 2FT for simulation of cirrhotic liver tissue.

7.1.4. Needle deflection

The needle deflection IQR spread increases with the dynamic interference of respiratory motion. This is shown by a larger interquartile range for all three test locations: intercostal mid-axial, intercostal midclavicular and subcostal midplane.

The median needle deflection is lowest for the subcostal configurations. This can be subscribed to the gravitational forces acting on the hub during the IC MC and IC MA needle insertion configurations. The gravitational forces increase the needle deflection. The hub holds the sensors used for the determination of the needle deflection.

The highest median needle deflection is observed for the static intercostal mid-axial insertion configuration. This configuration is, due to the orientation, most susceptible for gravity compared to the other two locations. However, the difference in median between the static and dynamic configuration is difficult to explain, other than the interference of the respiratory motion of the liver that reduces the median needle deflection in the current measurement method.

The order of needle deflection in the static subcostal insertion, 3.7 mm, is comparable to the values found in literature. The needle deflection found in Roesthuis et al. [77] is around 6 mm over 70 mm insertion at 10 mm/s with bevel tip needles. Though the authors used a gelatin model, with a different elasticity, needle friction forces are close to the PVA liver model used in this work and have near equal tissue properties. Further, needle and insertion parameters are also similar. The used method for obtaining needle deflection can be deemed appropriate for configurations where gravity has minimal effect. in this case in the subcostal midplane configuration where gravity mostly works co-linear to the needle.

7.1.5. Ultrasound imaging compatibility

The ultrasound machine produces a visual reconstruction of the prototype. On the reconstruction, clear hyper-echogenic edges of the liver model are visible. The contour of the liver can be seen. Further, the US waves can propagate through multiple layers of TMM. This feature allows a multi-layered design, while still allowing for US-guided needle insertion.

7.1.6. Expert feedback

Expert feedback connects the technical work with the medical world. Dr. W. Polak and dr. A. Moelker are asked for feedback on this work. Dr. Polak said that the liver model can be categorized with a grade 2 liver fibrosis, thereby, confirming that the liver model can simulate diseased liver tissue. Further, based on the Fibroscan results of 24.0 (±8.2) kPa, the liver model can be classified as cirrhotic. As prescribed in the Fibroscan interpretation guide and described by De Ledinghen and Vergniol [78], in cirrhotic patients the liver stiffness ranges from 13 - 15 kPa to 75 kPa. The mean normal liver stiffness examined in 429 healthy subject was 5.5 (±1.6) kPa. Thus, both on results of tactile experience as of the Fibroscan, the liver model can be classified as cirrhotic.

Furthermore, based on the interview with dr. Moelker, the respiratory motion is deemed as natural. Upon needle insertion the ultrasound window changes by the motion of the liver. As consequence the inserted needle disappears from the window as it would happen in a real environment. Ultrasound texture can be improved. The doctor mentioned that the US texture is too heterogeneous. Normally, the liver shows a homogeneous US texture. There are many different US textures for a liver. The texture can appear more or less echogenic but only as a whole structure. Further, the doctor mentioned that the skin is a nice feature. The silicone skin was, according to the doctor, not too easy to penetrate, which was good. The human skin also shows resistance upon needle insertion.

7.2. Study limitations

Some limitations of the study need to be taken into account when interpreting the results. In this section the limitations of the study are discussed.

Methods:

- The recreated liver model is obtained from a different patient (patient 3) than the simulated liver motion (patient 4). In the current prototype configuration, the motion vector of patient 3 was outside the adjustable range. The different shape of the liver model can influence the responding motion path, leading to a different design specification. However, due to the direct contact between the linear stage and liver model, the motion will be in the same order and direction as in the current prototype. Further, if the shape of the liver is studied between patient 3 and 4, near equal dimensions are found, as reported in table 4.2 and visualized in appendix B. Therefore, it is reasonable to assume that the influence of the differences is marginal.
- During needle deflection measurement the needle is inserted manually. The manual handling is prone for difference in insertion angle, needle insertion velocity and synced insertion for each run.
- For most of the validation experiments, 5 runs are taken, which is minimal. A higher amount of runs per configuration can increase validity of the results and decrease the chance of an outlier interfering with the measurements.
- Only part of the liver model is registered for motion tracking. For a complete scan of the model under motion, a different registration method should be applied.
- In the comparison between CT data and liver model kinematics, no IQR is noted from the CT data, since it only consists of 1 sample. Other patient based liver models can be produced. The liver models can be used to compare the distinct CT data to the liver kinematics of that patient.
- Another limitation is that the mechanical properties are acquired on a different experimental setup. Thereby, different background noise from the setup, effects of needle blunting and lowered needle coating might affect the results. Furthermore, the experiment is executed by different people, so inter-operator differences might have an influence as well.
- Experiment configurations with enabled respiratory motion, are started manually and are therefore not equally timed.
- The Aurora tracking system used in the measurement of the liver model kinematics and needle deflection experiments is prone for interference from ferromagnetic materials in the surrounding. In the prototype aluminum profiles are used, which also interfere with the measurement accuracy of the Aurora. During preliminary study for the suitability of the Aurora, interferences up to 4 mm deviation were observed. The highest deviation was noted when a ferromagnetic object was moved directly between the field generator and the sensor. However, during the experiments, no ferromagnetic objects were in between the sensor and the field generator. In the motion measurements, static interference differs less than 1 mm. This can be observed on the figures in appendix I between 15 - 30 seconds for static configurations. Note that the signal in those figures contains the combined noise of 3 sensors.

PVA properties:

- The choice of PVA is based on findings in literature which consider 'pure' materials. Other TMMs with additives could still be better able to replicate needle-tissue interaction or ultrasound imaging properties.
- The preparation method of PVA affects the material mechanical properties. The experiments done in the evaluation are done on samples produced in a beaker, while the liver model is prepared in a mold. The mold acts as isolation, thereby affecting thaw rate and freeze time and thus, the preparation method.
- This study only includes the mechanical characterization of 6%m 2 FT (40/20h) PVA, while the outcome is highly dependent on the production method. Other outcomes are possible if a different operator conducts the same experiment, since environmental circumstances are never the same unless the production is done in a fully controlled environment.

Phantom:

- A linear motion profile is assumed whereas reality might show a more curved path.
- Only one patient specific liver model is integrated in the design and prototype. A different liver model will likely behave differently than the one used in the current prototype. Different behavior can be noted in liver motion, which

in turn changes the insertion parameters. The change in insertion parameters will affect needle force, needle deflection and tissue deformation.

- The overall assessment of the prototype has only been performed by one expert; therefore, user tests with a larger amount of physicians could be conducted to obtain even more insight in possible improvements.

7.3. Recommendations

In section recommendations for future work are given. In future work the following aspects can be explored:

PVA properties:

- In this work only a few PVA preparation methods have been used. For further research, investigation in the effects of concentration, degree of hydrolysis, addition of ions, type of solvent, freeze time and thaw rate, on both mechanical and imaging properties can be done.
- Additionally, a link between the degree of pathology and PVA preparation method could be valuable. Sequentially, a desired pathological state can be recreated in a controlled manner.

Phantom motion:

- The rib motion in the prototype is not optimal. The motion of the rib changes the ultrasound window used during needle insertion. For a better interaction between operator and phantom, the rib motion should be bigger.
- Study different motion vectors and liver model response.
- Integration of patient specific respiratory signals can improve the realistic behavior of the design. The current prototype produces solely sinusoidal respiratory motions.
- The surrounding simulation structure inhibits the motion of lower parts of the liver model more than desired. Compartimisation of the surroundings could enhance the motion in these parts.

Needle deflection:

- The needle deflection is measured in the prototype, but lacks comparison data. For the comparison to realistic deflection, a cirrhotic *ex-vivo* liver can be analyzed with similar experimental conditions.

Ultrasound image modality:

- For ultrasound image reconstruction only one intercostal window is available. For increased functionality, other windows should be created.
- Study ultrasound texture of PVA for liver sized volumes.
- Study amount of needle insertion before material is too damaged for ultrasound imaging.

General:

- In a broader perspective, the current design setup could be embedded with other organs (e.g. kidneys, stomach, spleen) and subject them to a variety of respiratory induced motion patterns, as is done with the liver in this study.

8 Conclusion

The aim of this study was to develop a liver phantom which is able to replicate liver movement and simulates similar needle-tissue interaction as human tissue in ultrasound-guided needle interventions. In current literature no phantom model is known which enables the aforementioned features. The development of such a phantom allows the assessment of new devices and pre-clinical procedures and can function as training device for physicians.

Design An anthropomorphic breathing liver phantom is designed with properties facilitating multi-direction adjustable liver motion patterns and ultrasound-guided needle insertion. Sequentially, the design has been constructed and evaluated. The current prototype allows the user to switch to a desired motion pattern, where the motion of the liver is induced by a direct drive of a linear stage. The stroke length and vector can be tuned manually to fit the desired motion pattern.

Evaluation The functionality of the design is evaluated using three criteria: motion analysis, mechanical properties and ultrasound-guiding. First motion analysis shows a motion vector of 20.7, 10.8 and 6.7 mm in CC, AP and LR direction, respectively. The reference motion of the liver is obtained from real case testing and subjected on the liver model. Second, the mechanical properties of the liver model for needle-tissue interaction are characterized as cirrhotic liver tissue. The mechanical properties of the model are assessed on axial needle force measurements and expert feedback. An increased median needle friction force (0.0374 N mm^{-1}) is observed compared to healthy liver tissue (0.0111 N mm^{-1}). Further, Fibroscan elastography shows that the median stiffness of the liver model is cirrhotic (24.0 kPa) if compared to healthy liver values (5.5 kPa). Furthermore, liver surgeon dr. W. Polak characterized the liver model as a fibrosis scale 2 liver. Finally, the prototype allows intercostal and subcostal ultrasound-guided needle insertion. The prototype has been assessed by interventional radiologist dr. A. Moelker and provided the physician with the necessary visual feedback for needle guidance.

In a broader perspective, the prototype can be used for research into the assessment of new devices. Furthermore, the prototype can be used as a training model for physicians in training. Concluding, the prototype allows realistic respiratory liver motion and needle-tissue interaction during ultrasound-guided needle intervention.

Appendices

A

Appendix A: elastic modulus of the liver, PVA, PVC

In literature elastic modulus of liver tissue, PVA and PVC is described by different sources with the use of different measurement methods. In table A.1 to A.3, an overview is given of the elastic modulus of each material from several sources.

Table A.1: Elastic modulus of healthy and liver tissue.

Structure	Elastic Modulus [kPa]	Method	Source
Healthy liver	0.64(±0.08)-2.0(±0.63)	Compression	Yeh et al. [2]
	6.61(±1.41)	Elastography	Muller et al. [75]
	5.7(±1.8)	Elastography	Wong et al. [79]
	5.94	Indentation	Lim et al. [80]
Cirrothic liver fibrosis grade 5	1.17(±0.17)-19.98(±6.95)	Compression	Yeh et al. [2]
	25.1(±17.1)	Elastography	Wong et al. [79]

Table A.2: Elastic modulus of PVA.

Structure	Elastic Modulus [kPa]	Method	Source
PVA	3.6-11.4 (FT dependent)	Tensile	Jiang et al. [81]
	2.5-5.4 (FT dependent)	Compression	Cournane et al. [82]
	1.6-16.1 (FT dependent)	Elastography	Cournane et al. [82]
	42.0-89.1 (FT dependent)	Compression	Fromageau et al. [83]

Table A.3: Elastic modulus of PVC.

Structure	Elastic Modulus [kPa]	Method	Source
PVC	18-63	Compression	DiMaio and Salcudean [31]

B

Appendix B: motion modes segmented livers

On the following pages the motion modes per patient are shown in a trimesh function of Matlab 2017a (MathWorks, Inc., Natick, USA). The mesh is shown in sagittal, transverse and coronal perspective.

Patient 1

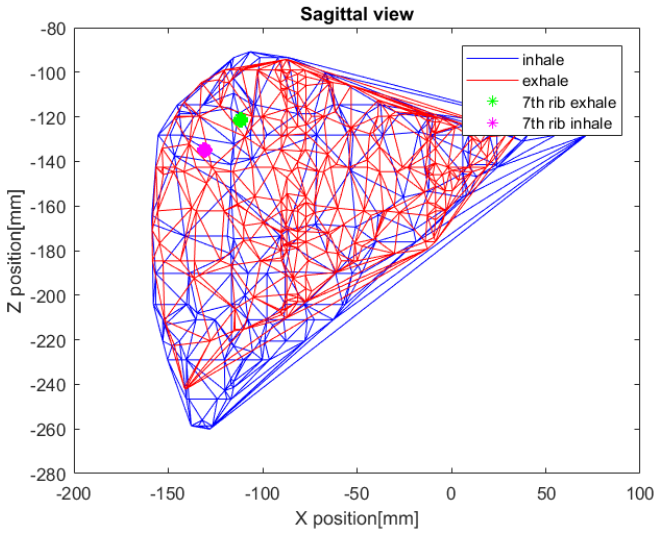
Sagittal view
inhale
exhale
7th rib exhale
7th rib inhale
Z position[mm]
X position[mm]
-80
-100
-120
-140
-160
-180
-200
-220
-240
-260
-280
-200
-150
-100
-50
0
50
100

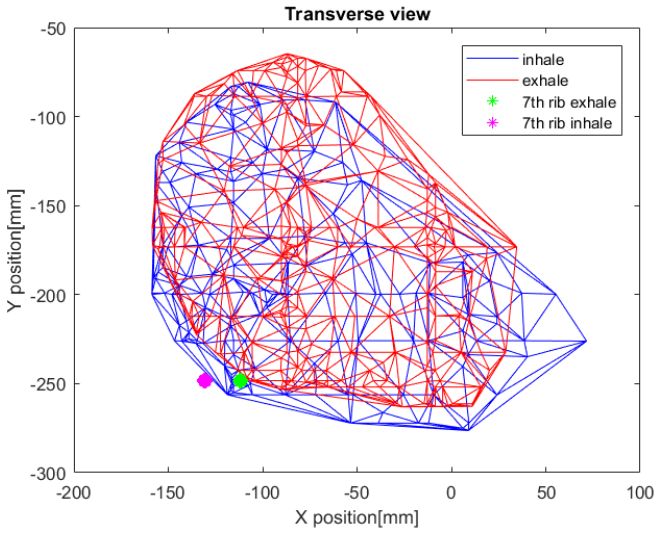
Transverse view
inhale
exhale
7th rib exhale
7th rib inhale
Y position[mm]
X position[mm]
-50
-100
-150
-200
-250
-300
-200
-150
-100
-50
0
50
100

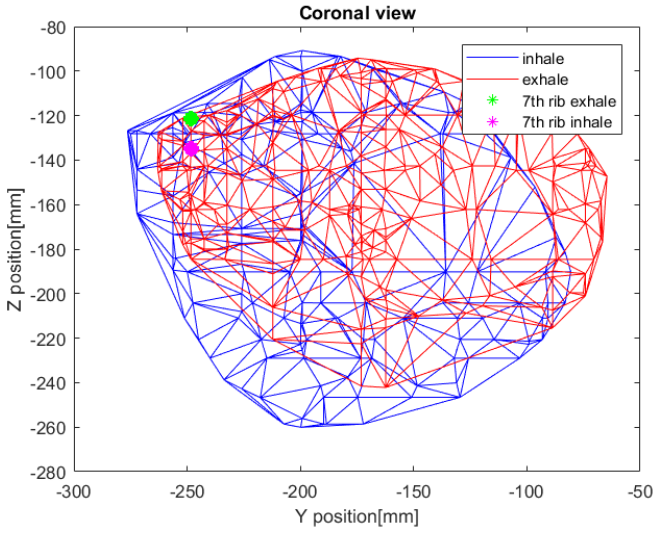
Coronal view
inhale
exhale
7th rib exhale
7th rib inhale
Z position[mm]
Y position[mm]
-80
-100
-120
-140
-160
-180
-200
-220
-240
-260
-280
-300
-250
-200
-150
-100
-50

Patient 2

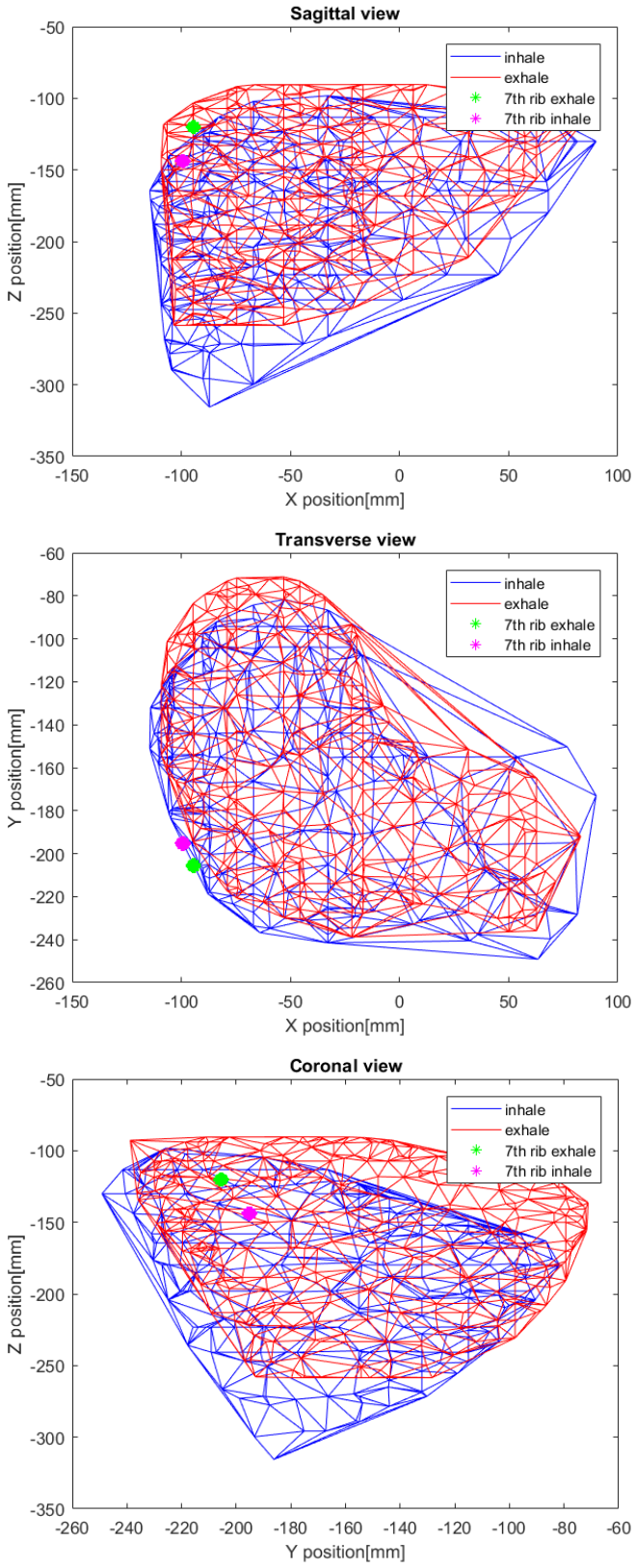
Sagittal view
inhale
exhale
7th rib exhale
7th rib inhale
Z position[mm]
X position[mm]
Transverse view
inhale
exhale
7th rib exhale
7th rib inhale
Y position[mm]
X position[mm]
Coronal view
inhale
exhale
7th rib exhale
7th rib inhale
Z position[mm]
Y position[mm]

Patient 3

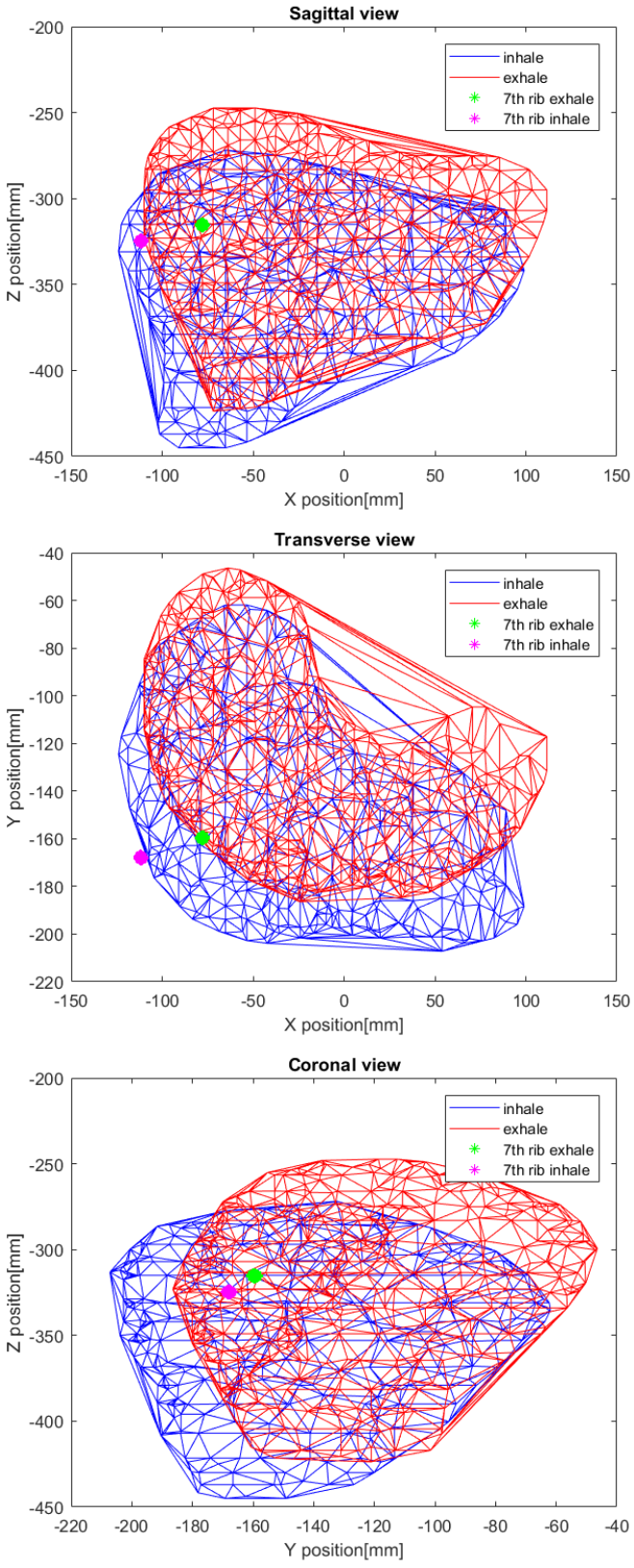
Sagittal view
inhale
exhale
7th rib exhale
7th rib inhale
Z position[mm]
X position[mm]
Transverse view
inhale
exhale
7th rib exhale
7th rib inhale
Y position[mm]
X position[mm]
Coronal view
inhale
exhale
7th rib exhale
7th rib inhale
Z position[mm]
Y position[mm]

Patient 4

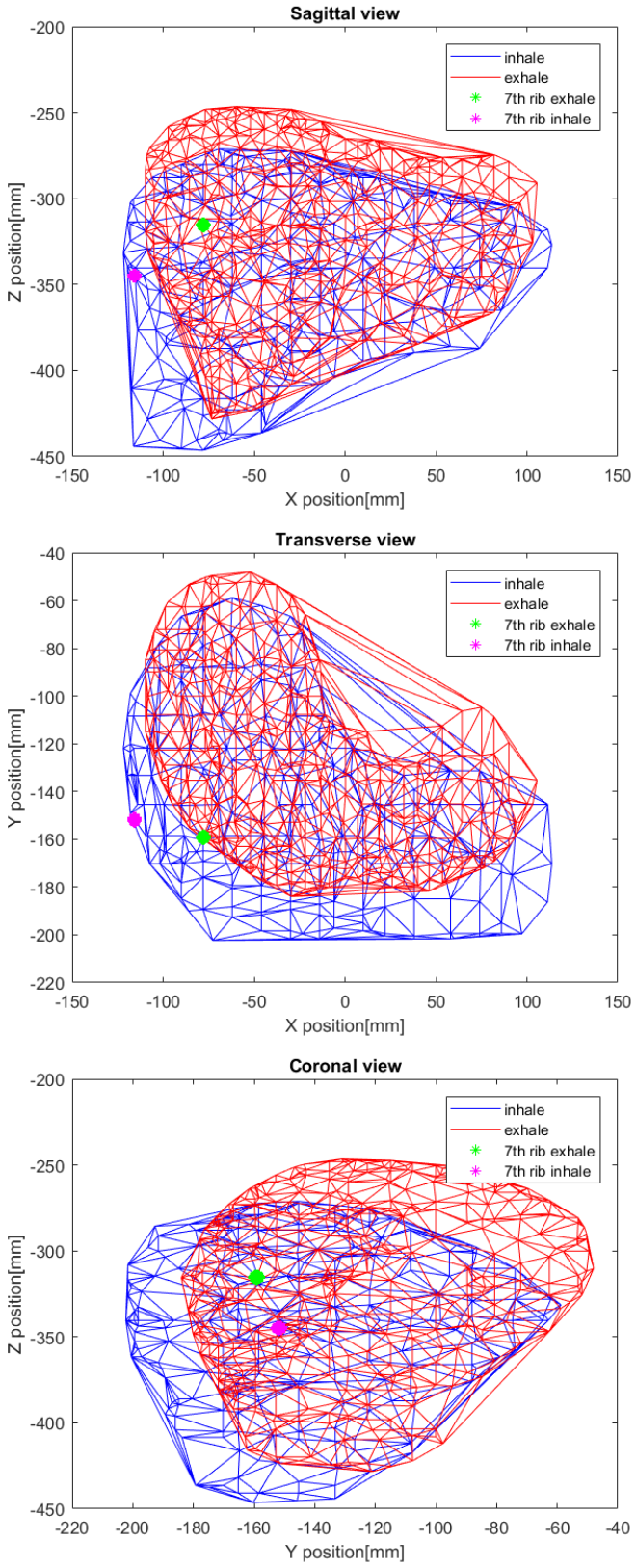
Sagittal view
inhale
exhale
7th rib exhale
7th rib inhale
Z position[mm]
X position[mm]
Transverse view
inhale
exhale
7th rib exhale
7th rib inhale
Y position[mm]
X position[mm]
Coronal view
inhale
exhale
7th rib exhale
7th rib inhale
Z position[mm]
Y position[mm]

Patient 5

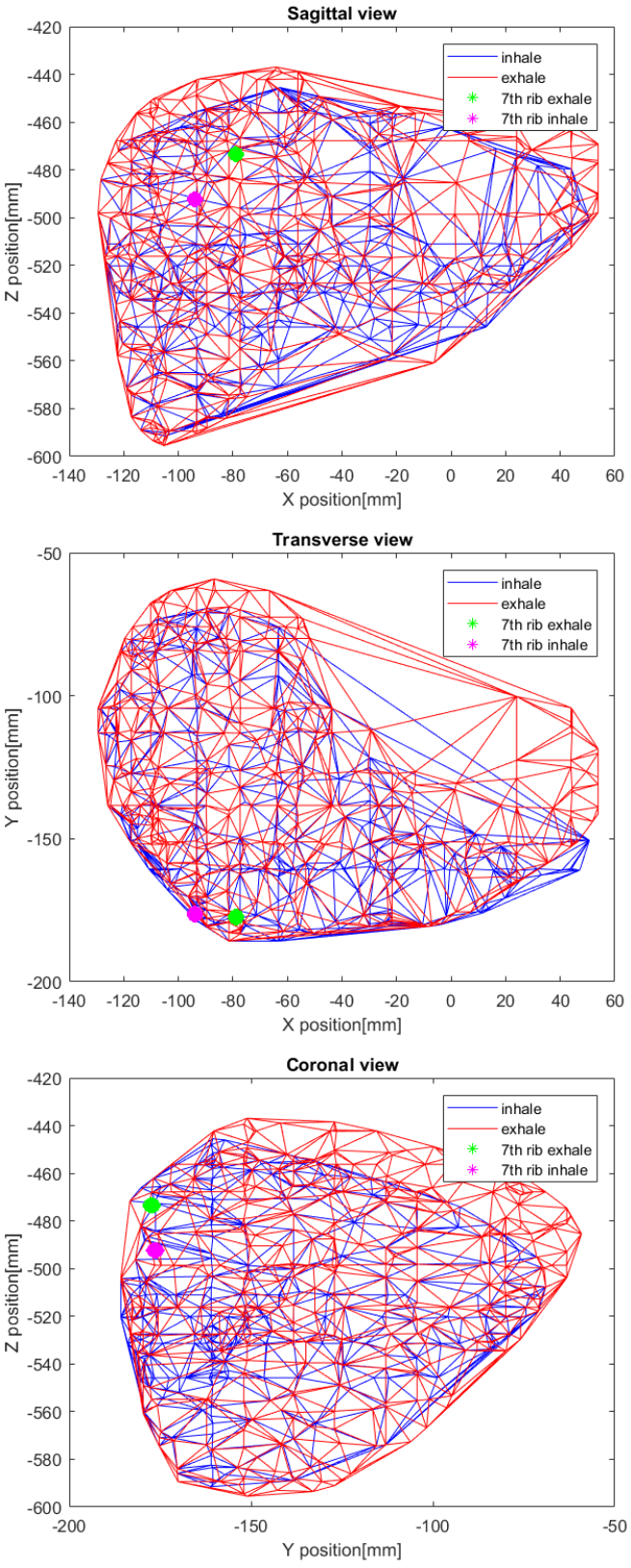
Sagittal view
inhale
exhale
7th rib exhale
7th rib inhale
Z position[mm]
X position[mm]
Transverse view
inhale
exhale
7th rib exhale
7th rib inhale
Y position[mm]
X position[mm]
Coronal view
inhale
exhale
7th rib exhale
7th rib inhale
Z position[mm]
Y position[mm]

C

Appendix C: PVA dry weight calculation

For the calculation for the amount of polyvinyl alcohol addition for the desired solution solid content, the following equation is used.

$$Polyvinyl\ Alcohol\ Addition\ (dry\ weight) = \frac{X * Y}{100\% - \%Volatiles} \tag{C.1}$$

,where X is the desired solution solids content [%] and Y is the netto weight of the final solution.

Both Selvol PVOH 165 (Sekisui Chemical Group NJ, USA) as the PVOH 146-186 (Acros Organics, Geel, Belgium) contain 5% volatiles. Solutions are prepared with a magnetic stirrer. Dependent on mixing volume an appropriate beaker is chosen to contain the final volume size. Prior to freezing, the solution is transferred to a plastic container which is frost resistant.

Solution solids contents for all produced PVA structures are summarized in table C.1. Further, the amount and timespan of freeze-thaw cycles is reported.

Table C.1: Solution solids contents for all produced PVA structures. All samples are created with Selvol 165, unless marked with *, which is made with Acros 146-186.

Structure [(%m)]	PVA dry weight [g]	Water[g]	Freeze-thaw cycle [# (F/T hour)]
Liver model (6%m)	94.7	1405.3	2 (40/20)
Abdominal Filler (4%m)	193.7	4406.3	3 (16/8)
Abdominal Insert* (6%m)	94.7	1405.3	2 (40/20)
Intercoastal Rib Insert (6%m)	25.3	374.7	3 (16/8)
Ultrasound Patch (6%m)	13.4	199.1	2 (40/20)
Needle Force Experiments			
Selvol 165 (6%m)	26.8	398.2	2 (40/20)
Acros 146-186 (6%m)	26.8	398.2	2 (40/20)
Stress test			
Selvol 165 (4%m)	18.9	431.1	2 (16/8)
Selvol 165 (7%m)	33.2	416.8	2 (16/8)

D

Appendix D: compression test on PVA

Preliminary study into the yield strength of PVA is performed. In a compression test, the PVA samples are loaded unto a stress rate associated with respiration. The sample are loaded 2.5 times diapraghmetic pressure, which is 5.5 kg based on geometry of the samples. Three PVA sample are positioned in a triangular order to distribute loads equally and support an uniform 3 mm Plexiglas plate from which a linear stage compresses the samples in the center of the triangle. Plate bending is not accounted for in this study, since interest primarily goes out to the yield strength of the PVA.

Results In figure D.1 and D.2 the raw data of force over time for all runs are shown of 4%m and 7%m PVA, respectively. From the figures, no deviations from a linear response is observed, indicating no failure of structural integrity for the 4%w PVA sample set to a load of 0.306 kg/cm^2. Similar response is observed for the 7%w PVA sample set. Difference between the sets is seen in the stroke needed to reach a reaction force of 54N. For the 7%w PVA sample set, the stroke is 9,7 mm, whereas the 4%w PVA sample set needs a 13.4 mm stroke to show the same reaction force. The difference confirmes that, the 7%w PVA sample set has stiffer elastic properties than the 4%w PVA sample set. Furthermore, the material relaxation in the 4%w PVA sample set is larger, comparing figure D.3 and D.4. This can be observed in a force reduction after the peak load and before retraction of the load. This indicates that 4%w PVA has a higher non-linear response to force loading and more visco-elastic behaviour.

In the raw data there are peaks observable, however the origin of the peak are from interference of electrical current in the motion stage circuit and not from the samples. Therefore, the data can be filtered by a low-pass filter, correcting for influence of high frequencies and by the use of a moving average filter, limiting the maximum change per sample point.

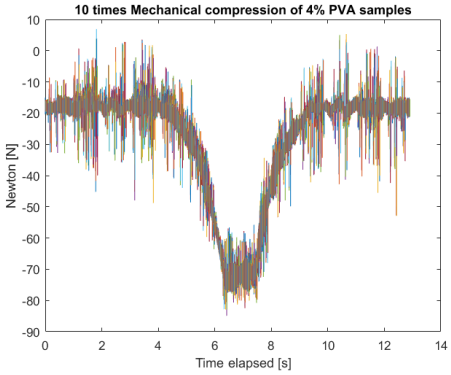

Figure D.1: Raw data of 10 runs for force over time of a minimum of 54N for 4%w PVA sample set.

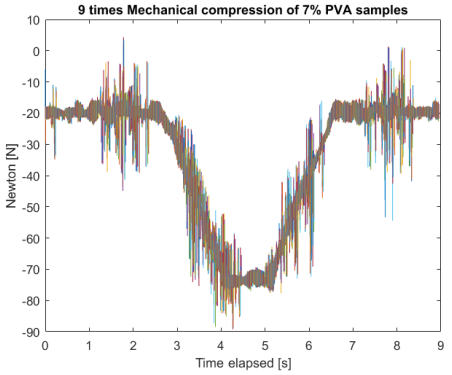

Figure D.2: Raw data of 9 runs for force over time of a minimum of 54N for 7%w PVA sample set..

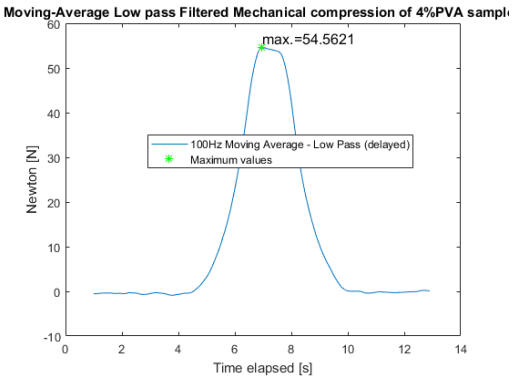

Figure D.3: Average compression response over time to indentation upto 54N for 4%w PVA sample set.

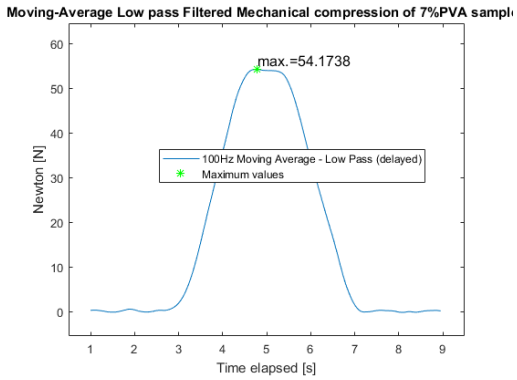

Figure D.4: Average compression response over time to indentation upto 54N for 7%w PVA sample set.

E

Appendix E: liver model characteristics

The phantom is constructed based on PVA. Interventionists response to 4%m 2ft PVA sample is too flexible if compared to a normal or diseased liver or in other words not stiff enough. In order to create a stiffer phantom the concentration PVA can be increased. Hence, a diseased liver is stiffer, an increased friction slope is expected compared to the healthy liver samples in de Jong et al. [5]. Considering that more shear stress is exerted on the needle. An increased PVA concentration, resolves in a higher friction slope. Higher peak forces are to be expected in a diseased liver since the tissue is more heterogeneous than healthy liver tissue. A higher concentration will conclude in higher peak forces. A trade-off is in place, since the number of peak forces reduces with an increased PVA concentration. Based upon the findings in de Jong et al. [5] and the feedback from interventionists. The phantom is created with a 6%m PVA and 2 FT cycles. Averaging the findings in the paper against the response of the interventionists.

Phantom preparation In the creation of the phantom the solid content solution concentration metrics as mentioned in appendix C are used. The PVA particles are submerged in water, while stirring, at room temperature. After fully submerging all particles, the solution is heated to 93 $^{\circ}C$ and maintained at this temperature for 30 minutes. Meanwhile, the mold can be prepared for pour-molding. First the inside of the two-part mold is spray-greased to make dissassembly of the model easier in a later stage. Further assembly is done by placing the rubber seal between the two parts, followed by connecting the two mold parts with nut-bolt fixation. Sequentially, the solution is pour-molded in a life-sized liver shape and left for 60 minutes to cool down, where after the mold is placed in the freezer at -30 $^{\circ}C$ for the first freeze-thaw cycle. After 16 hours freezing, the mold is still not crystallized in the center, see figure. After inspection, it is decided that the freeze period is prolonged to 40 hours. Most plausible cause of the lack of crystallization is that the mold also acts as isolator and the mold has a large volume. The heat of the poured PVA solution cannot easily disperse into the environment, thereby slowing the crystallization process. Due to the volume it contains relatively more heat energy than it's smaller scaled predecessors so it logically takes longer to freeze.

Figure E.1: Non-solid state of the liver model after a 16 hour freezing period.

After a 40 hours freezing period, the phantom is fully crystallized and can continue into a thawing phase. The phantom is placed in room temperature environment for 20 hours thawing. Where after, the FT cycle is repeated for a second time.

Figure E.2: Solid state liver model is acquired after a 40 hours freezing period.

The material properties are likely to have changed due to firstly the change in concentration and secondly, due to a different FT cycle. Due to the expected change, the properties will have to be investigated.

Notes

- Firstly, it is advised with the handling of large quantities of PVA to first cool down the mixture to room temperature after the 30-min period at 93 degrees, before pour-mold the mixture into a desired shape.

- Furthermore, the mold is prone for leakage. Preliminary use showed that solely a rubber seal is not sufficient. Additionally, for the seal, a rubber ring is placed between the two-part mold combined with Vaseline grease. The rubber with Vaseline combination was sufficient for a water tight seal.

F

Appendix F: construction drawings

In the next pages the construction drawings of manual machined parts are visible. Overview of the drawings is as follows:

- Drawing 1: 1x Mounting to linear stage
- Drawing 2: 1x Intermediate body cardan coupling
- Drawing 3: 2x Connector part cardan coupling

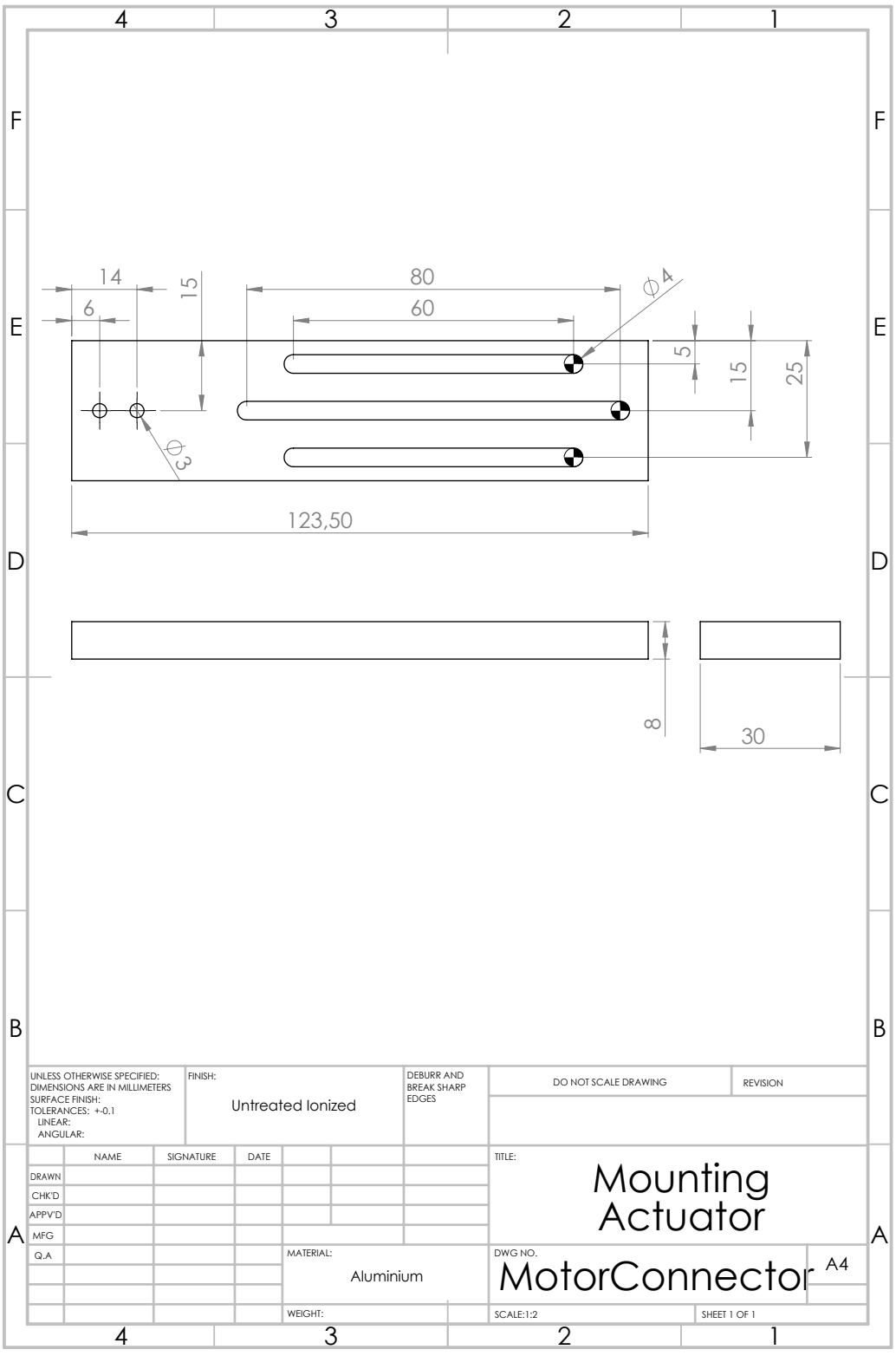
14
6
15
80
60
ϕ4
5
15
25
ϕ3
123,50
8
30
UNLESS OTHERWISE SPECIFIED:
DIMENSIONS ARE IN MILLIMETERS
SURFACE FINISH:
TOLERANCES: +-0.1
LINEAR:
ANGULAR:
FINISH:
Untreated Ionized
DEBURR AND BREAK SHARP EDGES
DO NOT SCALE DRAWING
REVISION
NAME
SIGNATURE
DATE
DRAWN
CHK'D
APPV'D
MFG
Q.A
TITLE:
Mounting Actuator
MATERIAL:
Aluminium
DWG NO.
MotorConnector
A4
WEIGHT:
SCALE:1:2
SHEET 1 OF 1

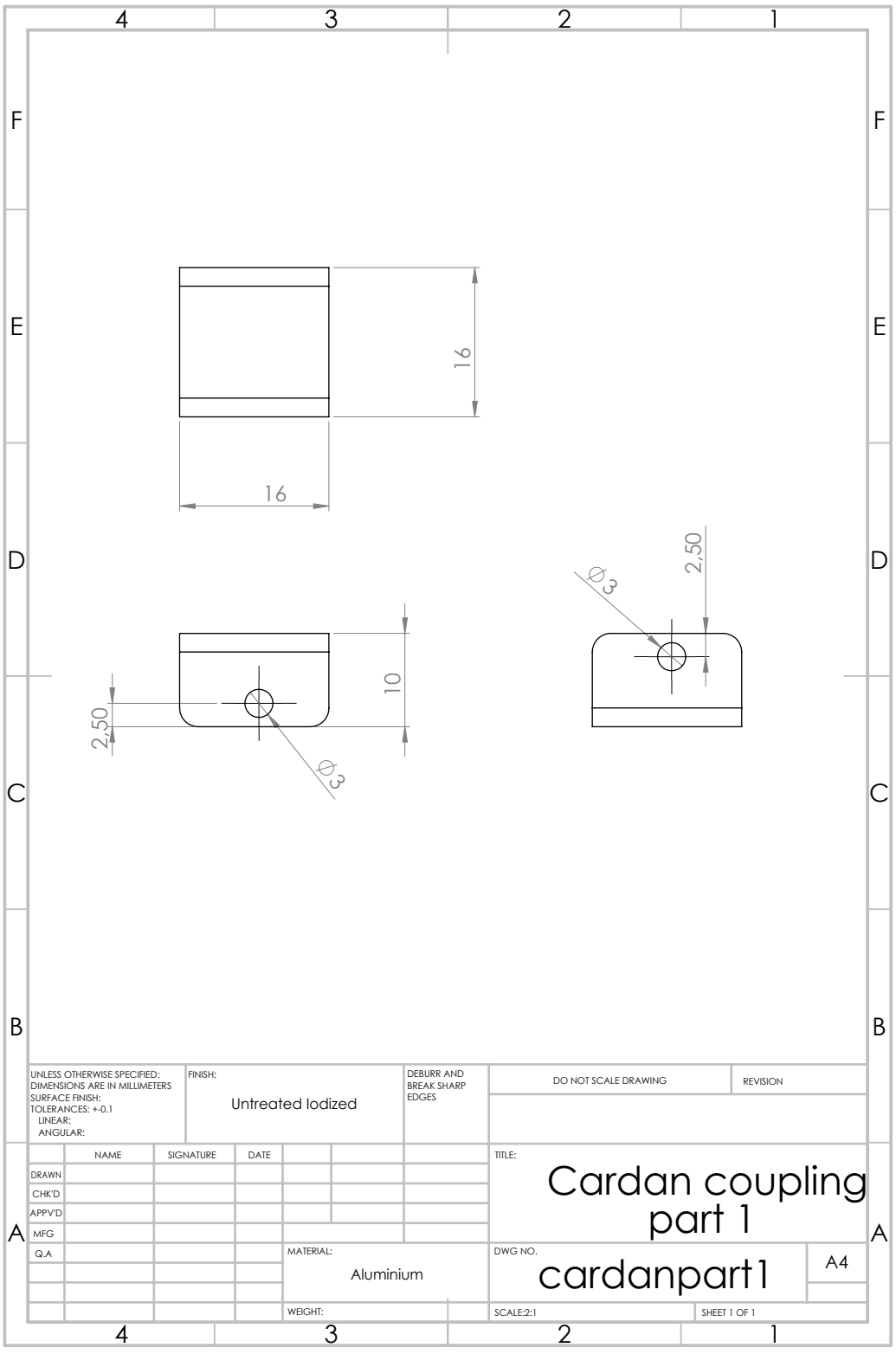
4
3
2
1
F
E
D
C
B
A
16
16
10
2,50
2,50
Ø3
Ø3
UNLESS OTHERWISE SPECIFIED:
DIMENSIONS ARE IN MILLIMETERS
SURFACE FINISH:
TOLERANCES: +-0.1
LINEAR:
ANGULAR:
FINISH:
Untreated Iodized
DEBURR AND BREAK SHARP EDGES
DO NOT SCALE DRAWING
REVISION
NAME
SIGNATURE
DATE
DRAWN
CHK'D
APPV'D
MFG
Q.A
TITLE:
Cardan coupling part 1
MATERIAL:
Aluminium
DWG NO.
cardanpart1
A4
WEIGHT:
SCALE:2:1
SHEET 1 OF 1

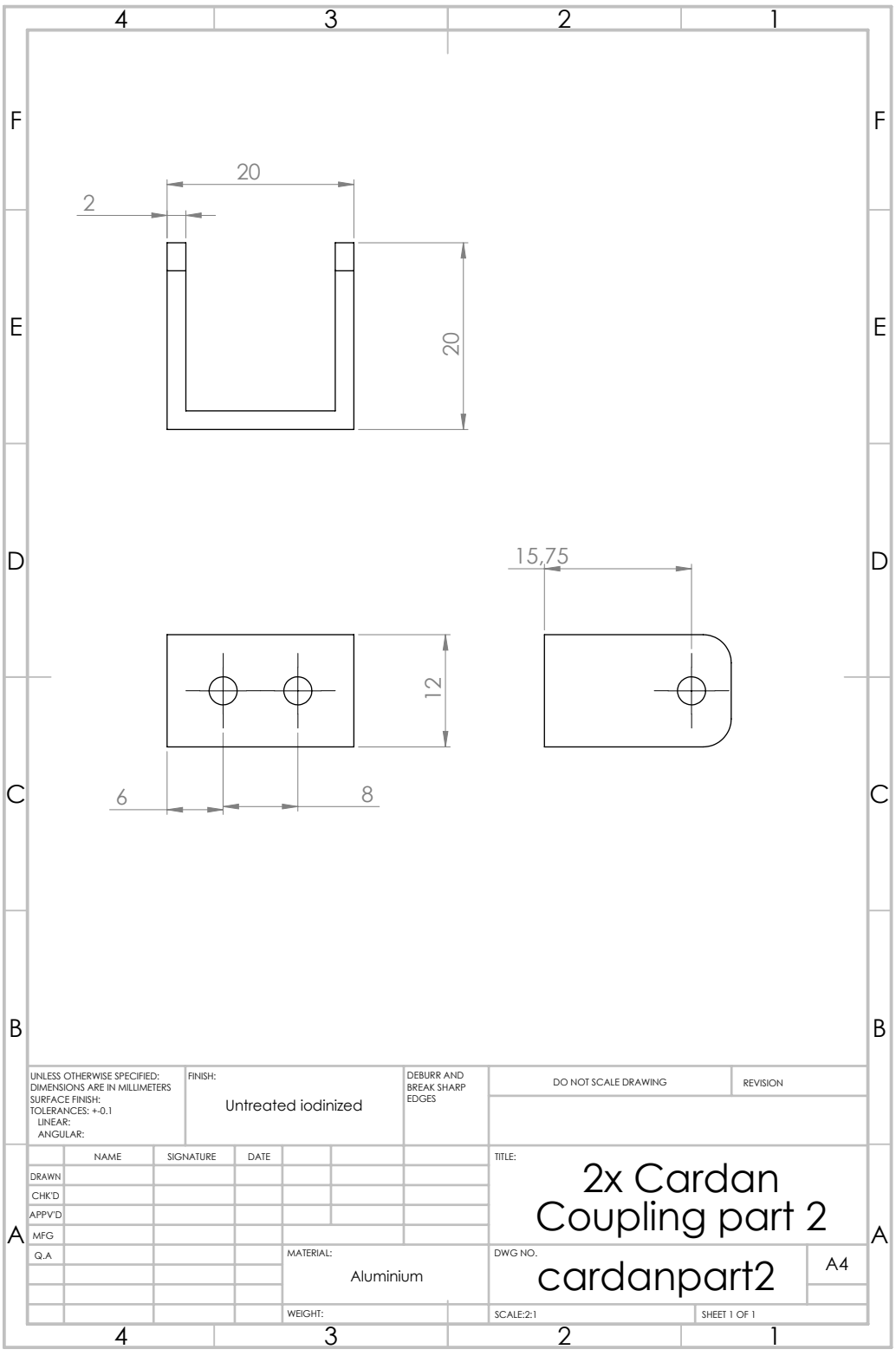
4
3
2
1
F
E
D
C
B
A
20
2
20
15,75
12
6
8
UNLESS OTHERWISE SPECIFIED:
DIMENSIONS ARE IN MILLIMETERS
SURFACE FINISH:
TOLERANCES: +-0.1
LINEAR:
ANGULAR:
FINISH:
Untreated iodinized
DEBURR AND BREAK SHARP EDGES
DO NOT SCALE DRAWING
REVISION
NAME
SIGNATURE
DATE
DRAWN
CHK'D
APPV'D
MFG
Q.A
TITLE:
2x Cardan Coupling part 2
MATERIAL:
Aluminium
DWG NO.
cardanpart2
A4
WEIGHT:
SCALE:2:1
SHEET 1 OF 1

Appendix G: liver model motion data

On the following pages the liver model motion over the 6 sensors is shown. All runs are plotted. Configurations are presented in the following order:

- Configuration Liver model: Dynamic 12 rpm
- Configuration Liver model: Dynamic 18 rpm
- Configuration Liver model: Dynamic 12 rpm with additional insert

Configuration: Dynamic 12 rpm

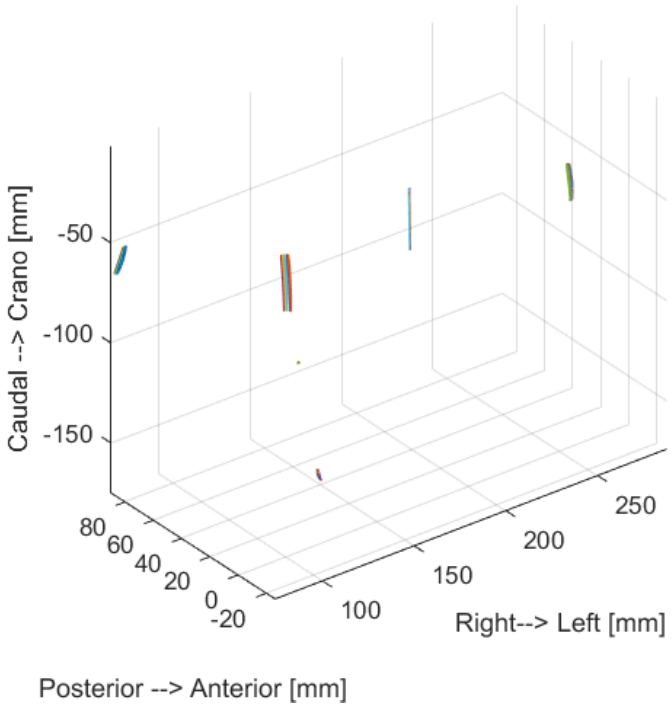

Configuration: Dynamic 12 rpm

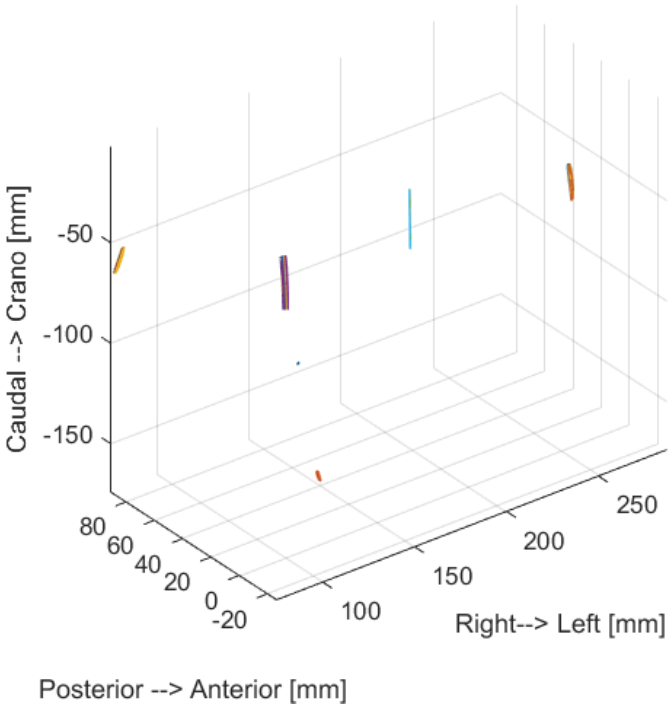

Configuration: Dynamic 12 rpm with insert

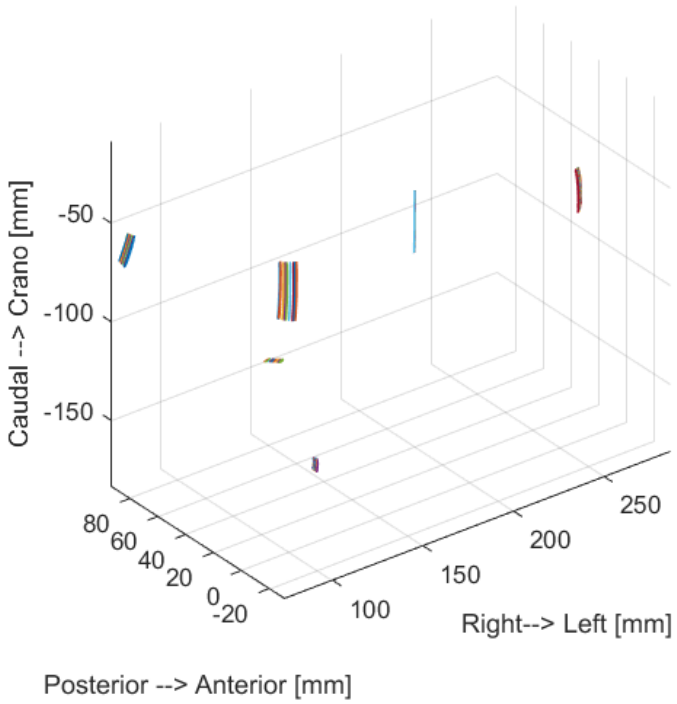

H

Appendix H: needle insertion data

On the following pages the force position diagrams for determination of the mechinical tissue properties are shown. All runs are plotted. Configurations are presented in the following order:

- Configuration Selvol 165 6%m PVA 2 FT (40/20h)
- Configuration Acros 146-186 6%m PVA 2 FT (40/20h)

Note that the y-axis are not equally scaled. The difference is chosen for, so visability of the data is increased.

Configuration: Selvol 165 6%m PVA 2 FT (40/20h)

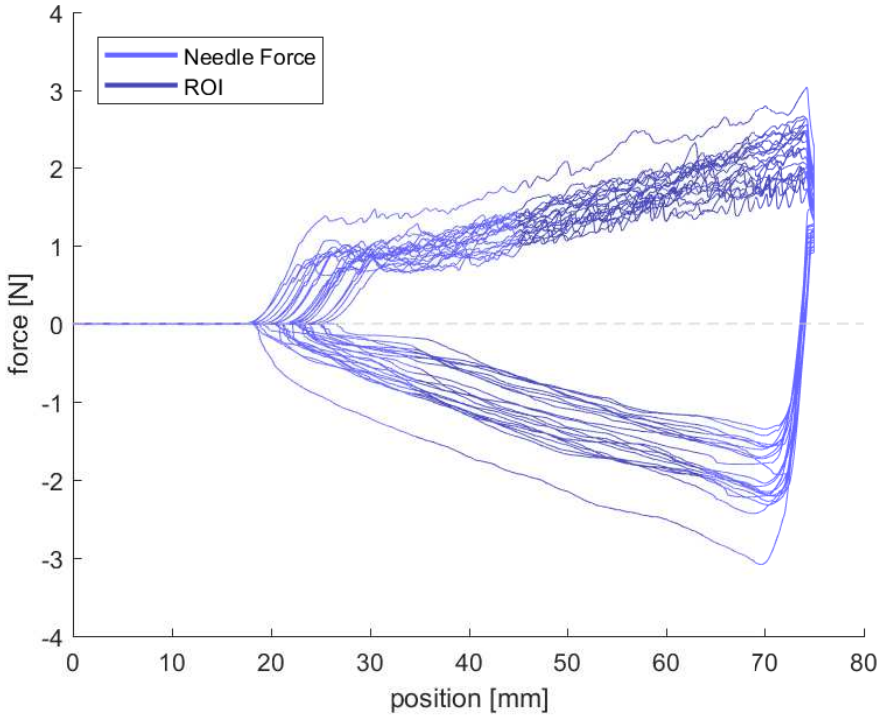

Configuration: Acros 146-186 6%m PVA 2 FT (40/20h)

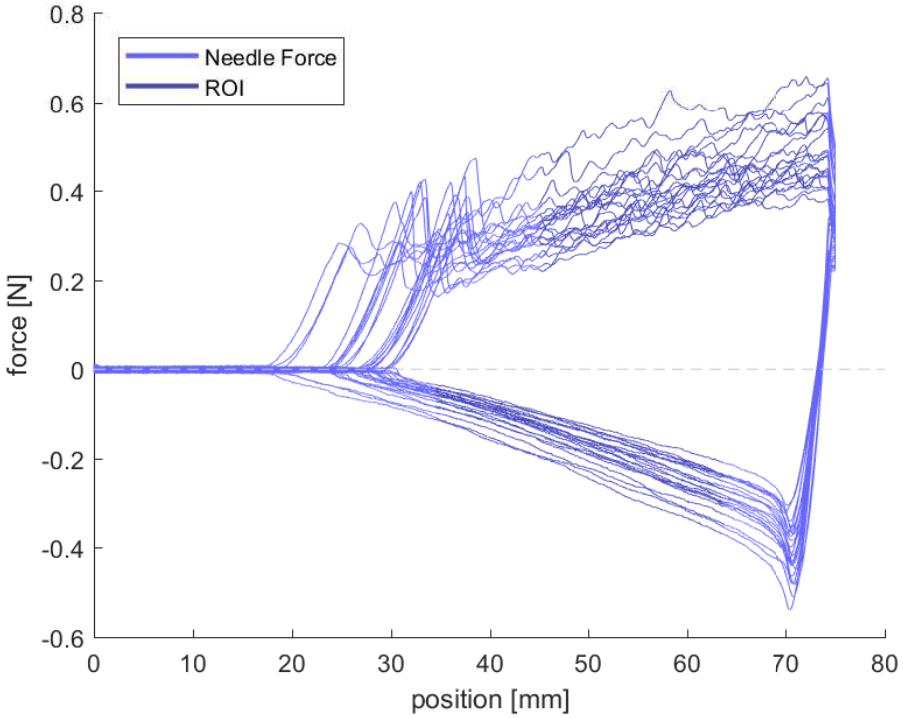

I

Appendix I: needle deflection data of all runs

On the following pages the needle deflection of all runs are shown. Configurations are presented in the following order:

- Configuration Subcostal Midplane: Static and Dynamic 12 rpm
- Configuration Intercostal Midclavicular: Static and Dynamic 12 rpm
- Configuration Subcostal Midaxillary: Static and Dynamic 12 rpm

Note that in some figures a peak appears in the first seconds, the peak appear due to errorous data points. The aurora records misfitted data with exponetial large values.

Configuration: Subcostal Midplane insertion static

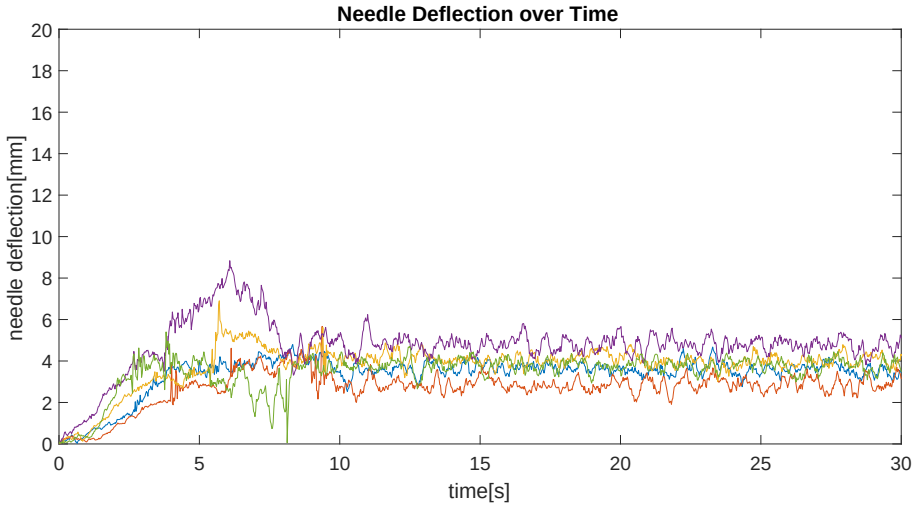

Configuration: Subcostal Midplane insertion dynamic 12 rpm

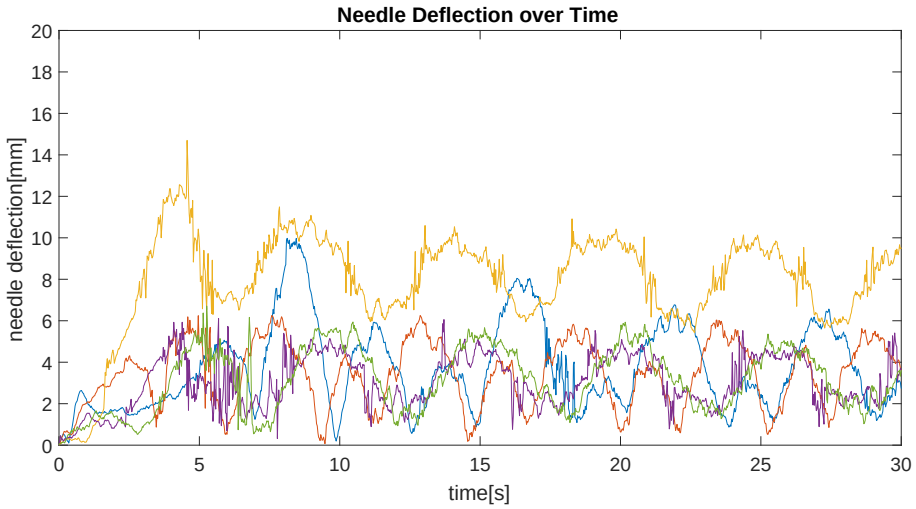

Configuration: Intercostal Midclavicular insertion static

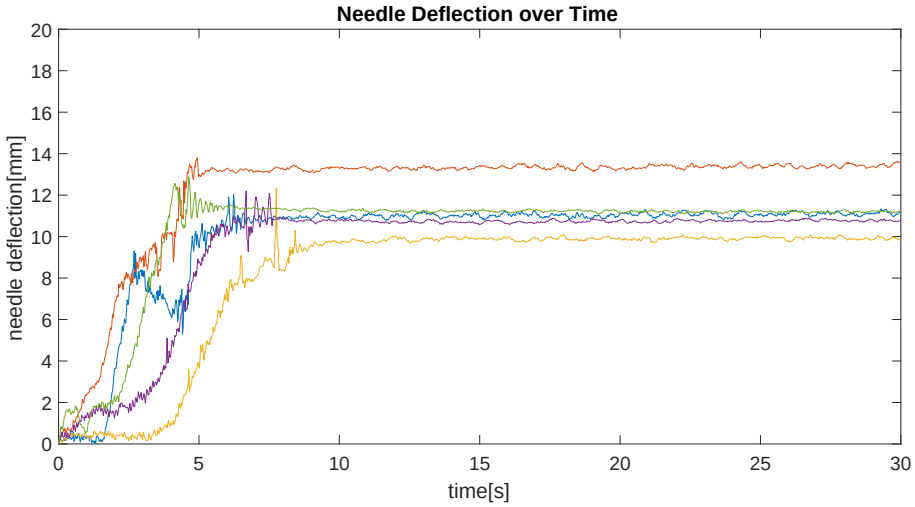

Configuration: Intercostal Midclavicular insertion dynamic 12 rpm

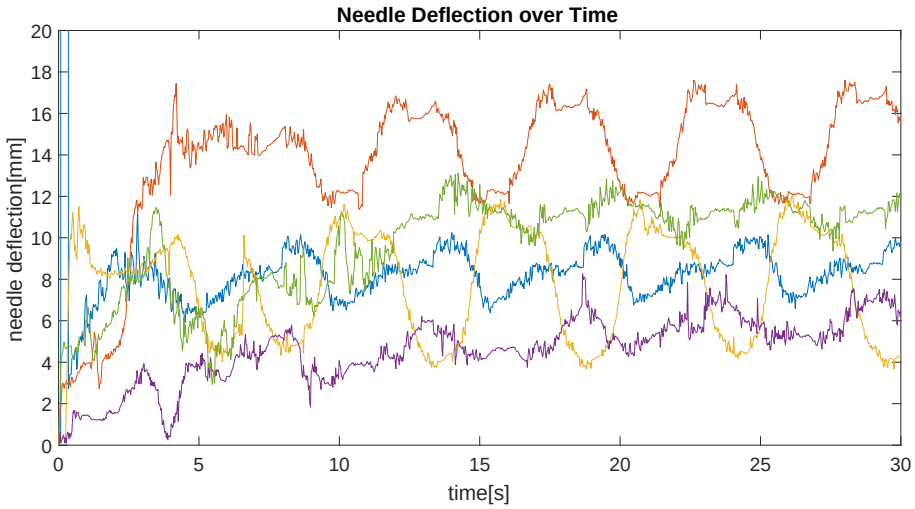

Configuration: Intercostal Mid-axial insertion static

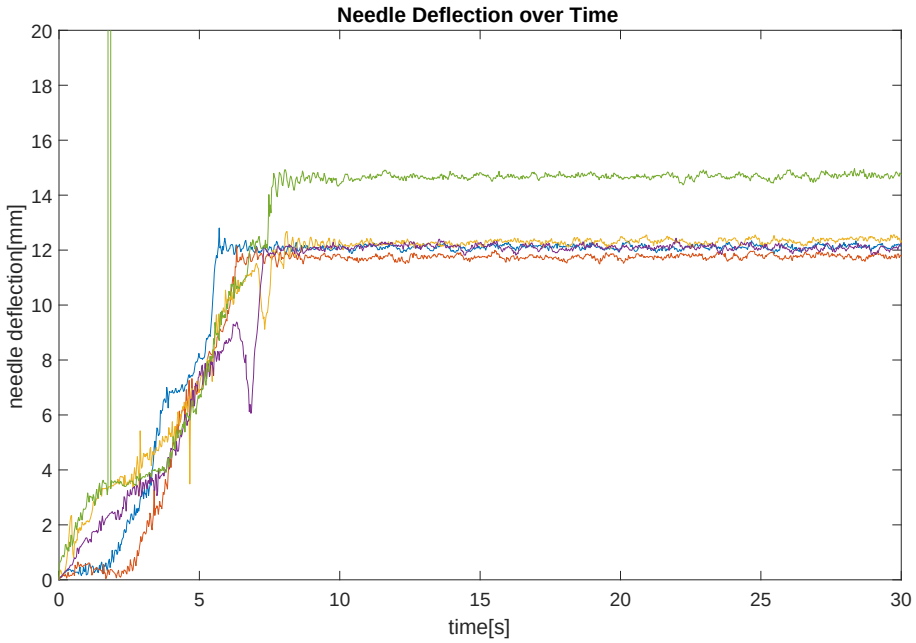

Configuration: Intercostal Mid-axial insertion dynamic 12 rpm

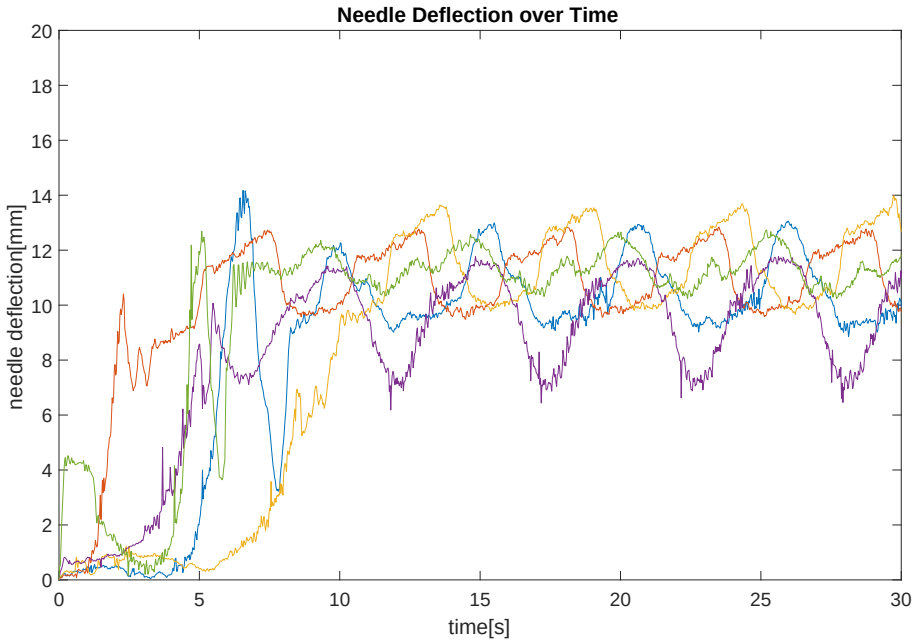

J

Appendix J: Reference signal

In the following section, the reference signal during the liver model motion experiment is presented. On both figures can be noted that the motion for 18 rpm is smaller in all directions compared to 12 rpm. This is due to the same gain is used in both feedback loops for reproduction of the sinosoid motion. The gain is too low for the shortened period in 18 rpm configuration. The feedback control should correct harder for the error, but with the same gain, the feedback loop is too slow.

Reference signal for the model motion without Insert

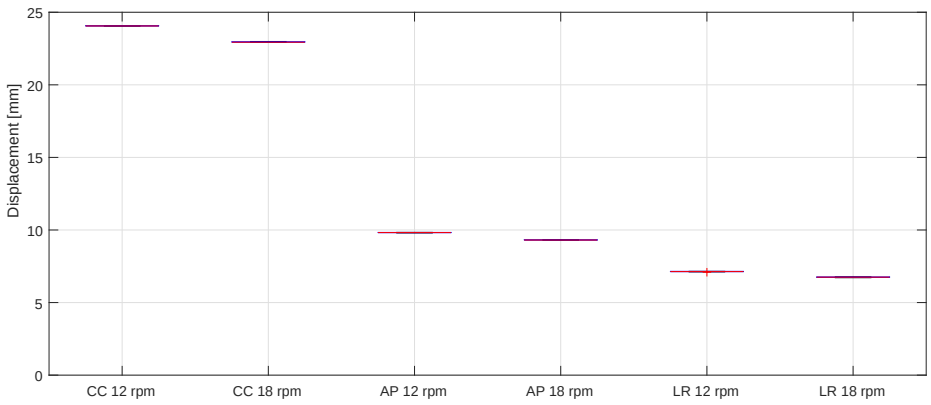

Reference signal for the model motion with Insert

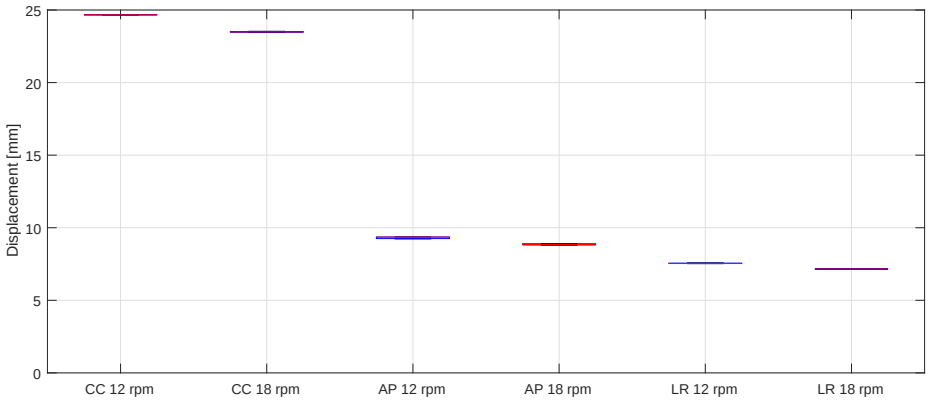

K

Appendix K: assessment form for phantom performance

The performance of the phantom prototype has been assessed on several aspects. Dr. A. Moelker filled in the assessment form. The assessment grade is made bold.

Prototype assessment:

Scale goes from 1-5, where 1 is very bad, 3 neutral and 5 very good.

How well does the prototype resemble realistic needle **motion** by respiration?

1	2	3	**4**	5
Very bad		neutral		very good

How well does the prototype resemble realistic needle **force** by respiration?

1	**2**	**3**	4	5
Very bad		neutral		very good

How well does the prototype resemble realistic **aesthetics** by respiration?

1	2	**3**	4	5
Very bad		neutral		very good

What do think about the size of the prototype?

1	2	3	**4**	5
Very bad		neutral		very good

How well does the prototype resemble realistic ultrasound imaging properties?

1	2	3	**4**	5
Very bad		neutral		very good

How well does the prototype generate ultrasound- imaging feedback during ultrasound-guided needle insertion?

1	2	3	**4**	5
Very bad		neutral		very good

How well does the liver represent sick tissue?

1	**2**	3	4	5
Very bad		neutral		very good

What is the overall performance of the prototype?

1	2	**3**	**4**	5
Very bad		neutral		very good

Bibliography

[1] Lexing Yu, Silvia Affo, and Robert F Schwabe. Fibrosis and liver cancer. *Annual Review of Pathology: Mechanisms of Disease*, 12(1), 2016.

[2] Wen-Chun Yeh, Pai-Chi Li, Yung-Ming Jeng, Hey-Chi Hsu, Po-Ling Kuo, Meng-Lin Li, Pei-Ming Yang, and Po Huang Lee. Elastic modulus measurements of human liver and correlation with pathology. *Ultrasound in medicine & biology*, 28(4):467–474, 2002.

[3] Shan Jiang, Pan Li, Yan Yu, Jun Liu, and Zhiyong Yang. Experimental study of needle–tissue interaction forces: effect of needle geometries, insertion methods and tissue characteristics. *Journal of biomechanics*, 47(13):3344–3353, 2014.

[4] Ajit H Goenka, Brian R Herts, Frank Dong, Nancy A Obuchowski, Andrew N Primak, Wadih Karim, and Mark E Baker. Image noise, cnr, and detectability of low-contrast, low-attenuation liver lesions in a phantom: Effects of radiation exposure, phantom size, integrated circuit detector, and iterative reconstruction. *Radiology*, page 151621, 2016.

[5] Tonke L de Jong, Loes H Pluymen, Dennis J van Gerwen, Gert-Jan Kleinrensink, Jenny Dankelman, and John J van den Dobbelsteen. Pva matches human liver in needle-tissue interaction. *Journal of the Mechanical Behavior of Biomedical Materials*, 2017.

[6] AJ Hindle and AC Perkins. A perfusion phantom for the evaluation of ultrasound contrast agents. *Ultrasound in medicine & biology*, 20(3):309–314, 1994.

[7] KJM Surry, HJB Austin, A Fenster, and TM Peters. Poly (vinyl alcohol) cryogel phantoms for use in ultrasound and mr imaging. *Physics in medicine and biology*, 49(24):5529, 2004.

[8] Nikolai Hungr, Jean-Alexandre Long, Vincent Beix, and Jocelyne Troccaz. A realistic deformable prostate phantom for multimodal imaging and needle-insertion procedures. *Medical Physics*, 39(4):2031–2041, 2012.

[9] L. H. Pluymen. Master thesis: Liver tissue mimicking materials for image-guided needle interventions. Tu Delft, 2016.

[10] K Zell, JI Sperl, MW Vogel, R Niessner, and C Haisch. Acoustical properties of selected tissue phantom materials for ultrasound imaging. *Physics in medicine and biology*, 52(20):N475, 2007.

[11] Y Thakur, HN Nikolov, IB Gulka, DW Holdsworth, and M Drangova. Design and construction of a multipath vessel phantom for interventional training. *The British journal of radiology*, 2014.

[12] RA Nicholson and M Crofton. Training phantom for ultrasound guided biopsy. *The British journal of radiology*, 70(830):192–194, 1997.

[13] Mohammad Ali Tavallaei, Patricia M Johnson, Junmin Liu, and Maria Drangova. Design and evaluation of an mri-compatible linear motion stage. *Medical physics*, 43(1):62–71, 2016.

[14] Dumitru Mazilu, Alexandru Patriciu, Lucian Gruionu, Marc McAllister, Albert Ong, Lars Ellison, Dominic Frimberger, Oscar Fugita, Louis Kavoussi, and Dan Stoianovici. Synthetic torso for training in and evaluation of urologic laparoscopic skills. *Journal of endourology*, 20(5):340–345, 2006.

[15] Sherif RZ Abdel-Misih and Mark Bloomston. Liver anatomy. *Surgical Clinics of North America*, 90(4): 643–653, 2010.

[16] Robert Morreale. Liver cancer, 2004. URL `https://www.cancer.net/es/nofollow/liver-cancer`.

[17] Keith L Moore, Arthur F Dalley, and Anne MR Agur. *Clinically oriented anatomy*. Lippincott Williams & Wilkins, 2013.

[18] WW Lautt. Hepatic vasculature: a conceptual review. *Gastroenterology*, 73(5):1163–1169, 1977.

[19] Matthew M Yeh and Elizabeth M Brunt. Pathology of nonalcoholic fatty liver disease. *American journal of clinical pathology*, 128(5):837–847, 2007.

[20] J. Eubanks. Fatty liver, 2013. URL `http://blog.professionalsupplementcenter.com/fatty-liver/#.WbpkccgjFPY`.

[21] ALF. American Liver Foundation alcohol-related liver disease. `http://www.liverfoundation.org/abouttheliver/info/alcohol/`, 2017. Accessed: 2017-01-20.

[22] Emanuel Rubin and Charles S Lieber. Fatty liver, alcoholic hepatitis and cirrhosis produced by alcohol in primates. *New England Journal of Medicine*, 290(3):128–135, 1974.

[23] Detlef Schuppan and Nezam H Afdhal. Liver cirrhosis. *The Lancet*, 371(9615):838–851, 2008.

[24] Toshiro Nakashima, Kunio Okuda, Masamichi Kojiro, Atsuro Jimi, Ryusuke Yamaguchi, Kazuyoshi Sakamoto, and Tamio Ikari. Pathology of hepatocellular carcinoma in japan: 232 consecutive cases autopsied in ten years. *Cancer*, 51(5):863–877, 1983.

[25] Niki Abolhassani, Rajni Patel, and Mehrdad Moallem. Needle insertion into soft tissue: A survey. *Medical engineering & physics*, 29(4):413–431, 2007.

[26] Ron Alterovitz, Ken Goldberg, Jean Pouliot, Richard Taschereau, and I-Chow Hsu. Needle insertion and radioactive seed implantation in human tissues: Simulation and sensitivity analysis. In *Robotics and Automation, 2003. Proceedings. ICRA'03. IEEE International Conference on*, volume 2, pages 1793–1799. IEEE, 2003.

[27] Allison M Okamura, Christina Simone, and Mark D O'leary. Force modeling for needle insertion into soft tissue. *IEEE transactions on biomedical engineering*, 51(10):1707–1716, 2004.

[28] Carl S McGill, Jonathon A Schwartz, Jason Z Moore, Patrick W McLaughlin, and Albert J Shih. Effects of insertion speed and trocar stiffness on the accuracy of needle position for brachytherapy. *Medical physics*, 39(4):1811–1817, 2012.

[29] Subrata Pal. Mechanical properties of biological materials. In *Design of Artificial Human Joints & Organs*, pages 23–40. Springer, 2014.

[30] Dennis J van Gerwen, Jenny Dankelman, and John J van den Dobbelsteen. Needle–tissue interaction forces–a survey of experimental data. *Medical engineering & physics*, 34(6):665–680, 2012.

[31] Simon P DiMaio and Septimiu E Salcudean. Needle insertion modeling and simulation. *IEEE Transactions on robotics and automation*, 19(5):864–875, 2003.

[32] Wenwu Ling, Qiang Lu, Changli Lu, Jierong Quan, Lin Ma, Jiawu Li, Du He, Jianping Liu, Jiaying Yang, Tianfu Wen, et al. Effects of vascularity and differentiation of hepatocellular carcinoma on tumor and liver stiffness: in vivo and in vitro studies. *Ultrasound in medicine & biology*, 40(4):739–746, 2014.

[33] Elaine Nicpon Marieb and Katja Hoehn. *Human anatomy & physiology*. Pearson Education, 2007.

[34] Larry A DeWerd and Michael Kissick. *The Phantoms of Medical and Health Physics*. Springer, 2014.

[35] Ultrasoundpaedia. Ultrasound of liver segments, 2014. URL `http://www.ultrasoundpaedia.com/segments/`.

[36] Study blue Inc. Abdomen test 3, 2017. URL `https://www.studyblue.com/notes/note/n/abdomen-test-3/deck/7857611`.

[37] NIDDK. The National Institute of Diabetes and Digestive and Kidney Diseases liver biopsy. `https://www.niddk.nih.gov/health-information/health-topics/diagnostic-tests/liver-biopsy/Pages/diagnostic-test.aspx`, 2014. Accessed: 2017-01-09.

[38] John H McAfee, Emmet B Keeffe, Randall G Lee, and Josef Rösch. Transjugular liver biopsy. *Hepatology*, 15(4):726–732, 1992.

[39] Mark W Mewissen. Transvenous liver biopsy. *Journal of Vascular and Interventional Radiology*, 7(1): 278–282, 1996.

[40] Timothy WI Clark. Chemical ablation of liver cancer. *Techniques in vascular and interventional radiology*, 10(1):58–63, 2007.

[41] Yue-Yong Xiao, Jin-Lin Tian, Jia-Kai Li, Li Yang, and Jin-Shan Zhang. Ct-guided percutaneous chemical ablation of adrenal neoplasms. *American Journal of Roentgenology*, 190(1):105–110, 2008.

[42] S Nahum Goldberg, G Scott Gazelle, and Peter R Mueller. Thermal ablation therapy for focal malignancy: a unified approach to underlying principles, techniques, and diagnostic imaging guidance. *American journal of roentgenology*, 174(2):323–331, 2000.

[43] Xin-Da Zhou and Zhao-You Tang. Cryotherapy for primary liver cancer. In *Seminars in surgical oncology*, volume 14, pages 171–174. Wiley Online Library, 1998.

[44] Erica M Knavel and Christopher L Brace. Tumor ablation: common modalities and general practices. *Techniques in vascular and interventional radiology*, 16(4):192–200, 2013.

[45] The Johns Hopkins University. Radiofrequency ablation (rfa), 2017. URL `https://www.hopkinsmedicine.org/liver_tumor_center/treatments/ablative_techniques/radio_frequency_ablation.html`.

[46] Byung Ihn Choi, Ho Chul Kim, Joon Koo Han, Jae Hyung Park, Yong Ii Kim, Soo Tae Kim, Hyo Suk Lee, Chung Yong Kim, and Man Chung Han. Therapeutic effect of transcatheter oily chemoembolization therapy for encapsulated nodular hepatocellular carcinoma: Ct and pathologic findings. *Radiology*, 182 (3):709–713, 1992.

[47] Laura Marelli, Rosa Stigliano, Christos Triantos, Marco Senzolo, Evangelos Cholongitas, Neil Davies, Jonathan Tibballs, Tim Meyer, David W Patch, and Andrew K Burroughs. Transarterial therapy for hepatocellular carcinoma: which technique is more effective? a systematic review of cohort and randomized studies. *Cardiovascular and interventional radiology*, 30(1):6–25, 2007.

[48] Bruno Sangro, Mercedes Iñarrairaegui, and Jose I Bilbao. Radioembolization for hepatocellular carcinoma. *Journal of hepatology*, 56(2):464–473, 2012.

[49] Filip Banovac, Neil Glossop, David Lindisch, Daigo Tanaka, Elliot Levy, and Kevin Cleary. Liver tumor biopsy in a respiring phantom with the assistance of a novel electromagnetic navigation device. In *International Conference on Medical Image Computing and Computer-Assisted Intervention*, pages 200–207. Springer, 2002.

[50] I Suramo, M Päivänsalo, and V Myllylä. Cranio-caudal movements of the liver, pancreas and kidneys in respiration. *Acta radiologica. Diagnosis*, 25(2):129–131, 1984.

[51] Torsten Rohlfing, Calvin R Maurer, Walter G O'dell, and Jianhui Zhong. Modeling liver motion and deformation during the respiratory cycle using intensity-based nonrigid registration of gated mr images. *Medical physics*, 31(3):427–432, 2004.

[52] Jane M Blackall, Andrew P King, Graeme P Penney, A Adam, and David J Hawkes. A statistical model of respiratory motion and deformation of the liver. In *International Conference on Medical Image Computing and Computer-Assisted Intervention*, pages 1338–1340. Springer, 2001.

[53] Torsten Rohlfing, Calvin R Maurer Jr, Walter G O'Dell, and Jianhui Zhong. Modeling liver motion and deformation during the respiratory cycle using intensity-based free-form registration of gated mr images. *Medical Imaging: Visualization, Display, and Image-Guided Procedures*, 4319:337–348, 2001.

[54] Kate McLeish, Derek LG Hill, David Atkinson, Jane M Blackall, and Reza Razavi. A study of the motion and deformation of the heart due to respiration. *IEEE transactions on medical imaging*, 21(9):1142–1150, 2002.

[55] Kent R Barker. Method of monitoring patient respiration and predicting apnea therefrom, December 28 1982. US Patent 4,365,636.

[56] Ralph Lin, Emmanuel Wilson, Jonathan Tang, Dan Stoianovici, and Kevin Cleary. A computer-controlled pump and realistic anthropomorphic respiratory phantom for validating image-guided systems. In *Medical Imaging*, pages 65090E–65090E. International Society for Optics and Photonics, 2007.

[57] Elena Nioutsikou, J Richard N Symonds-Tayler, James L Bedford, and Steve Webb. Quantifying the effect of respiratory motion on lung tumour dosimetry with the aid of a breathing phantom with deforming lungs. *Physics in medicine and biology*, 51(14):3359, 2006.

[58] Rolf B Saager, Clement Kondru, Kendrew Au, Kelly Sry, Frederick Ayers, and Anthony J Durkin. Multilayer silicone phantoms for the evaluation of quantitative optical techniques in skin imaging. In *Design and Performance Validation of Phantoms Used in Conjunction with Optical Measurement of Tissue II*, volume 7567, page 756706. International Society for Optics and Photonics, 2010.

[59] Ernest L Madsen and Gary R Frank. Ultrasound phantoms, February 20 2001. US Patent 6,190,915.

[60] Mohsen Mahvash and Pierre E Dupont. Mechanics of dynamic needle insertion into a biological material. *IEEE Transactions on Biomedical Engineering*, 57(4):934–943, 2010.

[61] Shinichi Minohara, Masahiro Endo, Tatsuaki Kanai, Hirotoshi Kato, and Hirohiko Tsujii. Estimating uncertainties of the geometrical range of particle radiotherapy during respiration. *International Journal of Radiation Oncology* Biology* Physics*, 56(1):121–125, 2003.

[62] Raymond A. Long. Diaphragmatic (belly) breathing, 2015. URL `http://www.dailybandha.com/2015/08/diaphragmatic-belly-breathing.html`.

[63] S C Davies, A L Hill, R B Holmes, M Halliwell, and P C Jackson. Ultrasound quantitation of respiratory organ motion in the upper abdomen. *The British Journal of Radiology*, 67(803):1096–1102, 1994. doi: 10.1259/0007-1285-67-803-1096. URL `https://doi.org/10.1259/0007-1285-67-803-1096`. PMID: 7820402.

[64] Yvette Seppenwoolde, Hiroki Shirato, Kei Kitamura, Shinichi Shimizu, Marcel Van Herk, Joos V Lebesque, and Kazuo Miyasaka. Precise and real-time measurement of 3d tumor motion in lung due to breathing and heartbeat, measured during radiotherapy. *International Journal of Radiation Oncology* Biology* Physics*, 53(4):822–834, 2002.

[65] Hieu Trung Huynh, Ibrahim Karademir, Aytekin Oto, and Kenji Suzuki. Computerized liver volumetry on mri by using 3d geodesic active contour segmentation. *American Journal of Roentgenology*, 202(1): 152–159, 2014.

[66] Arne Militzer, Tobias Hager, Florian Jager, Christian Tietjen, and Joachim Hornegger. Automatic detection and segmentation of focal liver lesions in contrast enhanced ct images. In *Pattern Recognition (ICPR), 2010 20th International Conference on*, pages 2524–2527. IEEE, 2010.

[67] Lau Brix, Steffen Ringgaard, Thomas Sangild Sørensen, and Per Rugaard Poulsen. Three-dimensional liver motion tracking using real-time two-dimensional mri. *Medical physics*, 41(4), 2014.

[68] John S Harris. *The Product Profile Chart: A Graphical Means of Appraising and Selecting New Products*. 1961.

[69] J Michael Henderson, Steven B Heymsfield, Jed Horowitz, and Michael H Kutner. Measurement of liver and spleen volume by computed tomography. assessment of reproducibility and changes found following a selective distal splenorenal shunt. *Radiology*, 141(2):525–527, 1981.

[70] Kathryn K Hodge, John E McNeal, Martha K Terris, and Thomas A Stamey. Random systematic versus directed ultrasound guided transrectal core biopsies of the prostate. *The Journal of urology*, 142(1):71–74, 1989.

[71] DUDLEY F Rochester, NARINDER S Arora, and NM Braun. Maximum contractile force of human diaphragm muscle, determined in vivo. *Transactions of the American Clinical and Climatological Association*, 93:200, 1982.

[72] Nigel Mills. *Polymer foams handbook: engineering and biomechanics applications and design guide*. Butterworth-Heinemann, 2007.

[73] AK Maji, HL Schreyer, S Donald, Q Zuo, and D Satpathi. Mechanical properties of polyurethane-foam impact limiters. *Journal of engineering mechanics*, 121(4):528–540, 1995.

[74] H Tobushi, D Shimada, S Hayashi, and M Endo. Shape fixity and shape recovery of polyurethane shape-memory polymer foams. *Proceedings of the Institution of Mechanical Engineers, Part L: Journal of Materials: Design and Applications*, 217(2):135–143, 2003.

[75] Marie Muller, Jean-Luc Gennisson, Thomas Deffieux, Mickaël Tanter, and Mathias Fink. Quantitative viscoelasticity mapping of human liver using supersonic shear imaging: preliminary in vivo feasability study. *Ultrasound in medicine & biology*, 35(2):219–229, 2009.

[76] Tonke L de Jong, Jenny Dankelman, and John J van den Dobbelsteen. Dataset on force measurements of needle insertions into two ex-vivo human livers. *Data in brief*, 11:308, 2017.

[77] Roy J Roesthuis, Youri RJ Van Veen, Alex Jahya, and Sarthak Misra. Mechanics of needle-tissue interaction. In *Intelligent Robots and Systems (IROS), 2011 IEEE/RSJ International Conference on*, pages 2557–2563. IEEE, 2011.

[78] V De Ledinghen and J Vergniol. Transient elastography (fibroscan). *Gastroenterologie clinique et biologique*, 32(6):58–67, 2008.

[79] Vincent Wai-Sun Wong, Julien Vergniol, Grace Lai-Hung Wong, Juliette Foucher, Henry Lik-Yuen Chan, Brigitte Le Bail, Paul Cheung-Lung Choi, Mathurin Kowo, Anthony Wing-Hung Chan, Wassil Merrouche, et al. Diagnosis of fibrosis and cirrhosis using liver stiffness measurement in nonalcoholic fatty liver disease. *Hepatology*, 51(2):454–462, 2010.

[80] Yi-Je Lim, Dhanannjay Deo, Tejinder P Singh, Daniel B Jones, and Suvranu De. In situ measurement and modeling of biomechanical response of human cadaveric soft tissues for physics-based surgical simulation. *Surgical endoscopy*, 23(6):1298, 2009.

[81] Shan Jiang, Sha Liu, and Wenhao Feng. Pva hydrogel properties for biomedical application. *Journal of the mechanical behavior of biomedical materials*, 4(7):1228–1233, 2011.

[82] S Cournane, L Cannon, JE Browne, and AJ Fagan. Assessment of the accuracy of an ultrasound elastography liver scanning system using a pva-cryogel phantom with optimal acoustic and mechanical properties. *Physics in medicine and biology*, 55(19):5965, 2010.

[83] Jérémie Fromageau, Elisabeth Brusseau, Didier Vray, Gérard Gimenez, and Philippe Delachartre. Characterization of pva cryogel for intravascular ultrasound elasticity imaging. *IEEE transactions on ultrasonics, ferroelectrics, and frequency control*, 50(10):1318–1324, 2003.